Title

Probing Interfacial Chemistry with Kinetic Models and Molecular Dynamics Simulations

ISBN

9798288865398

Author

Cohen, Liron

Publication Date

2025-08-15

Peer reviewed|Thesis/dissertation

Probing Interfacial Chemistry with Kinetic Models and Molecular Dynamics Simulations

by

Liron Cohen

A dissertation submitted in partial satisfaction of the
requirements for the degree of
Doctor of Philosophy
in
Chemistry
in the
Graduate Division
of the
University of California, Berkeley

Committee in charge:
Dr. Kevin R. Wilson, co-chair
Professor Richard J. Saykally, co-chair
Professor David T. Limmer
Professor Allen H. Goldstein

Summer 2025

Probing Interfacial Chemistry with Kinetic Models and Molecular Dynamics Simulations

Abstract

Probing Interfacial Chemistry with Kinetic Models and Molecular Dynamics Simulations

by

Liron Cohen

Doctor of Philosophy in Chemistry

University of California, Berkeley

Dr. Kevin R. Wilson, Co-Chair
Professor Richard J. Saykally, Co-Chair

At the interface, molecules experience local environments defined by anisotropic forces, disrupted solvation structures, and steep spatial gradients. These conditions can influence reaction pathways in ways that are not captured by bulk-phase experiments or models. Interfaces are ubiquitous across natural and engineered systems, including atmospheric aerosols and biological membranes. Thus, gaining a mechanistic understanding of how interfacial properties influence reaction rates is a critical step toward predicting and controlling chemical reactivity, with far-reaching implications for catalysis, atmospheric modeling, biological function, and materials design.

In this work, molecular-scale simulations are integrated with coarse-grained kinetic models to quantitatively assess the role of interfacial reactivity in multiphase reaction kinetics. This combined approach reveals how localized surface processes - such as molecular orientation, interfacial thickness, and diffusion - shape the macroscopic observed kinetics. Most studies of interfacial reactivity have focused on aqueous systems, where accelerated reaction rates are typically attributed to dielectric discontinuities or the surface enrichment of reactive solutes. In contrast, organic interfaces have received comparatively less attention. This dissertation focuses on squalene chlorination as a model system for probing chemical reactivity at a non-polar liquid-vapor interface, offering new insight into interfacial mechanisms that emerge independently of electrostatic gradients. Chapter 2 examines squalene chlorination at the air–squalene interface. We find that chlorine reacts at the surface two orders of magnitude faster than in the bulk. This acceleration is driven by a newly identified mechanism, *tail spearfishing*, in which squalene tails that extend into the gas phase, encounter chlorine with higher probability. Combined with faster interfacial diffusion, these two mechanisms quantitatively explain previously anomalous experimental results in aerosols. Chapter 3 builds on the pure squalene analysis and probes how interfacial reactivity is altered when a long chain alcohol is mixed within the aerosol liquid. Chapter 4 shifts the focus away from direct interfacial reactivity but was motivated by interest in Fenton chemistry at the air–water interface. In an effort to constrain bulk-phase kinetics before introducing interfacial complexity, a unified kinetic model was developed that describes the reaction mechanism across acidic to neutral pH conditions. Taken together, these chapters highlight how detailed molecular and kinetic analysis can reveal the underlying principles governing reactivity across diverse interfacial and bulk-phase environments.

Acknowledgments

This dissertation is dedicated to my children: to Googy, the most amazing daughter, who came with me to Berkeley with only a few suitcases, and to Boomba, the most amazing son, who was born in Berkeley and attended quantum lectures in utero. I love you both beyond words or actions, thank you for coming with me on this journey.

I would like to thank my parents. You both supported me, each in your own way. I could never be thankful enough and without your support, I would have not be able to pursue this degree. To my siblings, I love you both dearly.

A special thank you to Prof. Jamie Donaldson, who was the first to call me a scientist when I didn't think I was, and for continuing to support me throughout the years, both as a person and as a scientist.

At Berkeley, I would first like to thank Dr. Kevin Wilson for taking me as a PhD student and sticking with me until the end. I have learned a lot from you. To Prof. Phill Geissler (1974-2022), who helped get me out of the PhD slump by knowing who I was as soon as I stepped into his office and for making me feel smart again. To incoming assistant Prof. Amro Dodin, your mentorship and encouragement have been invaluable to me. To Prof. David Limmer, for providing continued support in MD simulation and theory to a non-traditional student transitioning from experimental research. Finally, I am deeply grateful to all the students and postdocs in the Wilson, Saykally, Geissler, and Limmer groups. I've learned so much through our interactions, and the collaborative scientific environment at Berkeley has made a lasting impact on me.

Table of Contents

Section Title — Page Number

Chapter 1. Introduction

1.1. Introduction - Chemical Reactions at Air/Organic Interfaces

Air/Liquid interfaces are distinct chemical environments where reactivity often proceeds differently than in the bulk. At this heterogeneous boundary between two phases, molecules experience unique physicochemical conditions such as preferential orientation, partial solvation effects, confinement of reagents, and interfacial electric fields. These conditions can give rise to markedly different mechanisms from those known to occur at either the gas or liquid phase,[1–4] with numerous studies providing evidence that interfacial environments catalyze or otherwise alter chemical transformations.[5–12] Reaction acceleration is particularly relevant in systems where interfacial area dominates chemical behavior: in atmospheric chemistry,[10,11,13–17] where aerosol and cloud droplets exhibit high surface-to-volume ratios and host heterogeneous oxidation and halogenation reactions; in biology,[18] where lipid bilayers and protein interfaces facilitate catalysis, signaling, and transport; and in industrial and engineered systems, where reactivity at catalytic surfaces or within emulsions[19,20] can determine efficiency, selectivity, and product distribution.

Accurately describing interfacial chemical processes requires a detailed understanding of the elementary transport and kinetic steps that occur as a gas-phase species transitions into the bulk liquid phase. A key parameter used to describe this behavior is the reactive uptake coefficient (γ), which represents the overall probability that a gas-surface collision results in reaction.[21–23] Experimentally, γ is often determined by monitoring the loss rate of a reactive gas as it interacts with a known surface area under controlled flow or static conditions. The rate of loss, normalized by the molecular flux of gas molecules to the surface, yields a dimensionless value between 0 and 1. Despite its apparent simplicity, γ is not a direct measure of any single reaction step. Instead, it represents the net result of multiple coupled steps: gas-phase transport, surface accommodation, solvation, and reaction in either phase. This layered complexity makes it challenging to assign γ to a single kinetic pathway or rate constant. As a result, interpreting measured values of γ requires mechanistic models that explicitly account for the contributions and coupling of physical transport and chemical transformation.

To interpret γ in terms of underlying physical or chemical processes, several kinetic modeling frameworks have been developed. Among the most widely used is the resistor model, which conceptualizes uptake as a sequence of physical and chemical steps, each of which imposes a kinetic resistance that limits the total rate of uptake. Gas molecules diffuse through the surrounding gas phase and collide with the surface, where they may adsorb, solvate into the bulk, and ultimately react. The uptake coefficient is given by

$$\frac{1}{\gamma} = \frac{1}{\Gamma_g} + \frac{1}{\alpha} + \frac{1}{\Gamma_{sol}+\Gamma_{rxn}}, \tag{1.1}$$

where Γ_g represents the resistance of gas phase diffusion to the surface of a particle, α is the mass accommodation coefficient, Γ_{sol} represents solubility from surface to bulk and liquid diffusion, and Γ_{rxn} is the bulk liquid reaction. Figure 1.1 shows a visual representation of the resistor model

framework. This approach offers a simple yet flexible framework for linking measurable quantities like γ to molecular-level processes and is particularly useful for estimating limiting behavior, such as whether a system is transport- or reaction-limited.

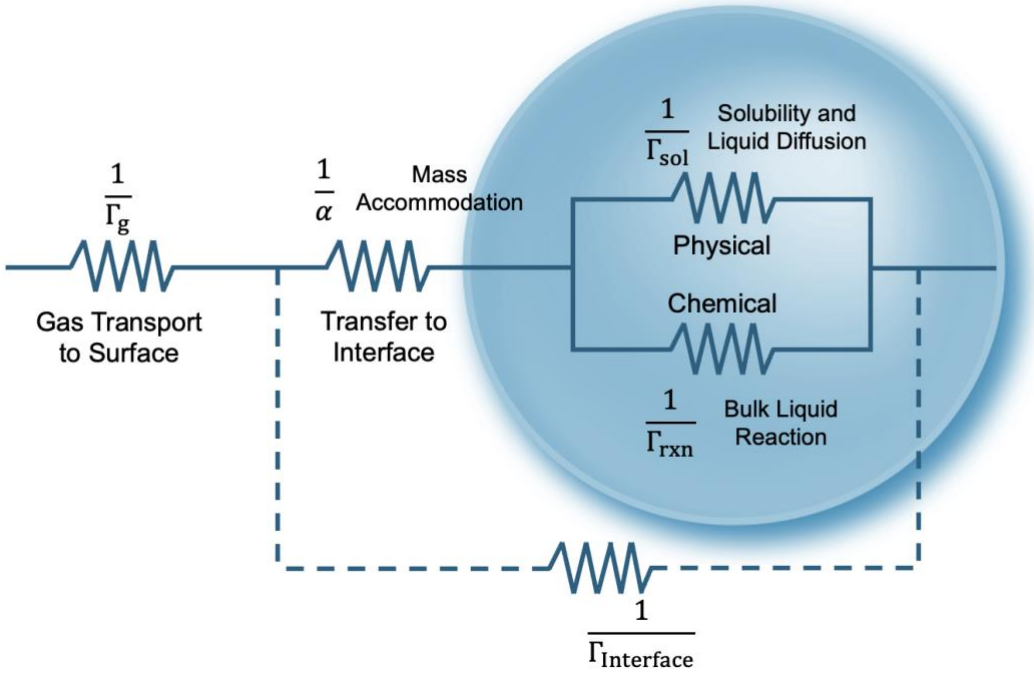

Figure 1.1 – Schematic representation of the resistor model. Gas-phase molecules diffuse and collide with the surface (Γ_g), where they may accommodate into the interface (α), solvate and diffuse through the liquid bulk (Γ_{sol}), Each of these steps introduces a kinetic resistance that collectively determines the overall reactive uptake coefficient, analogous to resistors arranged in series in an electrical circuit. Adapted from Ref [23].

While the resistor model offers a practical and intuitive framework for interpreting gas uptake, its simplicity can obscure important complexities of real multiphase systems. By treating each step as independent, the model assumes steady-state conditions, and its limiting cases require a priori assumptions about where the reaction occurs (surface or bulk). To address these issues, more detailed models have been developed. Kinetic multilayer models resolve concentration gradients across interfaces and within the bulk by numerically solving coupled diffusion-reaction equations.[24–27] Despite offering a more thorough physical description, kinetic multilayer models present additional challenges. These models typically require a large number of input parameters, including interfacial properties, diffusion coefficients specific to each phase, and reaction rates that vary with depth. Many of these parameters are difficult to measure directly. In the absence of well-constrained experimental data, model outputs can become highly sensitive to assumptions, making them difficult to validate and limiting their reliability.

To capture the essential features of multiphase reactivity while avoiding the high complexity of full molecular models, this dissertation adopts a coarse-grained kinetic framework originally developed by Willis and Wilson.[28] This approach offers a physically grounded midpoint between resistor-type formalisms and fully resolved multilayer or particle-based simulations. In

this scheme, a particle is treated as comprising two well-mixed reaction compartments: surface and bulk. Scaling of the compartments is such that the height of the bulk compartment is a/3 (where a is the particle radius) to preserve the correct surface to volume scaling in a sphere. The surface compartment thickness in previous implementations of this framework was assumed to be $\delta \approx 1$ nm, which is consistent with the dimensions of the solvation free energy profiles for aqueous interfaces obtained in previous simulations. [29] Molecules move between compartments by Fickian diffusion, and reactions can occur in either region (Figure 1.2).

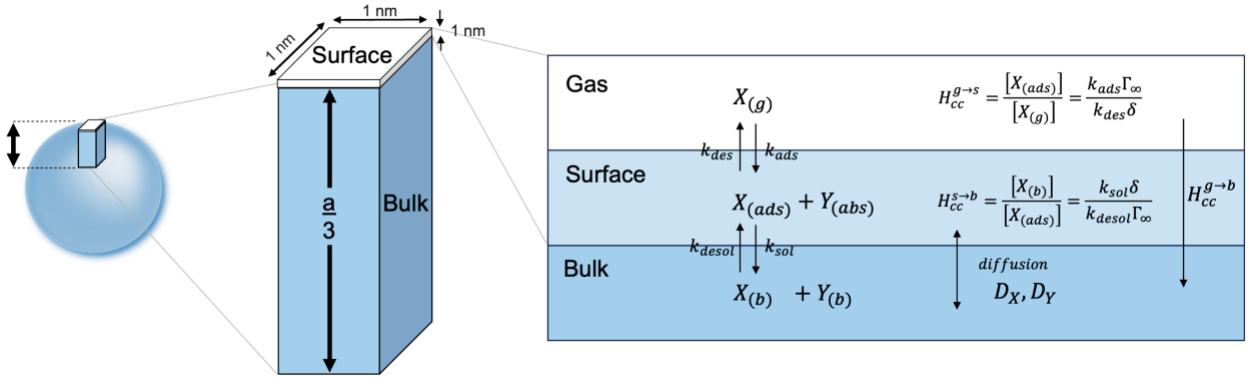

Figure 1.2 – Framework for kinetic modeling. Simulation preserves surface area to volume ratio of a sphere with surface compartment that is 1nm thick and bulk compartment with height of a/3. Three kinetic regions: gas, surface ,and bulk, maintain concentrations through coupled equilibrium determined by Henry's law coefficients. The gas-phase species X represents a reactive trace gas, while species Y denotes a liquid-phase reactant. Adsorption, solvation, and diffusion govern the movement of X into the particle, where it can react with Y at the surface or in the bulk. Kinetic rate constants and diffusion coefficients determine the rates of these processes. Surface and bulk species can react or diffuse between compartments. Maximum surface concentration Γ_∞ and interfacial thickness δ determine the concentration of surface sites.

The scheme features three kinetic regions: gas, surface, and bulk. Concentrations of species X in each region are governed by a dimensionless Henry's law constant (H_{cc}). The gas to surface Henry's law constant is,

$$H_{cc}^{g\to s} = \frac{[X_{(ads)}]}{[X_{(g)}]} = \frac{k_{ads}\Gamma_\infty}{k_{des}\delta}, \tag{1.2}$$

where k_{ads} and k_{des} are rate coefficients that describe the adsorption and desorption of X to the interface. Γ_∞ is the maximum surface concentration, and δ is the interfacial thickness. Surface sites are represented as volumetric concentrations ($\frac{\Gamma_\infty}{\delta}$). k_{ads} is set to the collision frequency of X gas, which assumes a sticking probability of 1,

$$k_{ads} = \frac{\bar{c}A}{4}, \tag{1.3}$$

where $\bar{c}$ is the mean speed of species X in the gas phase, and A is the area of the surface compartment. k_{des} is computed from Eq. (1.2) using k_{ads} and $H_{cc}^{g\to s}$. Once X is adsorbed at the surface, it can react with a Y molecule, desorb back into the gas phase, or become solvated into the bulk liquid. Surface to bulk partitioning is described by a second Henry's law constant,

$$H_{cc}^{s\to b} = \frac{[X_{(b)}]}{[X_{(ads)}]} = \frac{k_{sol}\delta}{k_{desol}\Gamma_{\infty}}, \tag{1.4}$$

where the solvation rate (k_{sol}) is computed from k_{des} and the mass accommodation coefficient,

$$\alpha = \frac{k_{sol}}{k_{sol}+k_{des}} \to k_{sol} = \frac{\alpha k_{des}}{1-\alpha} \tag{1.5}$$

From k_{sol} and $H_{cc}^{s\to b}$, k_{desol} is determined using Eq. (1.4).

A key feature of this framework is its minimal reliance on arbitrary assumptions. Instead, the compartment structure is informed by physical principles, and the kinetic parameters governing interfacial partitioning, accommodation, and diffusion can be constrained directly through molecular dynamics simulations. This dissertation builds upon the original framework by introducing targeted molecular dynamics simulations to quantify solvation energetics, interfacial concentrations, and transport rates. These simulations provide direct input for Henry's law constants, maximum surface site densities, system-specific interfacial thickness and kinetic coefficients, reducing uncertainty and improving the fidelity of the model.

The air-water interface represents perhaps the most ubiquitous, highly studied interfacial environment. A substantial body of experimental and theoretical work has focused on aqueous interfaces, where reaction acceleration is frequently attributed to the sharp dielectric transition between nonpolar air and highly polar water. This transition alters the local solvation environment, electric field strength, and hydrogen bonding network, all of which can significantly influence reaction pathways and energetics.[1–4,9,10,14,16,17,30] In contrast to the aqueous systems that dominate interfacial studies, the behavior of organic interfaces, despite their environmental abundance, remains far less explored.

Organic aerosols represent a major component of atmospheric particulate matter and have been extensively studied due to their central roles in air quality, radiative forcing, and human health.[31–33] Found in both primary and secondary forms, organic aerosols are chemically diverse and undergo dynamic processes that alter their physical and reactive properties. Despite this breadth of research, investigations into the molecular-level mechanisms that govern chemical transformations at the air–organic interfaces remain relatively sparse. In particular, little is known about how interfacial organization, solvation environments, and surface composition modulate reaction pathways in organic aerosols.

Recent simulation studies have begun to address this gap by probing the molecular organization and reactivity at air–organic interfaces, particularly in indoor environments.[34] Lakey et al.[35] demonstrated that reactions between ozone and squalene, an unsaturated skin lipid, can deplete ozone levels indoors while generating semi-volatile organic compounds that act as respiratory and dermal irritants. Their work highlighted the significance of interfacial reactivity in enclosed environments by integrating models that span spatial and temporal scales. A follow-up investigation by von Domaros et al.[36] employed molecular dynamics (MD) simulations and vibrational spectroscopy to investigate the molecular organization of squalene at the air-oil interface. They found that squalene chains preferentially align along the surface normal, leading to a nonuniform distribution of double bonds that may modulate local reactivity. Extending this

molecular-level understanding to predictive models, Zhou et al.[37] investigated the multiphase ozonolysis of oleic acid-based lipids, focusing on the quantitation of major products and using kinetic multilayer modeling to simulate triolein ozonolysis. This model was used to understand the reaction mechanism and kinetics, simulating reactions over a wide range of coating thicknesses and ozone levels. Shiraiwa et al.[38] developed a multiscale modeling framework (MOCCIE) that connects molecular parameters, such as surface accommodation coefficients and desorption lifetimes, directly to room-scale chemical dynamics. Their approach demonstrated how atomistic simulations can inform kinetic multilayer models of indoor air chemistry, bridging the gap between microscopic interfacial behavior and macroscopic chemical exposure predictions.

Although recent studies have begun to explore chemical transformations at organic interfaces, the molecular-level mechanisms driving interfacial reactivity remain poorly characterized. Clarifying how surface organization, composition, and solvation influence reaction kinetics is critical for advancing our understanding of multiphase chemistry. Systems such as squalene provide a valuable framework for uncovering general principles of interfacial catalysis across atmospheric and engineered environments.

Prior experimental studies have reported anomalous temperature dependence in the heterogeneous chlorination of small squalene aerosols,[39] suggesting that interfacial reactions might control the multiphase kinetics in this system. In Chapter 2 of this dissertation, we construct a kinetic model that is grounded in thermodynamic parameters extracted from molecular dynamics simulations. We demonstrate that this temperature dependence arises from an interfacial reaction rate that exceeds the bulk rate by two orders of magnitude. Diving deeper to search for a molecular origin for this acceleration, we identify a newly discovered mechanism termed "tail spearfishing" (Figure 1.3). This mechanism is a result of a collective thermodynamic driving force that increases the encounter frequency of chlorine with squalene double bonds at the interface. Our findings have broader implications that extend beyond this model system, suggesting that interfacial acceleration may be more ubiquitous than previously thought, particularly in non-polar solvents composed of long hydrocarbon chains. This challenges conventional thinking about where enhanced interfacial reactivity might occur and provides insights into a reaction mechanism distinct from those proposed for aqueous interfaces.

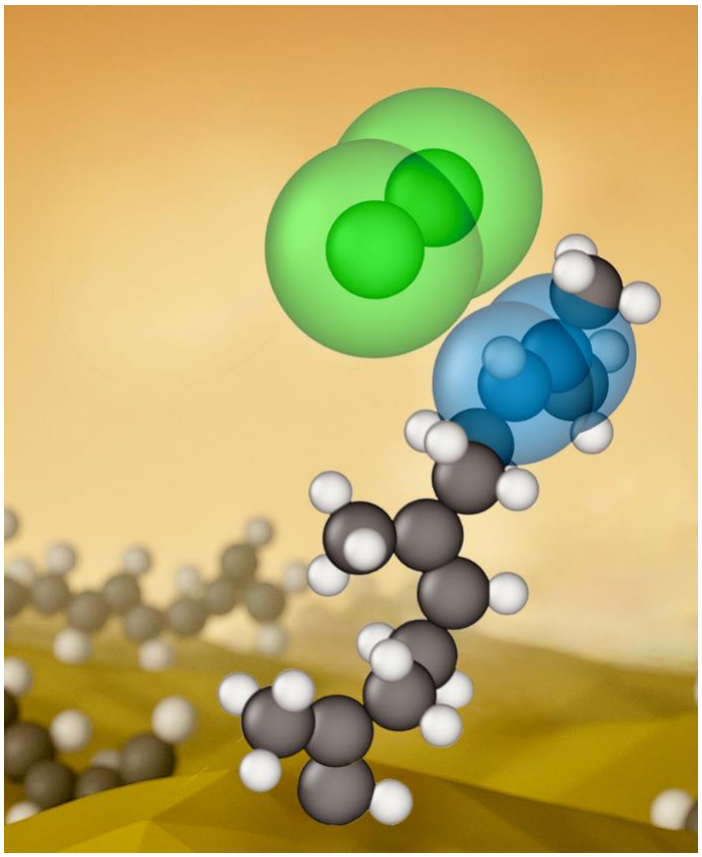

Figure 1.3 – "Tail spearfishing" mechanism, where squalene molecules that extend into the gas phase come in contact with chlorine with a greater probability.

Interfacial environments exhibit pronounced sensitivity to compositional changes. The introduction of solutes or solvent mixtures can alter surface structure, modify solvation energetics, and alter interfacial reactivity. Previous aerosol experiments have shown that the presence of oxygenated spectator species accelerates the heterogeneous chlorination of squalene,[39] even though the underlying reaction mechanism remains unchanged. In Chapter 3, we expand on our knowledge of the pure squalene system and use molecular dynamics simulations coupled with kinetic modeling to quantify the impact of alcohol addition on squalene chlorination. We find that long-chain alcohols, 2-decyl-1-tetradecanol, accumulate in a subsurface region beneath the interface, where they enhance chemical reactivity both at the surface and within the bulk. Specifically, the bulk reaction rate increases by an order of magnitude compared to the pure system rate, while the interfacial rate is accelerated by an additional two orders of magnitude relative to that bulk value. These results demonstrate how small compositional modifications can drive interfacial catalysis in multiphase systems.

The work presented in Chapters 2 and 3 establishes air–organic interfaces as catalytically active regions where structure, composition, and dynamics can drive substantial reaction rate enhancements. By combining molecular simulations with kinetic modeling, we show that alignment of long-chain organics, interfacial diffusion, and modest compositional changes, such as alcohol addition, can accelerate heterogeneous reactivity by several orders of magnitude.

1.2. Introduction - Fenton Chemistry

Since its discovery in 1894,[40] Fenton Chemistry has been highly studied due to its importance in biological processes and for its application as an advanced oxidation process in water remediation and wastewater treatment.[41–48] The formation mechanism and identity of the strong oxidant formed in this reaction continue to be actively debated. One interesting facet of this debate concerns Fenton chemistry at the air-water interface.

Enami et al.[49] claim that Fenton reactions proceed dramatically faster at the air–water interface than in bulk solution, by about four orders of magnitude, due to the formation of reactive ferryl (Fe(IV)) species rather than hydroxyl radicals. Using online electrospray mass spectrometry, they identify both mono- and poly-nuclear ferryl complexes generated when gaseous H_2O_2 or O_3 reacts with aqueous Fe^{2+} at the interface. This enhanced interfacial reactivity is attributed to unique solvation environments and altered coordination structures at the surface. In contrast, Gladich et al.[50] investigated the solvation structure and interfacial behavior of Fe^{2+} and Fe^{3+} ions involved in Fenton chemistry using a combination of photoelectron spectroscopy and molecular dynamics simulations. Their results show that both Fe^{2+} and Fe^{3+} prefer bulk solvation rather than enrichment at the liquid–gas interface. This study finds no evidence for distinct interfacial reaction pathways or ferryl intermediate formation at the interface. Instead, the observed oxidation of Fe^{2+} to Fe^{3+} is consistent with bulk phase chemistry. This report sparked a back-and-forth correspondence between the two research groups, as evidenced by comments published in the Journal of Physical Chemistry Letters.[51,52]

Motivated by this ongoing debate regarding interfacial Fenton chemistry and the general underlying mechanism of Fenton chemistry, we undertook a critical examination of the existing literature. While we were initially interested in examining Fenton reactivity at interfaces, we concluded that a detailed analysis of interfacial processes may be premature. This is primarily because the fundamental bulk-phase Fenton mechanism remains unresolved. In particular, the role of Fe(IV) as an intermediate is not well characterized, despite its frequent association with higher pH conditions in both experimental and computational studies.[53–59]

To clarify the pH dependence of this complex reaction, we reanalyzed a previously proposed kinetic model (Ref. [60]). Our investigation revealed that the model did not explicitly account for iron speciation, resulting in the use of unrealistic rate constants. By introducing proper speciation into the model, we identified a significantly faster formation rate of Fe(IV), on the order of 10^6 $M^{-1}s^{-1}$. This correction lays the foundation for a more mechanistically consistent kinetic framework capable of explaining the observed acceleration of Fenton chemistry as the system transitions from acidic to near-neutral pH (Figure 1.4).

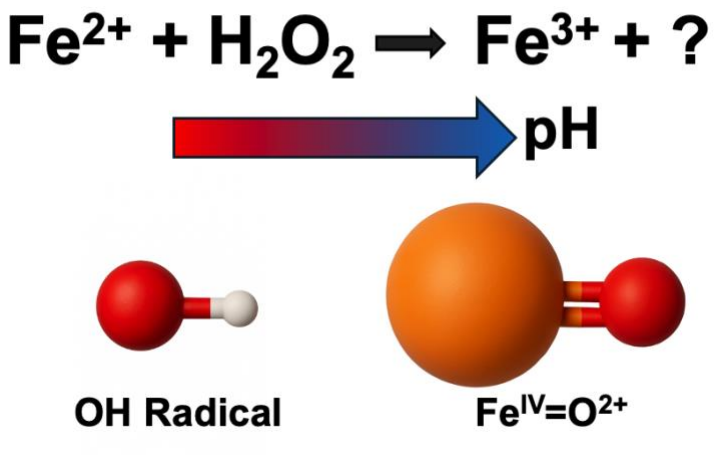

Figure 1.4 – Fenton mechanism pH dependence, neutral to higher pH values shift mechanism to form Fe(IV) oxidizing species.

Building on a prior kinetic modeling study that focused on constraining Fenton reactivity in the acidic regime[61], we extended the framework to encompass a broader pH range. This work culminates in the development of a unified kinetic model that describes the speciation-dependent mechanism of Fenton chemistry across acidic to neutral pH conditions. The model captures the observed acceleration of Fe(II) oxidation by hydrogen peroxide as the system shifts away from strongly acidic environments. The construction, validation, and implications of this unified model are detailed in Chapter 4 of this dissertation.

1.3. References

(1) Ruiz-Lopez, M. F.; Francisco, J. S.; Martins-Costa, M. T. C.; Anglada, J. M. Molecular Reactions at Aqueous Interfaces. *Nat. Rev. Chem.* **2020**, *4* (9), 459–475. https://doi.org/10.1038/s41570-020-0203-2.

(2) Wei, Z.; Li, Y.; Cooks, R. G.; Yan, X. Accelerated Reaction Kinetics in Microdroplets: Overview and Recent Developments. *Annu. Rev. Phys. Chem.* **2020**, *71* (Volume 71, 2020), 31–51. https://doi.org/10.1146/annurev-physchem-121319-110654.

(3) Ahmed, M.; Blum, M.; Crumlin, E. J.; Geissler, P. L.; Head-Gordon, T.; Limmer, D. T.; Mandadapu, K. K.; Saykally, R. J.; Wilson, K. R. Molecular Properties and Chemical Transformations Near Interfaces. *J. Phys. Chem. B* **2021**, *125* (32), 9037–9051. https://doi.org/10.1021/acs.jpcb.1c03756.

(4) LaCour, R. A.; Heindel, J. P.; Zhao, R.; Head-Gordon, T. The Role of Interfaces and Charge for Chemical Reactivity in Microdroplets. *J. Am. Chem. Soc.* **2025**, *147* (8), 6299–6317. https://doi.org/10.1021/jacs.4c15493.

(5) Knipping, E. M.; Lakin, M. J.; Foster, K. L.; Jungwirth, P.; Tobias, D. J.; Gerber, R. B.; Dabdub, D.; Finlayson-Pitts, B. J. Experiments and Simulations of Ion-Enhanced Interfacial Chemistry on Aqueous NaCl Aerosols. *Science* **2000**, *288* (5464), 301–306. https://doi.org/10.1126/science.288.5464.301.

(6) Jang, M.; Czoschke, N. M.; Lee, S.; Kamens, R. M. Heterogeneous Atmospheric Aerosol Production by Acid-Catalyzed Particle-Phase Reactions. *Science* **2002**, *298* (5594), 814–817. https://doi.org/10.1126/science.1075798.

(7) Kumar, M.; Trabelsi, T.; Gómez Martín, J. C.; Saiz-Lopez, A.; Francisco, J. S. HIOx–IONO2 Dynamics at the Air–Water Interface: Revealing the Existence of a Halogen Bond at the Atmospheric Aerosol Surface. *J. Am. Chem. Soc.* **2020**, *142* (28), 12467–12477. https://doi.org/10.1021/jacs.0c05232.

(8) Kumar, M.; Zhong, J.; Zeng, X. C.; Francisco, J. S. Reaction of Criegee Intermediate with Nitric Acid at the Air–Water Interface. *J. Am. Chem. Soc.* **2018**, *140* (14), 4913–4921. https://doi.org/10.1021/jacs.8b01191.

(9) Hoehn, R. D.; Carignano, M. A.; Kais, S.; Zhu, C.; Zhong, J.; Zeng, X. C.; Francisco, J. S.; Gladich, I. Hydrogen Bonding and Orientation Effects on the Accommodation of Methylamine at the Air-Water Interface. *J. Chem. Phys.* **2016**, *144* (21), 214701. https://doi.org/10.1063/1.4950951.

(10) Galib, M.; Limmer, D. T. Reactive Uptake of N2O5 by Atmospheric Aerosol Is Dominated by Interfacial Processes. *Science* **2021**, *371* (6532), 921–925. https://doi.org/10.1126/science.abd7716.

(11) Moon, S.; Limmer, D. T. Enhanced ClNO2 Formation at the Interface of Sea-Salt Aerosol. *J. Phys. Chem. Lett.* **2024**, *15* (37), 9466–9473. https://doi.org/10.1021/acs.jpclett.4c02289.

(12) Moise, T.; Rudich, Y. Uptake of Cl and Br by Organic Surfaces—A Perspective on Organic Aerosols Processing by Tropospheric Oxidants. *Geophys. Res. Lett.* **2001**, *28* (21), 4083–4086. https://doi.org/10.1029/2001GL013583.

(13) M. Prophet, A.; Polley, K.; Berkel, G. J. V.; T. Limmer, D.; R. Wilson, K. Iodide Oxidation by Ozone at the Surface of Aqueous Microdroplets. *Chem. Sci.* **2024**, *15* (2), 736–756. https://doi.org/10.1039/D3SC04254E.

(14) Gong, C.; Yuan, X.; Xing, D.; Zhang, D.; Martins-Costa, M. T. C.; Anglada, J. M.; Ruiz-López, M. F.; Francisco, J. S.; Zhang, X. Fast Sulfate Formation Initiated by the Spin-

Forbidden Excitation of SO2 at the Air–Water Interface. *J. Am. Chem. Soc.* **2022**, *144* (48), 22302–22308. https://doi.org/10.1021/jacs.2c10830.
(15) Zhong, J.; Zhao, Y.; Li, L.; Li, H.; Francisco, J. S.; Zeng, X. C. Interaction of the NH2 Radical with the Surface of a Water Droplet. *J. Am. Chem. Soc.* **2015**, *137* (37), 12070–12078. https://doi.org/10.1021/jacs.5b07354.
(16) Zhu, C.; Kumar, M.; Zhong, J.; Li, L.; Francisco, J. S.; Zeng, X. C. New Mechanistic Pathways for Criegee–Water Chemistry at the Air/Water Interface. *J. Am. Chem. Soc.* **2016**, *138* (35), 11164–11169. https://doi.org/10.1021/jacs.6b04338.
(17) Fang, Y.-G.; Wei, L.; Francisco, J. S.; Zhu, C.; Fang, W.-H. Mechanistic Insights into Chloric Acid Production by Hydrolysis of Chlorine Trioxide at an Air–Water Interface. *J. Am. Chem. Soc.* **2024**, *146* (30), 21052–21060. https://doi.org/10.1021/jacs.4c06269.
(18) Jelinek, R.; Okada, S.; Norvez, S.; Charych, D. Interfacial Catalysis by Phospholipases at Conjugated Lipid Vesicles: Colorimetric Detection and NMR Spectroscopy. *Chem. Biol.* **1998**, *5* (11), 619–629. https://doi.org/10.1016/S1074-5521(98)90290-3.
(19) Narayan, S.; Muldoon, J.; Finn, M. G.; Fokin, V. V.; Kolb, H. C.; Sharpless, K. B. "On Water": Unique Reactivity of Organic Compounds in Aqueous Suspension. *Angew. Chem. Int. Ed.* **2005**, *44* (21), 3275–3279. https://doi.org/10.1002/anie.200462883.
(20) Song, X.; Basheer, C.; Zare, R. N. Making Ammonia from Nitrogen and Water Microdroplets. *Proc. Natl. Acad. Sci.* **2023**, *120* (16), e2301206120. https://doi.org/10.1073/pnas.2301206120.
(21) Davidovits, P.; Kolb, C. E.; Williams, L. R.; Jayne, J. T.; Worsnop, D. R. Mass Accommodation and Chemical Reactions at Gas−Liquid Interfaces. *Chem. Rev.* **2006**, *106* (4), 1323–1354. https://doi.org/10.1021/cr040366k.
(22) Kolb, C. E.; Cox, R. A.; Abbatt, J. P. D.; Ammann, M.; Davis, E. J.; Donaldson, D. J.; Garrett, B. C.; George, C.; Griffiths, P. T.; Hanson, D. R.; Kulmala, M.; McFiggans, G.; Pöschl, U.; Riipinen, I.; Rossi, M. J.; Rudich, Y.; Wagner, P. E.; Winkler, P. M.; Worsnop, D. R.; O' Dowd, C. D. An Overview of Current Issues in the Uptake of Atmospheric Trace Gases by Aerosols and Clouds. *Atmospheric Chem. Phys.* **2010**, *10* (21), 10561–10605. https://doi.org/10.5194/acp-10-10561-2010.
(23) Finlayson-Pitts, B. J.; Pitts, J. N. *Chemistry of the Upper and Lower Atmosphere: Theory, Experiments, and Applications*; Academic Press: San Diego, 2000.
(24) Lakey, P. S. J.; Eichler, C. M. A.; Wang, C.; Little, J. C.; Shiraiwa, M. Kinetic Multi-layer Model of Film Formation, Growth, and Chemistry (KM-FILM): Boundary Layer Processes, Multi-layer Adsorption, Bulk Diffusion, and Heterogeneous Reactions. *Indoor Air* **2021**, *31* (6), 2070–2083. https://doi.org/10.1111/ina.12854.
(25) Ingram, S.; Rovelli, G.; Song, Y.-C.; Topping, D.; Dutcher, C. S.; Liu, S.; Nandy, L.; Shiraiwa, M.; Reid, J. P. Accurate Prediction of Organic Aerosol Evaporation Using Kinetic Multilayer Modeling and the Stokes–Einstein Equation. *J. Phys. Chem. A* **2021**, *125* (16), 3444–3456. https://doi.org/10.1021/acs.jpca.1c00986.
(26) Berkemeier, T.; Huisman, A. J.; Ammann, M.; Shiraiwa, M.; Koop, T.; Pöschl, U. Kinetic Regimes and Limiting Cases of Gas Uptake and Heterogeneous Reactions in Atmospheric Aerosols and Clouds: A General Classification Scheme. *Atmospheric Chem. Phys.* **2013**, *13* (14), 6663–6686. https://doi.org/10.5194/acp-13-6663-2013.
(27) Shiraiwa, M.; Pfrang, C.; Pöschl, U. Kinetic Multi-Layer Model of Aerosol Surface and Bulk Chemistry (KM-SUB): The Influence of Interfacial Transport and Bulk Diffusion on

the Oxidation of Oleic Acid by Ozone. *Atmospheric Chem. Phys.* **2010**, *10* (8), 3673–3691. https://doi.org/10.5194/acp-10-3673-2010.
(28) Willis, M. D.; Wilson, K. R. Coupled Interfacial and Bulk Kinetics Govern the Timescales of Multiphase Ozonolysis Reactions. *J. Phys. Chem. A* **2022**, *126* (30), 4991–5010. https://doi.org/10.1021/acs.jpca.2c03059.
(29) Vácha, R.; Slavíček, P.; Mucha, M.; Finlayson-Pitts, B. J.; Jungwirth, P. Adsorption of Atmospherically Relevant Gases at the Air/Water Interface: Free Energy Profiles of Aqueous Solvation of N2, O2, O3, OH, H2O, HO2, and H2O2. *J. Phys. Chem. A* **2004**, *108* (52), 11573–11579. https://doi.org/10.1021/jp046268k.
(30) Björneholm, O.; Hansen, M. H.; Hodgson, A.; Liu, L.-M.; Limmer, D. T.; Michaelides, A.; Pedevilla, P.; Rossmeisl, J.; Shen, H.; Tocci, G.; Tyrode, E.; Walz, M.-M.; Werner, J.; Bluhm, H. Water at Interfaces. *Chem. Rev.* **2016**, *116* (13), 7698–7726. https://doi.org/10.1021/acs.chemrev.6b00045.
(31) Hallquist, M.; Wenger, J. C.; Baltensperger, U.; Rudich, Y.; Simpson, D.; Claeys, M.; Dommen, J.; Donahue, N. M.; George, C.; Goldstein, A. H.; Hamilton, J. F.; Herrmann, H.; Hoffmann, T.; Iinuma, Y.; Jang, M.; Jenkin, M. E.; Jimenez, J. L.; Kiendler-Scharr, A.; Maenhaut, W.; McFiggans, G.; Mentel, T. F.; Monod, A.; Prévôt, A. S. H.; Seinfeld, J. H.; Surratt, J. D.; Szmigielski, R.; Wildt, J. The Formation, Properties and Impact of Secondary Organic Aerosol: Current and Emerging Issues. *Atmospheric Chem. Phys.* **2009**, *9* (14), 5155–5236. https://doi.org/10.5194/acp-9-5155-2009.
(32) Jimenez, J. L.; Canagaratna, M. R.; Donahue, N. M.; Prevot, A. S. H.; Zhang, Q.; Kroll, J. H.; DeCarlo, P. F.; Allan, J. D.; Coe, H.; Ng, N. L.; Aiken, A. C.; Docherty, K. S.; Ulbrich, I. M.; Grieshop, A. P.; Robinson, A. L.; Duplissy, J.; Smith, J. D.; Wilson, K. R.; Lanz, V. A.; Hueglin, C.; Sun, Y. L.; Tian, J.; Laaksonen, A.; Raatikainen, T.; Rautiainen, J.; Vaattovaara, P.; Ehn, M.; Kulmala, M.; Tomlinson, J. M.; Collins, D. R.; Cubison, M. J.; Dunlea, E. J.; Huffman, J. A.; Onasch, T. B.; Alfarra, M. R.; Williams, P. I.; Bower, K.; Kondo, Y.; Schneider, J.; Drewnick, F.; Borrmann, S.; Weimer, S.; Demerjian, K.; Salcedo, D.; Cottrell, L.; Griffin, R.; Takami, A.; Miyoshi, T.; Hatakeyama, S.; Shimono, A.; Sun, J. Y.; Zhang, Y. M.; Dzepina, K.; Kimmel, J. R.; Sueper, D.; Jayne, J. T.; Herndon, S. C.; Trimborn, A. M.; Williams, L. R.; Wood, E. C.; Middlebrook, A. M.; Kolb, C. E.; Baltensperger, U.; Worsnop, D. R. Evolution of Organic Aerosols in the Atmosphere. *Science* **2009**, *326* (5959), 1525–1529. https://doi.org/10.1126/science.1180353.
(33) Pöschl, U. Atmospheric Aerosols: Composition, Transformation, Climate and Health Effects. *Angew. Chem. Int. Ed.* **2005**, *44* (46), 7520–7540. https://doi.org/10.1002/anie.200501122.
(34) Domaros, M. von; Tobias, D. J. Molecular Dynamics Simulations of the Interactions of Organic Compounds at Indoor Relevant Surfaces. *Annu. Rev. Phys. Chem.* **2025**, *76* (Volume 76, 2025), 231–250. https://doi.org/10.1146/annurev-physchem-083122-123017.
(35) Lakey, P. S. J.; Morrison, G. C.; Won, Y.; Parry, K. M.; von Domaros, M.; Tobias, D. J.; Rim, D.; Shiraiwa, M. The Impact of Clothing on Ozone and Squalene Ozonolysis Products in Indoor Environments. *Commun. Chem.* **2019**, *2* (1), 1–8. https://doi.org/10.1038/s42004-019-0159-7.
(36) von Domaros, M.; Liu, Y.; Butman, J. L.; Perlt, E.; Geiger, F. M.; Tobias, D. J. Molecular Orientation at the Squalene/Air Interface from Sum Frequency Generation Spectroscopy and Atomistic Modeling. *J. Phys. Chem. B* **2021**, *125* (15), 3932–3941. https://doi.org/10.1021/acs.jpcb.0c11158.

(37) Zhou, Z.; Lakey, P. S. J.; von Domaros, M.; Wise, N.; Tobias, D. J.; Shiraiwa, M.; Abbatt, J. P. D. Multiphase Ozonolysis of Oleic Acid-Based Lipids: Quantitation of Major Products and Kinetic Multilayer Modeling. *Environ. Sci. Technol.* **2022**, *56* (12), 7716–7728. https://doi.org/10.1021/acs.est.2c01163.
(38) Shiraiwa, M.; Carslaw, N.; Tobias, D. J.; Waring, M. S.; Rim, D.; Morrison, G.; Lakey, P. S. J.; Kruza, M.; Domaros, M. von; Cummings, B. E.; Won, Y. Modelling Consortium for Chemistry of Indoor Environments (MOCCIE): Integrating Chemical Processes from Molecular to Room Scales. *Environ. Sci. Process. Impacts* **2019**, *21* (8), 1240–1254. https://doi.org/10.1039/C9EM00123A.
(39) Zeng, M.; Wilson, K. R. Experimental Evidence That Halogen Bonding Catalyzes the Heterogeneous Chlorination of Alkenes in Submicron Liquid Droplets. *Chem. Sci.* **2021**, *12* (31), 10455–10466. https://doi.org/10.1039/D1SC02662C.
(40) Fenton, H. J. H. LXXIII.—Oxidation of Tartaric Acid in Presence of Iron. *J. Chem. Soc. Trans.* **1894**, *65* (0), 899–910. https://doi.org/10.1039/CT8946500899.
(41) Prousek, J. Fenton Chemistry in Biology and Medicine. *Pure Appl. Chem.* **2007**. https://doi.org/10.1351/pac200779122325.
(42) Deguillaume, L.; Leriche, M.; Chaumerliac, N. Impact of Radical versus Non-Radical Pathway in the Fenton Chemistry on the Iron Redox Cycle in Clouds. *Chemosphere* **2005**, *60* (5), 718–724. https://doi.org/10.1016/j.chemosphere.2005.03.052.
(43) A. Al-Abadleh, H. Review of the Bulk and Surface Chemistry of Iron in Atmospherically Relevant Systems Containing Humic-like Substances. *RSC Adv.* **2015**, *5* (57), 45785–45811. https://doi.org/10.1039/C5RA03132J.
(44) Siefert, R. L.; Pehkonen, S. O.; Erel, Y.; Hoffmann, M. R. Iron Photochemistry of Aqueous Suspensions of Ambient Aerosol with Added Organic Acids. *Geochim. Cosmochim. Acta* **1994**, *58* (15), 3271–3279. https://doi.org/10.1016/0016-7037(94)90055-8.
(45) Babuponnusami, A.; Muthukumar, K. A Review on Fenton and Improvements to the Fenton Process for Wastewater Treatment. *J. Environ. Chem. Eng.* **2014**, *2* (1), 557–572. https://doi.org/10.1016/j.jece.2013.10.011.
(46) Bigda, R. J. Consider Fenton`s Chemistry for Wastewater Treatment. *Chem. Eng. Prog.* **1995**, *91* (12).
(47) Wardman, P.; Candeias, L. P. Fenton Chemistry: An Introduction. *Radiat. Res.* **1996**, *145* (5), 523–531. https://doi.org/10.2307/3579270.
(48) Walling, C. Fenton's Reagent Revisited. *Acc. Chem. Res.* **1975**, *8* (4), 125–131. https://doi.org/10.1021/ar50088a003.
(49) Enami, S.; Sakamoto, Y.; Colussi, A. J. Fenton Chemistry at Aqueous Interfaces. *Proc. Natl. Acad. Sci.* **2014**, *111* (2), 623–628. https://doi.org/10.1073/pnas.1314885111.
(50) Gladich, I.; Chen, S.; Yang, H.; Boucly, A.; Winter, B.; van Bokhoven, J. A.; Ammann, M.; Artiglia, L. Liquid–Gas Interface of Iron Aqueous Solutions and Fenton Reagents. *J. Phys. Chem. Lett.* **2022**, *13* (13), 2994–3001. https://doi.org/10.1021/acs.jpclett.2c00380.
(51) Colussi, A. J.; Enami, S. Comment on "Liquid–Gas Interface of Iron Aqueous Solutions and Fenton Reagents." *J. Phys. Chem. Lett.* **2022**, *13* (29), 6680–6680. https://doi.org/10.1021/acs.jpclett.2c01006.
(52) Gladich, I.; Chen, S.; Yang, H.; Boucly, A.; Winter, B.; van Bokhoven, J. A.; Ammann, M.; Artiglia, L. Reply to "Comment on 'Liquid–Gas Interface of Iron Aqueous Solutions and Fenton Reagents.'" *J. Phys. Chem. Lett.* **2022**, *13* (29), 6681–6682. https://doi.org/10.1021/acs.jpclett.2c01391.

(53) Rush, J. D.; Koppenol, W. H. Reactions of Iron(II) Nitrilotriacetate and Iron(II) Ethylenediamine-N,N'-Diacetate Complexes with Hydrogen Peroxide. *J. Am. Chem. Soc.* **1988**, *110* (15), 4957–4963. https://doi.org/10.1021/ja00223a013.
(54) Bossmann, S. H.; Oliveros, E.; Göb, S.; Siegwart, S.; Dahlen, E. P.; Payawan, L.; Straub, M.; Wörner, M.; Braun, A. M. New Evidence against Hydroxyl Radicals as Reactive Intermediates in the Thermal and Photochemically Enhanced Fenton Reactions. *J. Phys. Chem. A* **1998**, *102* (28), 5542–5550. https://doi.org/10.1021/jp980129j.
(55) Kremer, M. L. Mechanism of the Fenton Reaction. Evidence for a New Intermediate. *Phys. Chem. Chem. Phys.* **1999**, *1* (15), 3595–3605. https://doi.org/10.1039/A903915E.
(56) Buda, F.; Ensing, B.; Gribnau, M. C. M.; Baerends, E. J. DFT Study of the Active Intermediate in the Fenton Reaction. *Chem. – Eur. J.* **2001**, *7* (13), 2775–2783. https://doi.org/10.1002/1521-3765(20010702)7:13<2775::AID-CHEM2775>3.0.CO;2-6.
(57) Ensing, B.; Buda, F.; Blöchl, P.; Baerends, E. J. Chemical Involvement of Solvent Water Molecules in Elementary Steps of the Fenton Oxidation Reaction. *Angew. Chem. Int. Ed.* **2001**, *40* (15), 2893–2895. https://doi.org/10.1002/1521-3773(20010803)40:15<2893::AID-ANIE2893>3.0.CO;2-B.
(58) Ensing, B.; Buda, F.; Blöchl, P. E.; Baerends, E. J. A Car–Parrinello Study of the Formation of Oxidizing Intermediates from Fenton's Reagent in Aqueous Solution. *Phys. Chem. Chem. Phys.* **2002**, *4* (15), 3619–3627. https://doi.org/10.1039/B201864K.
(59) Ensing, B.; Buda, F.; Gribnau, M. C. M.; Baerends, E. J. Methane-to-Methanol Oxidation by the Hydrated Iron(IV) Oxo Species in Aqueous Solution: A Combined DFT and Car−Parrinello Molecular Dynamics Study. *J. Am. Chem. Soc.* **2004**, *126* (13), 4355–4365. https://doi.org/10.1021/ja038865a.
(60) Bataineh, H.; Pestovsky, O.; Bakac, A. pH-Induced Mechanistic Changeover from Hydroxyl Radicals to Iron(IV) in the Fenton Reaction. *Chem. Sci.* **2012**, *3* (5), 1594–1599. https://doi.org/10.1039/C2SC20099F.
(61) Stanbury, D. M. The Principle of Detailed Balancing, the Iron-Catalyzed Disproportionation of Hydrogen Peroxide, and the Fenton Reaction. *Dalton Trans.* **2022**, *51* (6), 2135–2157. https://doi.org/10.1039/D1DT03645A.

Chapter 2. Accelerated Surface Reaction of Chlorine with Squalene Revealed by Molecular Simulations and Kinetic Modeling

This chapter is adapted from Cohen, L.; Dodin, A.; Wilson, K.; Limmer, D. Accelerated chlorination at the surface of organic aerosol* **2025. DOI:10.26434/chemrxiv-2025-r0wcd.

2.1. Introduction

Liquid interfaces are nano-environments that differ significantly from bulk liquids. A growing body of theoretical and experimental evidence has shown that the unique properties of *aqueous* interfaces can dramatically accelerate chemical reactions,[1–4] with significant implications, e.g., in atmospheric chemistry where emergent reactions at the air-water interface governs reactivity of aerosols,[5–11] and in chemical synthesis where reaction acceleration at interfaces promises to use water as the ultimate green catalyst.[12,13] In this work, we show that such reaction rate acceleration is not unique to aqueous interfaces and emerges in the chlorination of squalene nano-droplets, at a nonpolar liquid-vapor interface. Unlike some previous observations for rection acceleration at interfaces, this reaction 1) occurs with the solvent itself and not a solute that can show modified interfacial concentrations or phase seperation,[14,15] and 2) occurs at an interface without a significant dielectric variation and therefore without substantial modification to interfacial electric fields, eliminating the two primary explanations for reaction acceleration at aqueous interfaces. Instead, we show using a combination of kinetic modeling and molecular dynamics simulations that previously reported anomalous temperature dependence of squalene chlorination rates in aerosols originates from an interfacial reaction rate that is two orders of magnitude faster than the bulk. This acceleration results from a combination of faster chlorine diffusion at the interface and an increased encounter probability between chlorine and carbon double bonds, driven by the unique solvation environment produced by the interfacial alignment of squalene molecules, where squalene tails extend in a spearfishing action to interact with chlorine out into the gas phase. Our analysis provides an insight into interfacial reaction acceleration that goes beyond this model system, revealing a new mechanism that can arise in non-polar solvents consisting of long hydrocarbon chains. Our work suggests that interfacial acceleration may occur in a broader range of interfaces than previously expected.

The characteristic length-scale for a multiphase reaction like the chlorination of squalene is the reacto-diffusive length,[16] l defined as,

$$l = \sqrt{\frac{D}{k_{\mathrm{rxn}}}}, \tag{2.1}$$

where D is the liquid phase diffusion constant of chlorine (Cl_2) and k_{rxn} is the pseudo first order rate constant for the addition of chlorine to a squalene carbon double bond. For fast reactions, l is short and reactivity occurs at the surface or in the near surface region, implying that the molecular details of how gas phase Cl_2 transits the interface play a significant role in the heterogeneous reaction. For slower reactions, where the reacto-diffusive length is longer than the aerosol or

droplet dimensions, the reactivity is expected to be controlled by the bulk solubility and reactivity of Cl_2, with the interface playing a more minor role.

Direct measurement of squalene chlorination in small aerosol particles was previously conducted in flow tube experiments and detected by mass spectrometry.[17] Curiously, the experiments showed an increase in the observed heterogeneous reaction rate with decreasing temperature, which is in contrast with bulk measurements for similar alkenes, in which higher temperatures lead to faster reaction rates.[18,19] Estimates of the uptake coefficient can be made using the resistor model[20] and compared to the experimental results (Figure 2.1).

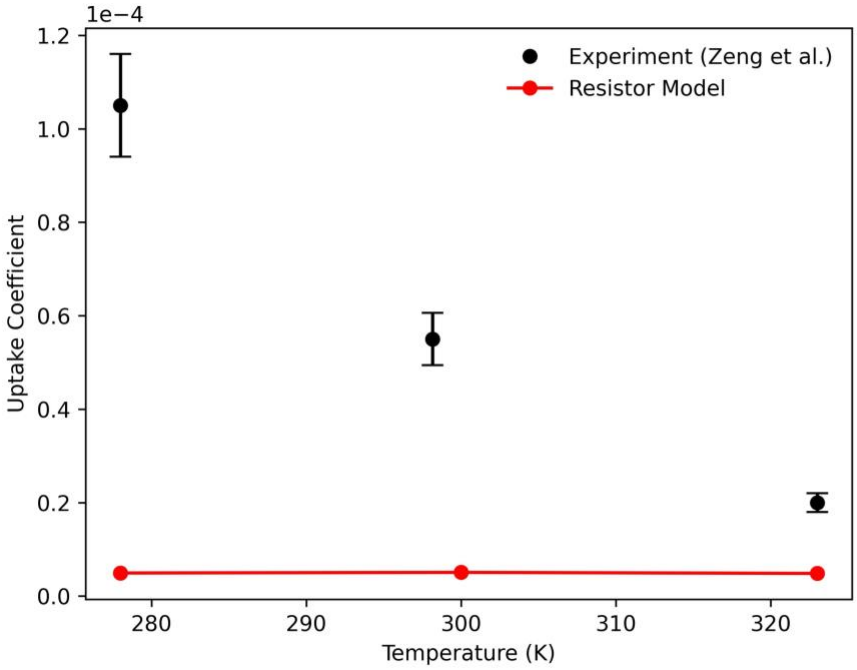

Figure 2.1. Uptake coefficient as a function of temperature for the heterogeneous chlorination of squalene. Experimental uptake coefficients reproduced from Zeng et al. (ref [17]) are shown in black whereas resistor model estimates are shown in red.

The resistor model predicts a kinetic trend that is invariant with temperature due to compensating factors: the increased solubility of Cl2 (i.e. increasing Henry's law constant) with decreasing temperature and the decrease in $k_{rxn}$with decreasing temperature. The lack of agreement with the aerosol experiments suggests an interfacial contribution to the reactive uptake that is not captured by the resistor model. Yet, The reacto-diffusive length for squalene chlorination, based on the experimentally observed rate and chlorine diffusion constant, is double the aerosol diameter used in the experiment, pointing to bulk reactivity.[17] This contradiction motivated the theoretical investigation presented in this paper.

2.2. Methods

Classical molecular dynamics simulations were conducted in LAMMPS [21] using 288 squalene molecules in a slab geometry. A liquid region (~60Å) is enclosed by two interfaces along the *z* axis with periodic boundary conditions in all directions. The total box dimension is 60 X 60 X 240 Å. The molecular force field for squalene is taken from the Automated Topology Builder

repository, [22] optimized for GROMOS_54A7.[23] The force field yielded the most accurate liquid density and C-C bond lengths. Simulations are conducted in the canonical ensemble with a fixed number of particles, volume, and temperature T using the velocity-Verlet integrator with 2 fs timesteps. Temperature is controlled at 300K using a Langevin thermostat with a 1 ps relaxation time. Carbon-hydrogen bonds are constrained using the RATTLE algorithm.[24] Short-range interactions are described by a Lennard-Jones (LJ) potential truncated at 14Å, $U_{LJ}(r) = 4\varepsilon_{ij}\left[\left(\frac{\sigma_{ij}}{r}\right)^{12} - \left(\frac{\sigma_{ij}}{r}\right)^{6}\right]$, where ε_{ij} and σ_{ij} are the energy and size parameters described in GROMOS_54A7, and r is the distance between atoms. Long range Coulomb interactions are described by particle–particle–particle–mesh method [25] with a relative error of 10^{-4}. Initial configurations were generated by PACKMOL [26] and equilibrated for 50ns prior to production runs. The PMF for chlorine solvation in squalene is estimated from umbrella sampling using a biasing potential acting on the chlorine's center of mass $U_{bias}(z) = \frac{1}{2}k(z - z_0)^2$, where k is the spring constant. A list of the biased simulation windows and spring constants is presented in Table S2. Reconstruction of the PMF from the biased simulations was done using the Grossfield [27] implementation of the Weighted Histogram Analysis Method (WHAM).[28,29] 2D-PMF was constructed similarly using a biasing potential of the form $U_{bias}(z, R) = \frac{1}{2}k(z - z_0)^2 + \frac{1}{2}k(R - R_0)^2$, and a spring constant of $k = 5$ kcal/mol/Å^2, for biased production runs of 10 ns, at $31 \leq z \leq 26$Å, for the bulk liquid region, and at $-8 \leq z \leq 1$Å, for the interfacial region, with bias windows spaced by 0.5 Å. Bulk diffusivities are calculated from 150ns simulation trajectories using mean-squared displacement analysis limited to the bulk region $41 < \mathrm{z} < 21$ Å) $D = \lim_{t\to\infty} \frac{\langle |r(t) - r_0|^2 \rangle}{6\,t}$, where r is the center of mass position, D is the diffusion constant, and t is time. The mass accommodation coefficient was calculated from recording trajectory outcomes after placing chlorine at the Gibbs dividing surface $\alpha = \frac{n_\mathrm{b}}{n_\mathrm{g} + n_\mathrm{b}}$, where n_b is the number of trajectories where chlorine enters the bulk region of the liquid and n_g is the number of trajectories where chlorine enters the gas region. Gas, or liquid regions of the simulation, are defined as 10Å below or above the Gibbs dividing surface.

2.3. Results and Discussion

To examine the molecular details of chlorine gas adsorption and solvation at the air/squalene interface, we construct the potential of mean force (PMF) for chlorine solvation in squalene at room temperature as a function of the position z, the coordinate perpendicular to the liquid-vapor interface. The PMF is computed as,

$$F(z) = -k_\mathrm{B}T \ln\langle \delta(z - z_0) \rangle + F_0, \tag{2.2}$$

where k_B is Boltzmann's constant, T is temperature, and the angle brackets represent an ensemble average for chlorine's center of mass z_0. F_0 is the reference free energy set to zero at the gas phase. The PMF of chlorine solvation in squalene is shown in Figure 2.2A. It exhibits a minimum at the interface of ~0.5 kcal/mol, making Cl_2 about twice as likely to accumulate at the surface than in the bulk. The dimensionless Henry's law constant is calculated from the PMF by,

$$H_{cc}^{x\to y} = e^{-\frac{\Delta G_{x\to y}}{k_\mathrm{B}T}}, \tag{2.3}$$

where $\Delta G_{x\to y}$ is the free energy difference between regions. The resulting Henry's law constants for Cl_2 partitioning between gas and surface is $H_{cc}^{g\to s} = 13.24$, and that between the surface and bulk is $H_{cc}^{s\to b} = 0.45$, and the overall gas to bulk Henry's law constant is $H_{cc}^{g\to b} = 6.02$. To the best of our knowledge, there are no direct experimental measurements of the Cl_2 solubility in squalene, but our computed value is consistent with those for other organic liquids, such as $H_{cc}^{g\to b} = 9$ (decane), $H_{cc}^{g\to b} = 4$ (benzene), and $H_{cc}^{g\to b} = 8$ (cyclohexane).[30]

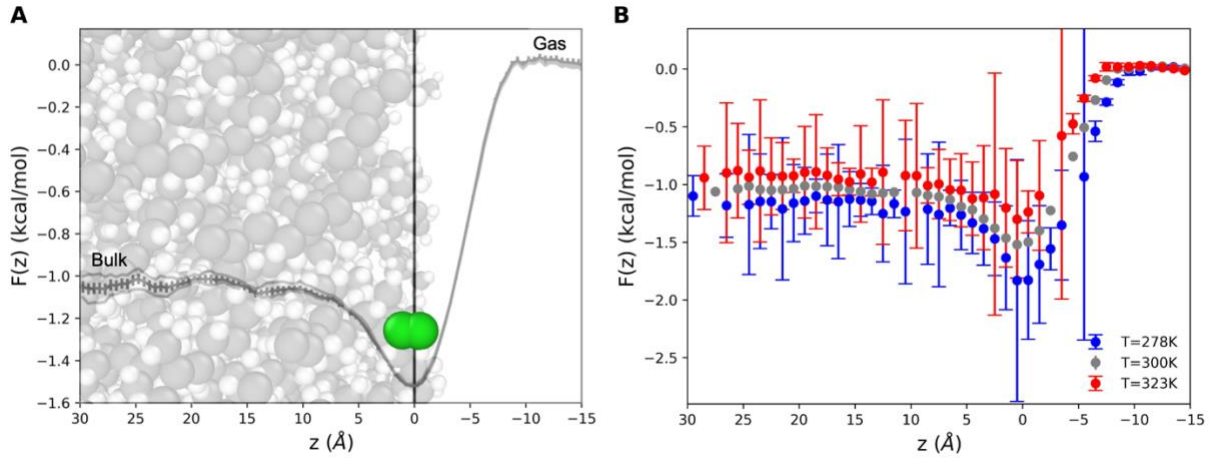

Figure 2.2. (A) The potential of mean force (PMF) for chlorine solvation in squalene as a function of distance, z, from the average interface at room temperature. Light grey line represents half the data to exemplify PMF precision. The Gibbs Dividing surface is at $z = 0$ Å, with positive and negative z values corresponding to the bulk liquid and gas regions, respectively. (*Inset*) MD snapshot of squalene slab, carbons are shown in grey and hydrogens in white. (B) PMF as function of the temperatures used in previous in aerosol experiments: 278K (blue), 300K (grey), and 323K (red), error bars represent standard error.

To explore how chlorine solvation changes with temperature, we employ the method of Souaille and Roux[31] to compute the enthalpy profile along the slab axis z from the Weighted Histogram Analysis Method (WHAM)[27–29] weighted average of the potential energy. By decomposing the enthalpic and entropic contributions to the PMF at room temperature, we can calculate a PMF at a given temperature to match the conditions used in the experiment. The standard error generated from this process is inherently larger, thus a comparison between the estimated PMF at 323K and a directly simulated one is shown in Figure 2.S3, to provide assurance of this method's accuracy. Over the 45K temperature range of the experiment, there is a prominent change in the PMFs as shown in Figure 2.2B. At 323K, the difference in solvation energy between the gas and surface is smaller than at room temperature, leading to overall less chlorine solvation in the aerosol, and faster solvation and desorption times from the interface. At low temperatures (278K), the interface plays a more pronounced role. The free energy minima is both wider and deeper than at room temperature, leading to an overall broader interfacial region and higher concentration of chlorine at the interface. Chlorine's lower thermal kinetic energy together with larger free energy differences between the surface and the bulk or gas, leads to slower desorption and solvation times that increase chlorine residence time at the interface. Consequently, Cl_2 is kinetically and thermodynamically enhanced at the interface at lower temperatures. Similar to the room temperature data, a temperature dependent mass accommodation coefficient can be computed by sampling system configurations at the higher, and/or lower temperatures.

We model the temperature dependent reaction kinetics of squalene chlorination in aerosols using a framework developed by Willis and Wilson[32] and implemented in Kinetiscope,[33] which describes an aerosol particle as comprised of two reaction compartments: surface and bulk. The bulk reaction rate is estimated from chlorine addition to oleic acid in a non-polar solvent, since to our best knowledge there are no literature reports of addition to squalene. All other model parameters are directly constrained from molecular models such as using the Henry's law constants extracted from the PMF and the mass accommodation. Complete model assumptions and parameters are provided in the Supporting Information. By changing the surface rate constant, we can use the model as a predictive tool to assess the surface rate enhancement required to explain the experimental result.

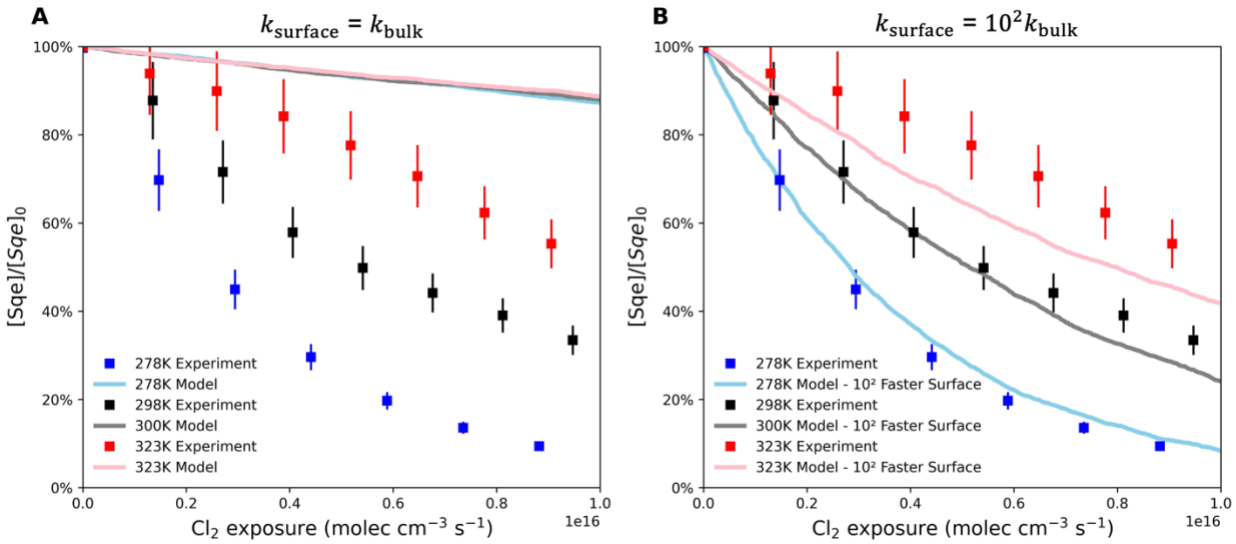

Figure 2.3. Kinetic model predictions for: (A) a surface reaction rate that is equal to bulk rate; (B) a surface rate that is 100 times faster than bulk. Shown in blue marker and line are the 278K measurements and model predictions, room temperature data is shown in black and grey, and 323K is shown in red. Model scenarios reveal that in order for the model to predict faster reaction kinetics with decreasing temperature, the surface rate must be faster.

Figure 2.3 shows the kinetic model predictions compared with experimental kinetic measurements for two model scenarios. Figure 2.3A shows the first scenario, where we assume that the surface and bulk reactions are equal (i.e., $k_{surface} = k_{bulk}$), while the second scenario shown is Figure 2.3B, assumes that the surface reaction rate coefficient is two orders of magnitude faster (*i.e.,* $k_{surface} = 10^2 k_{bulk}$). The first scenario fails to capture the overall magnitude of the reaction kinetics and is temperature invariant since the increase in solvation counteracts the decrease in the bimolecular rate with decreasing temperature. The second scenario with the faster surface rate is in better agreement with the experimental results. It predicts faster reaction kinetics with decreasing temperature, and at early times, where our assumptions hold best, it is within the experimental error. This scenario generates a hypothesis that the reaction at the surface proceeds faster than in the bulk, which motivates further analysis of our simulations to identify possible microscopic mechanisms for an enhanced surface reaction.

The pseudo-first order rate constant is given by the Arrhenius expression, $k = Ae^{-\frac{E_a}{k_B T}}$, which depends upon the pre-exponential factor A and the activation energy E_a. Thus, there are two ways for a surface reaction rate to be faster than the bulk; either through the pre-exponential factor, e.g., due to a higher encounter frequency at the interface, or thermodynamically, with the activation energy for the reaction being lower at the interface due to the emergence of a new reaction mechanism or the modification of the bulk reaction free energies at the interface.[6,10,34–36] The primary activation barrier will be given by the breaking of the Cl_2 bond, which is not expected to be strongly dependent on the environment, considering that there is no abrupt transition between the gas and liquid dielectric constants at the air/squalene interface, so here we will focus on the former, using simulations to quantify the Cl_2 and C=C double bond encounter frequency.

Chlorine and Carbon Double Bond Contact Probability. From umbrella sampling, we compute the average probability of contact between chlorine and a double bond conditioned on the chlorine's z position, using the method of Souaille and Roux.[31] Contact probability (Figure 2.4A) is defined as the average number of timesteps in which the smallest atomic distance between a Cl atom in Cl_2 and a C atom in a squalene double bond is smaller than 3.5Å. This cutoff was selected based upon the Lennard-Jones sigma parameter between Cl and C (i.e., $\sigma_{Cl-C} = 3.52$Å). Figure 2.4B shows the distribution of C=C double bonds along the squalene slab z axis. Terminal double bonds are preferentially present at the interface due to squalene alignment with the surface normal, which is consistent with previous simulations.[37,38] Figure 2.4C shows the probability of Cl_2 and C=C double bond contact for the three types of double bonds in squalene, normalized to the total double bond density and the average contact probability in the bulk.

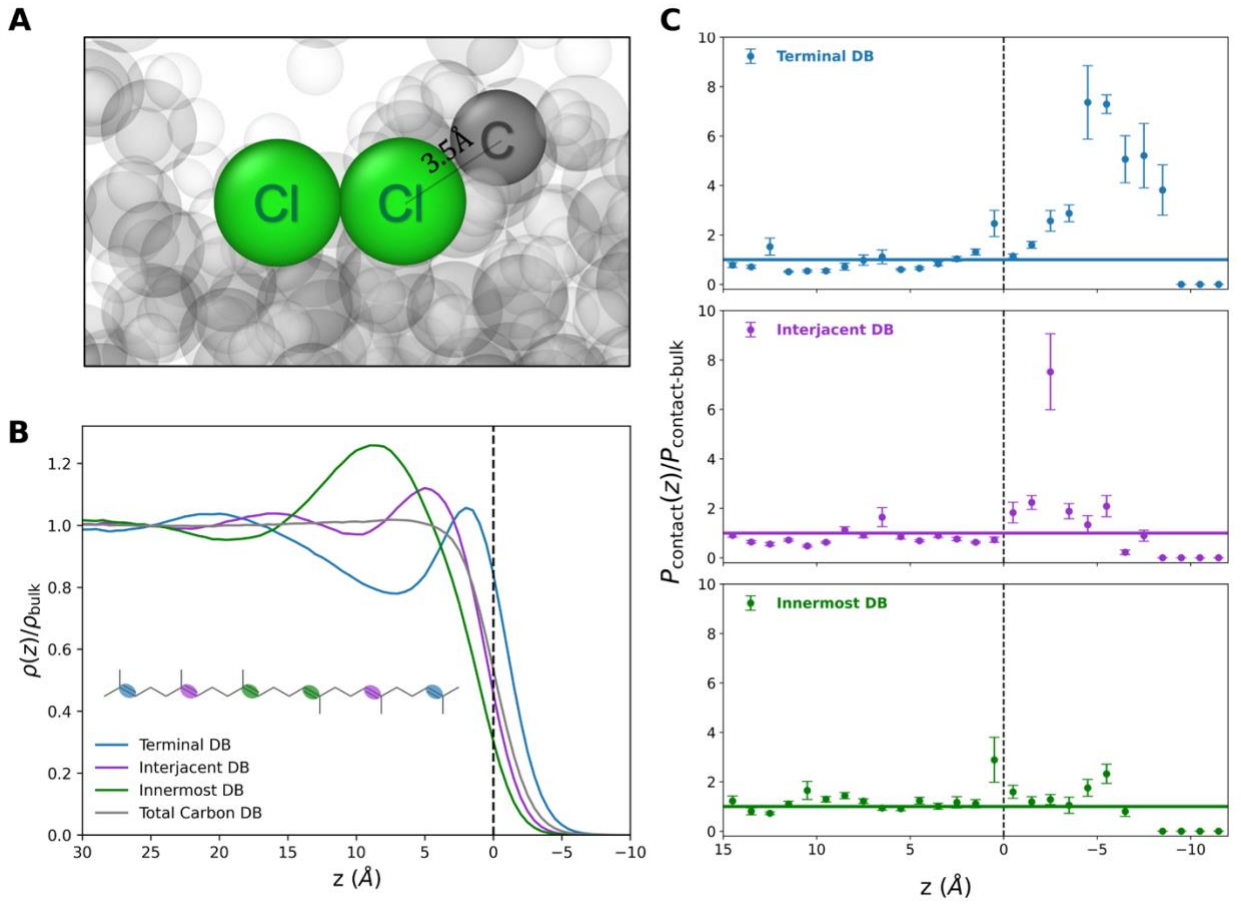

Figure 2.4. (A) Cartoon depicting the definition of contact between a chlorine atom in Cl_2 and a carbon in a double bond of squalene. Contact is computed as the average number of timesteps in which a chlorine atom is at a distance smaller 3.5Å. (B) Distribution of double bonds (DBs) along the slab axis z, terminal DB shown in blue preferentially stick out towards the gas phase. The Gibbs dividing surface is shown with a dashed line. (Inset) Squalene chemical structure with color coding of DB types. (C) Probability of contact along the slab axis z for all double bond types normalized to the total DB density and bulk averaged contact probability. A horizontal line at 1 represents the bulk average. Contact on the gas side of the interface is enhanced compared to bulk contact.

Figure 2.4C shows that the terminal double bonds that extend out of the interface and into the gas phase can interact with Cl_2 at a probability that is almost an order of magnitude larger than it is in the bulk. A smaller interaction enhancement is observed for the other C=C types, following their density profile along the z axis. We find that the increased contact probability of squalene with a gas phase chlorine molecule at the interface cannot be explained only by the increased concentration of terminal double bonds since our computed contact probability is already normalized to the double bond density. This suggests that there must be an additional thermodynamic driving force attracting chlorine molecules and double bonds at the interface. To calculate the encounter probability between chlorine and C=C in the interfacial region where the density of double bonds is small, we evaluate the two-dimensional free energy for chlorine's position relative to the interface, z, and its distance from a C=C terminal double bond center of mass, R,

$$F(z,R) = -k_B T \ln\langle \delta(z - z_0)\delta(R - R_0)\rangle + F_0, \tag{2.4}$$

where each data point is normalized to the spherical density profile of the terminal double bond, and F_0 is the reference free energy set to zero at long interaction distances ($R = 10$Å).

The resultant free energy surface is shown in Figure 2.5 and provides further supporting evidence for a faster surface reaction.

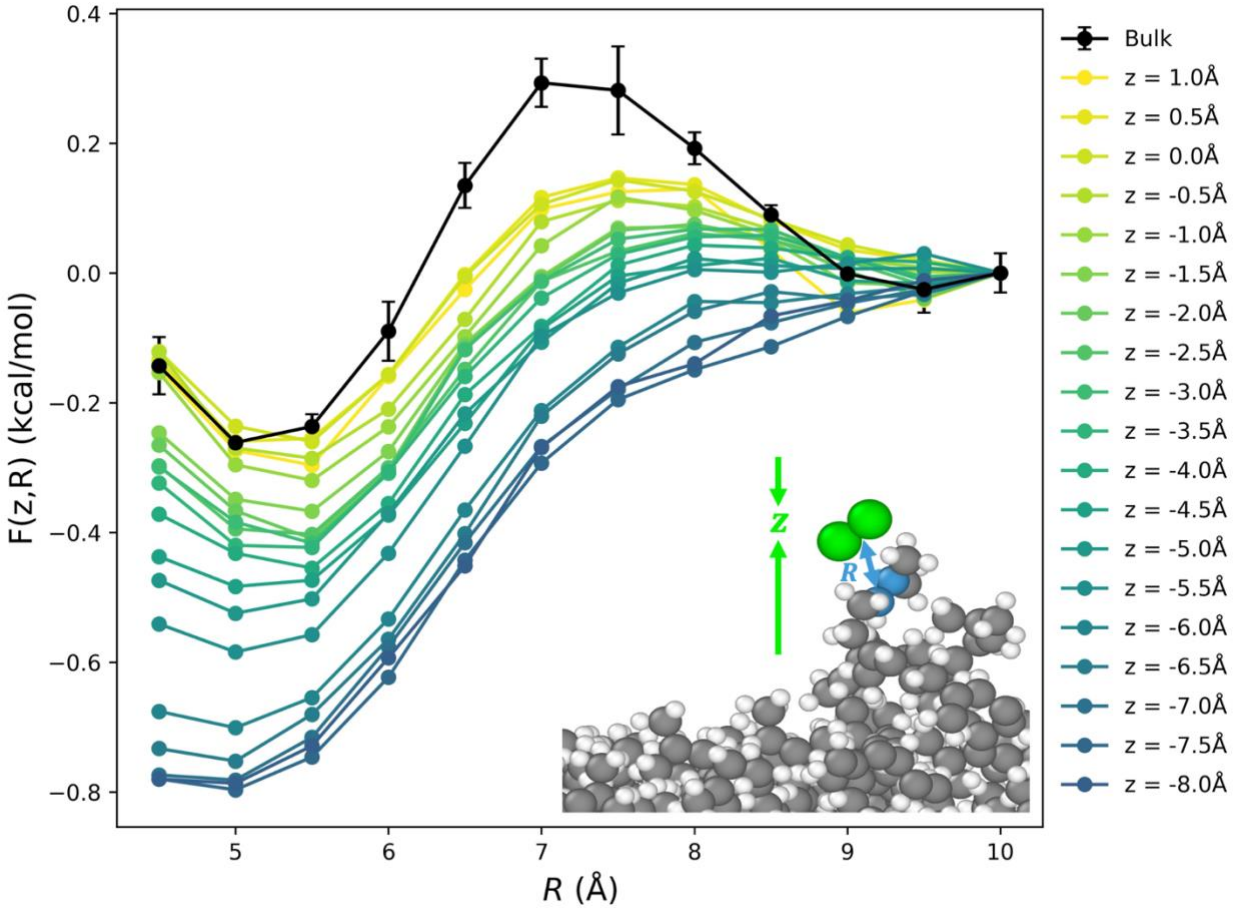

Figure 2.5. 2D-PMF for chlorine's interaction with a terminal double bond along the slab z axis, and across R, the distance between the chlorine center of mass and the terminal double bond. Black traces show the bulk interaction and colors from yellow to blue show how the interaction energy changes from just below the Gibbs dividing surface ($z = 0$Å), with positive z values in yellow and into the gas phase with increasing negative values in blue. (*Inset*) Snapshot from biased simulation illustrating the 2D-PMF coordinates, chlorine is show in green and the terminal double bond is tagged in blue.

The PMF in the bulk region of the liquid exhibits two minima, first around $R = 5$Å and again at 9.5Å, separated by a barrier. The first minimum originates from the solvation shell around Cl_2, where chlorine interacts favorably with carbon atoms. There is a ~ 0.5kcal/mol energetic barrier between $R = 5$Å and 9.5Å corresponding to the rearrangement of the solvation structure of squalene as the tagged double bond is removed from the first solvation shell of Cl_2. At the Gibbs dividing surface, these discrete solvation details are attenuated. The minimum at $R = 5$Å is preserved since it originates from the direct interaction energy between chlorine and C=C. In contrast, moving chlorine away at the interface yields a lower energetic barrier since squalene atoms can be displaced into the low-density gas phase, reducing the free energy cost of modifying local solvation structure, which is dominated by strong C-C repulsive interactions in the high-density liquid phase. As we proceed into the gas phase to examine free energy curves corresponding to larger negative z values and away from the Gibbs surface, the attractive well R =

5Å deepens, and the overall energy contribution from the interaction of chlorine with the terminal double bond becomes larger. For example, at $z = -8$Å this interaction is ~0.6 kcal/mol or ~1 kT larger than in the bulk. This can be explained considering squalene's relatively weak dispersion interactions with itself, allowing for surface molecules to stick out like pins into the gas phase without paying a large enthalpic cost. At this position, where the terminal double bonds are completely exposed, the volume around the double bond is vacant, allowing chlorine to interact in more possible arrangements and more closely due to the lack of steric hindrance.

The increased interaction energy at the interface means that the encounter probability between chlorine and a terminal double bond is larger at the interface. If we define encounter as the minimum at R = 5Å, as we move further into the gas phase the probability of encounter increases, at $z = -8$Å it is about three times larger than in the bulk, and when normalized to the total C=C double bond density chlorine; it is about eight times more likely to encounter a double bond at the interface than in the bulk, suggesting that a reaction in this surface region could be almost an order of magnitude faster than in bulk. This mechanism for interfacial acceleration can be visualized by analogy to spearfishing, where squalene tails are extending out into the gas phase to interact with chlorine molecules. It is distinct from proposed mechanisms for reaction rate acceleration at aqueous interfaces, which are largely dielectric in origin. Rather, here, it is the increased propensity for density fluctuations at the interface, which is larger for long hydrocarbon chains compared to water,[39,40] resulting in an exposure of reactive double bonds to facilitate a reaction.

Position-Dependent Diffusion. The energetic contribution at the interface is only one facet of the encounter frequency. When evaluating the potential differences between the pre-exponential factor at the interface and in the bulk, we should also consider how chlorine dynamics changes when crossing these regions. Following a method developed by Polley *et al.,* [41] we compute the position dependent friction and therefore diffusivity, of chlorine's motion perpendicular to the interface, *i.e.,* along the z- axis. The dynamics are treated in a continuum picture as a coarse-grained single particle following the Fokker-Planck equation of motion, where the time evolution of a particle probability density along the slab axis z is,

$$\frac{\partial p(z,v,t)}{\partial t} = -v\frac{\partial p}{\partial z} + \frac{\partial}{\partial v}\left[\frac{\partial_z F(z)}{m} + \gamma(z)v\right]p + \frac{k_B T\gamma(z)}{m}\frac{\partial^2 p}{\partial v^2}, \tag{2.5}$$

where $F(z)$ is the potential of mean force, $\gamma(z)$ is the position-dependent friction experienced by the particle of mass m, and v is velocity. The friction profile is described by a smoothly varying hyperbolic tangent function,

$$\gamma(z) = (\gamma_{\mathrm{l}} - \gamma_{\mathrm{g}})\left(\tanh\frac{(w(s-z))}{2} + \frac{1}{2}\right)^n + \gamma_{\mathrm{g}}, \tag{2.6}$$

where γ_{l} is the friction of the bulk liquid, γ_{g} is the friction in the gas phase, and s, w, and n are the fitting parameters controlling the transition region between the gas and bulk friction asymptotes. The friction in the bulk and gas regions are determined from the diffusion coefficients using the Einstein relation, $\gamma_{\mathrm{l/g}} = \frac{k_{\mathrm{B}}T}{mD_{\mathrm{l/g}}}$, where $\mathrm{D_l}$ is obtained directly from trajectory analysis of mean-squared displacement and $\mathrm{D_g}$ is from Ref. [42]. To find the optimal fit parameters for the functional form of the friction $\gamma(z)$, we propagated the Fokker-Planck equation while varying the fit parameters using a gradient-free optimizer until the probability distribution compared favorably

with those obtained explicitly from shooting trajectories of chlorine towards the squalene slab. Implementation details, the comparison between the converged optimized friction $\gamma(z)$ and trajectories, and the resulting friction profile are available in the Supporting Information. The friction profile (Figure 2.S6) indicates that chlorine experiences friction well outside the squalene density range due to fluctuating long-range dispersion forces between chlorine and squalene molecules. The diffusion of chlorine which is inversely proportional to the friction (*i.e.,* the Einstein relation) is about an order magnitude faster at the Gibbs dividing surface and up to four orders of magnitude faster in the gas phase relative to the bulk. Thus, this substantial change in Cl_2 dynamics will influence the interfacial reaction rates relative to the bulk.

Interfacial Pre-exponential Factor. If we consider the interface in a coarse grain fashion, where probabilities of encounter and dynamics are averaged over the interfacial region, we can make an estimate for the interfacial enhancement of reactivity due to a larger pre-exponential factor. As in the kinetic model framework presented above, we define the interfacial region by the decay in the double bond density, over the range of $-8 \leq z \leq 5$Å. We might naively assume that a slow reaction such as this would have a large energetic barrier, and thus only equilibrium properties embodied in the encounter probability should matter. However, the activation energy for C=C double bond chlorination in non-polar solvents is quite small ($1.8\ \mathrm{kcal/mol}$ for oleic acid[18]), suggesting that how rapidly chlorine samples that equilibrium probability through diffusion will strongly influence the frequency of encounter in the pre-exponential factor. Hence, we can calculate a relative pre-exponential factor comparing surface and bulk by assuming that it is directly proportional to the encounter probability between Cl_2 and a C=C double bond weighted by double-bond density, and the Cl_2 diffusion coefficient, all of which are a function of z,

$$\frac{A_{\text{interface}}}{A_{\text{bulk}}} = \frac{\int^{z_{\text{interface}}} P_{Cl_2-C_{\text{DB}}}(z)\rho_{C_{\text{DB}}}(z)D_{Cl_2}(z)dz}{P_{Cl_2-C_{\text{DB}}-\text{bulk}}\rho_{C_{DB}-\text{bulk}}D_{Cl_2-\text{bulk}}}, \tag{2.7}$$

where $P_{Cl_2-C_{\text{DB}}}$ is the encounter probability between chlorine and a C=C double bond in squalene, $\rho_{C_{\text{DB}}}$ is the double bond density and D_{Cl_2} is chlorine's diffusion constant. The contact probability $P_{Cl_2-C_{\text{DB}}}$ can be computed from the 2D-PMF in Figure 2.5, converting free energy differences between z-dependent interfacial values and the bulk to relative probabilities, where encounter is defined as the interaction minima at $\mathrm{R} = 5$Å. This encounter probability is conditioned on the presence of a C=C double bond at a given z value and must then be weighted by the C=C double bond density to reflect the relative contribution to reactivity of each z slice. Position dependent diffusion is calculated from the friction function using the Einstein relation and values for the position dependent variables in Eq. (2.7) are listed in Table 2.S5. If we assume that reactivity is uniform along z, we can compute the interfacial encounter frequency to be 12 times larger than the bulk, which would be a lower limit estimate. The diffusion constant changes by three orders of magnitude across the interfacial region, meaning that reactivity is likely to be dominated by the faster chlorine molecules arriving from the gas phase, rather than the slower molecules coming from the liquid phase. If we assume that reactivity is determined by the gas phase Cl_2 flux, we can calculate an upper limit estimate by asserting that the diffusion constant on the gas side of the interface (i.e. beyond the Gibbs dividing surface, with negative z values) is equal to the diffusion constant at the gas phase edge ($D_{Cl_2-8\text{Å}<z\leq 0\ (Gibbs)} = D_{Cl_2-z=-8\text{Å}}$). When integrated across the interfacial region the upper limit estimate for the pre-exponential factor is about three orders of

magnitude larger than bulk. While an exact calculation requires more sophisticated simulations and models, that may be intractable for the large number of atoms required to simulate an organic interface, the changes in the pre-exponential factor observed here nicely bracket the estimate of $k_{\text{surface}} = 10^2 \times k_{\text{bulk}}$ from the kinetic model, which is needed to explain the temperature trend observed in the aerosol experiments (Figure 2.3B). Further constraints to refine the kinetic model can also be achieved through explicit measurements of the bulk rate for squalene chlorination.

There is some experimental evidence that the bulk free radical oxidation of squalene occurs primarily on the terminal double bond.[43] It was hypothesized that this is due to increased flexibility of the squalene tails. If electrophilic addition exhibits a similar affinity for the terminal double bonds, then the interfacial rate could be even larger since both their density is higher on the surface and a reactive encounter is more likely and frequent. This hypothesis could be tested, for example, in experiments that can distinguish conformational isomers. Further experimental supporting evidence that electrophilic addition to alkenes could be sensitive to interfacial reactivity was reported by Kropp *et al.*,[44] where they found that reactions of HCl and HBr with a number of alkenes, which normally react very slowly in bulk, proceeded more quickly and in greater yields when silica gel surfaces were added to solution.

The interfacial enhancement reported in this study is a direct consequence of molecular details unique to squalene; driven by its orientation on the surface and the relatively weak intermolecular forces acting between solvent molecules. This result was not anticipated, and it would be interesting to explore if the interfacial structure of other hydrocarbons and oil species behaves similarly. The overwhelming majority of accounts on interfacial reaction acceleration is focused on aqueous interfaces, with little attention given to air/oil interfaces. We hope that this study can generate further interest in reactivity at organic interfaces.

2.4. Conclusion

We have used molecular dynamics simulations to construct the potential of mean force (PMF) for chlorine solvation at the air/squalene interface, in order to compute thermodynamic quantities such as Henry's law coefficients, bulk diffusivities and mass accommodation coefficients. The information extracted from simulations is used to constrain a two-compartment kinetic model representing the bulk and surface of an aerosol particle. The model suggested that a faster interfacial rate is required to explain the temperature dependent results observed in experiments. This enhanced interfacial reaction is not physically intuitive since the reaction is slow and we would expect its reacto-diffusive length to be large. We proceeded to identify a molecular origin for this acceleration in our simulations and found that chlorine was more likely to have contact with a terminal C=C double bond at the interface. The 2D-PMF for the interaction energy between Cl_2 and a terminal double bond confirmed that the probability of encounter is three times larger at the gas side of the interface, and that when normalized to the total C=C double bonds in the system it is about eight times larger than bulk, suggesting a "tail spearfishing" mechanism where squalene tails extend out to the gas phase to interact with chlorine molecules.

Furthermore, not only is the contact more favorable at the interface, but it is also sampled more frequently than in the bulk liquid since chlorine's diffusivity is faster at the surface, with its diffusion constant changing over three orders of magnitude across the interfacial region. Overall, the change to the Arrhenius pre-exponential factor, or the reaction encounter frequency, was calculated to be at least 12, and up to three orders of magnitude faster at the interface, making it

the primary explanation for interfacial acceleration of chlorine addition to C=C double bonds in squalene.

2.5. Supporting Information

2.5. Section S1: Resistor Model Predictions

From considerations of the reacto-diffusive length only, we would expect squalene chlorination in a sub-micron aerosol to occur mostly in the bulk since the rate constant for Cl_2 addition to carbon double bonds is, in non-polar solvents, relatively slow ($\sim 10^{-19} - 10^{-18} \mathrm{cm^3 molec^{-1} s^{-1}}$).[18] We might expect some slow reactions to exhibit enhanced surface reactivity due to the enrichment of reagents at the interface (e.g. reactions with surfactants). However, this would not be expected for this system since chlorine is known to be quite soluble in organic solvents.[30]

Estimates of the uptake coefficient, γ, can be made using the resistor model framework.[20] For slow reactions an analytical solution for the uptake coefficient has the form,

$$\gamma = \frac{4aHRT}{3\bar{c}} k_{\mathrm{rxn}}, \tag{2.S1}$$

where a is the particle radius, H is the henry's law constant, R is the gas constant, T is the temperature, $\bar{c}$ is the mean gas velocity of Cl_2. Temperature dependent quantities used to calculate the uptake coefficient using Eq. (2.S1) are shown in Table 2.S1.

Table 2.S1. Physical quantities used to compute resistor model uptake predictions for slow reaction

Temperature	**278K**	**300K**	**323K**	**Notes**
γ	4.93 x 10^{-6}	5.07 x 10^{-6}	4.85 x 10^{-6}	Calculated from Eq.S1
k_b $(cm^3 molec^{-1} s^{-1})$	1.6 x 10^{-18}	2.0 x 10^{-18}	2.5 x 10^{-18}	Estimated from chlorine addition to double bond of oleic acid in CCl_4 [18] multiplied X 6 to account for 6 double bonds in squalene, activation energy of 1.8kcal/mol calculated from temperature dependence of the oleic acid rate.
$k_{rxn} = k_b[sqe](s^{-1})$	2016	2520	3150	$[sqe] = 1.26 \times 10^{21} molec/cm^3$ from squalene density $0.858 gr/cm^3$
$\boldsymbol{H_{cc}^{g \to b}} = HRT$	7.05	6.02	4.78	These dimensionless Henry's law constants are calculated from the temperature dependent PMF Figure 2.2B
$\bar{c}(m/s)$	288.1	299.3	310.5	Calculated for chlorine from $\sqrt{\frac{8RT}{\pi M}}$
$r(nm)$	75	75	75	Mean particle radius from experiment [17]

Bolded quantities are calculated from our MD simulations

2.5. Section S2: Molecular Dynamics Simulation Details and Force Field Selection

In preparation for this study, we examined 4 different models of squalene:

1. ATb PJMU [45]– squalene initial configuration containing two cis bonds provided by ATb database at a semi-empirical level of theory using the GROMOS 54A7 force field(FF).
2. ATb KFEY [46]- initial configuration based on the xyz coordinates provided in Ref. [47] for trans squalene, optimized by ATb at a semi-empirical level using GROMOS 54A7 FF.
3. OPLS-AA [48] – general liquid force field used with the same initial configuration for trans squalene, atom types were defined to match definition in force field atom types.
4. Long Chain OPLS-AA [49]– OPLS force field with additional parameters and atom types for long hydrocarbon chains.

The liquid density for squalene models, described above, are tabulated in Table 2.S2.

Table 2.S2. Liquid densities for squalene force fields

Model	**Density g/cm^3**
ATb PJMU + GROMOS 54A7	0.873
ATb KFEY + GROMOS 54A7	0.860
OPLS-AA	0.839
Long Chain OPLS-AA	0.831

The densities for all models are in good agreement with the experimental density of squalene (0.858 g/cm^3 at 20C [50]). The OPLS models show a slightly lower density than the experimental value. We also examined the C-C bond length distribution to further evaluate the models. A higher-level theory (B3LYP/6-31G) DFT calculation was performed in ATb for a terpene structure with an additional carbon, terpene is the building block unit for squalene molecules.

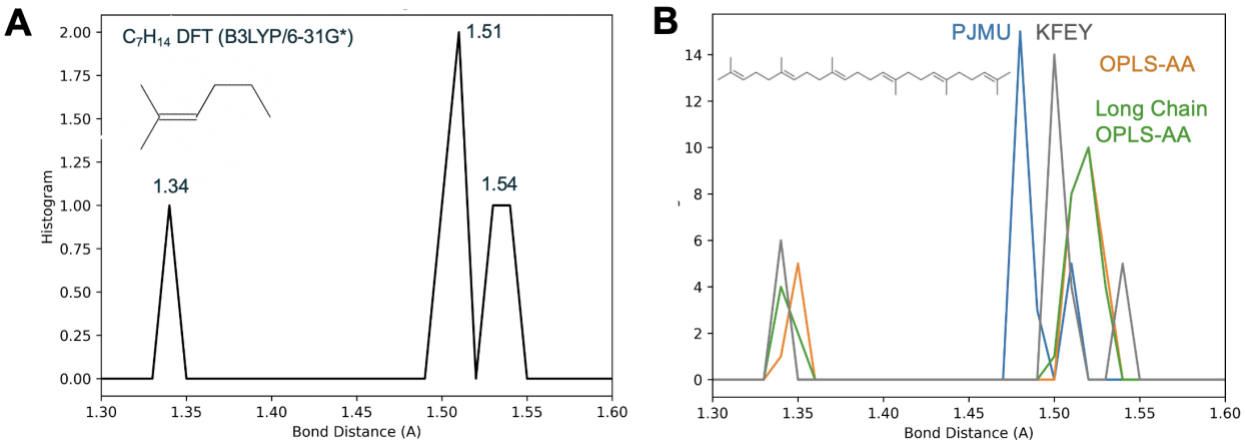

Figure 2.S1. Histograms of C-C bond lengths for (A) terpene fragment DFT calculation at B3LYP level (B) different squalene models. KFEY residue is closest to fragment higher theory calculations.

Higher level calculation shown in Fig. 2.S1A identifies three C-C bond lengths: the shortest double bond C=C, and two single bonds with a shorter single bond closer to the double bond (i.e. C=**C-C**). Figure S1B shows that both ATb models manage to capture this quality, while the OPLS force fields only use a single C-C bond length. Since a difference in C-C bond length could be important for capturing the system correctly, we decided to use the ATb KFEY model, which matched fragment calculations more accurately and was closer to the experimental density. Force field parameters for Cl_2 are taken from ATb [46] to use the same general force field for all molecules in the system.

2.5. Section S3: Chlorine Solvation PMF Umbrella Sampling

The combination of spring constants used in umbrella sampling bias windows is shown in Table 2.S3.

Table 2.S3. Umbrella sampling bias windows details

$k\left(\frac{kcal}{mol\text{Å}^2}\right)$	Constrained Position in box $z_0(\text{Å})$	Constrained Position shifted to zero at Gibbs dividing surface (matching coordinates presented in the paper) $z_0(\text{Å})$	Simulation length per window
1	--47.5,-46.5,…,46.5,47.5 -35,-34,…,34,35	-16.5,-15.5,…,77.5,78.5 -4,-3,…,65,66	10ns
3	-47.5,-46.5,…,46.5,47.5 -35,-34,…,34,35	-16.5,-15.5,…,77.5,78.5 -4,-3,…,65,66	20ns
5	-40,-39.5,..,39.5,40	-9,-8.5,..,70.5,71	20ns
8	-30,-29.5,…,29.5,30	1,1.5,..,60.5,61	20ns

2.5. Section S4: Kinetic Model Details

Kinetic model details implemented in Kinetiscope, [33] an open source stochastic reaction-diffusion simulator that propagates a transformation through a random walk of probability weighted diffusion and reaction steps. Kinetiscope has been extensively used to elucidate reactions and chemical transformations in aerosols and microcompartments. [51–59] The simulation scheme (Fig. 2.S2) closely follows the framework developed by Willis and Wilson, [32] which describes an aerosol particle as comprised of two reaction compartments: surface and bulk. Scaling of the compartments is such that the height of the bulk compartment is a/3 (where a is the aerosol or particle radius) to preserve the correct surface to volume scaling in a sphere. The surface compartment thickness in previous implementations of this framework was assumed to be $\delta \approx$ 1 nm, which is consistent with the dimensions of the solvation free energy profiles for aqueous interfaces obtained in previous simulations. [60] Interfacial thicknesses as a function of temperature for squalene are defined directly using the temperature dependent density and solvation free energy profiles. To calculate volumetric concentration, the length and width of both compartments is set to 1 nm. These dimensions have been shown to not influence simulation results [32]. The compartments are assumed to be internally well-mixed, and molecules move between compartments by Fickian diffusion.

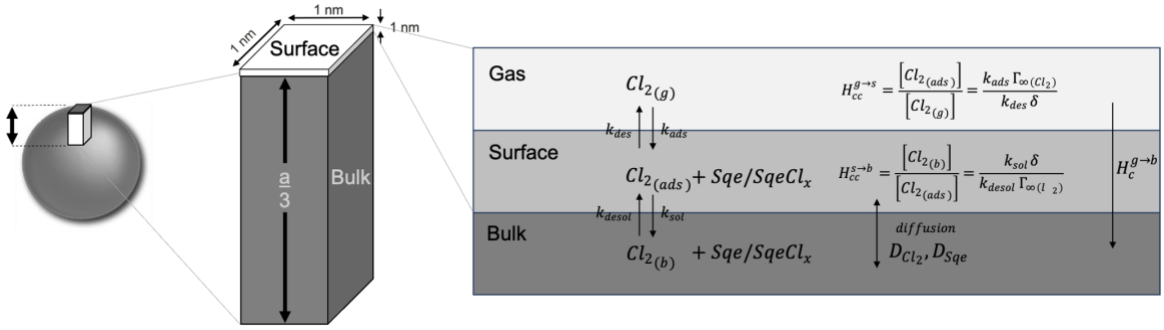

Figure 2.S2. Framework for kinetic modeling. Simulation preserves surface area to volume ratio of a sphere with surface compartment that is 1nm thick and bulk compartment with height of a/3. Three kinetic regions: gas, surface ,and bulk, maintain concentrations through coupled equilibrium determined by Henry's law coefficients calculated from MD. Surface and bulk species can react with squalene or diffuse between compartments. Maximum surface concentration $\Gamma_{\infty(Cl_2)}$ (from chlorine molecular size) and interfacial thickness δ determines the concentration of surface sites.

The scheme features three kinetic regions: gas, surface, and bulk. Chlorine concentrations in each region are governed by a dimensionless Henry's law constant (H_{cc}) computed from the solvation free energy difference obtained by the Cl_2 PMF described above,

$$H_{cc}^{x\to y} = e^{-\frac{\Delta G_{x\to y}}{RT}}. \tag{2.S2}$$

$\Delta G_{x\to y}$ is the free energy difference of Cl_2 between different regions (e.g. x = gas, y = bulk). The gas to surface Henry's law constant is,

$$H_{cc}^{g\to s} = \frac{[Cl_{2(ads)}]}{[Cl_{2(g)}]} = \frac{k_{ads}\Gamma_{\infty(Cl_2)}}{k_{des}\delta}, \tag{2.S3}$$

where k_{ads} and k_{des} are rate coefficients that describe the adsorption and desorption of Cl_2 to the interface. $\Gamma_{\infty(Cl_2)}$ is the maximum surface concentration, and δ is the interfacial thickness. Surface sites are represented as volumetric concentrations ($\frac{\Gamma_{\infty(Cl_2)}}{\delta}$). $\Gamma_{\infty(Cl_2)}$ is computed from the molecular area of Cl_2 (19.1Å – taken from force field parameters for Cl_2). k_{ads} is set to the collision frequency of chlorine gas, which assumes a sticking probability of 1,

$$k_{ads} = \frac{\bar{c}A}{4}, \tag{2.S4}$$

where $\bar{c}$ is the mean speed of chlorine gas (299 m/s at 300K) and A is the area of the surface compartment. k_{des} is computed from Eq. (2.S3) using k_{ads} and $H_{cc}^{g\to s}$ obtained in the simulations. Once chlorine is thermalized at the surface it can react with a squalene molecule, desorb back into the gas phase, or become solvated into the bulk liquid. Surface to bulk partitioning is described by a second Henry's law constant,

$$H_{cc}^{s\to b} = \frac{[Cl_{2(b)}]}{[Cl_{2(ads)}]} = \frac{k_{sol}\delta}{k_{desol}\Gamma_{\infty(Cl_2)}}, \tag{2.S5}$$

where the solvation rate (k_{sol}) is computed from k_{des} and the mass accommodation coefficient obtained directly from simulations,

$$\alpha = \frac{k_{sol}}{k_{sol}+k_{des}} \to k_{sol} = \frac{\alpha k_{des}}{1-\alpha} \tag{2.S6}$$

From k_{sol} and $H_{cc}^{s\to b}$, k_{desol} is determined using Eq. (2.S5). All model parameters other than the reaction rate constant are directly constrained by molecular models. To our knowledge the rate coefficient for squalene chlorination has not been measured, instead we use the closest reaction system we found in the literature, the rate constant for Cl_2 addition to oleic acid in carbon tetrachloride [18], multiplied by six to account for the six double bonds in squalene to one in oleic acid. The rate coefficients for successive Cl_2 additions to the 6 C=C of squalene are assumed to be the same as that for pure squalene. By changing the surface rate constant, we can use the model as a predictive tool to assess the surface rate enhancement required to explain the experimental result. A complete list of model parameters is given in the Table 2.S4.

Table 2.S4. Elementary reaction steps, rate and diffusion coefficients used in the Kinetiscope simulations. Quantities derived directly from MD simulations are shown in **Bold**. Reaction steps that occur at the surface compartment are labeled with S, diffusion steps between the surface and bulk compartment are labeled with D, and reaction steps in the bulk are labeled with B.

#	Reaction	Rate Coefficient			Notes
		278K	300K	323K	
S1	$\mathrm{site}_{Cl_2} \underset{k_{des}}{\overset{k_{ads}}{\rightleftarrows}} Cl_{2(ads)}$	$k_{ads} = 1.77 \times 10^4 s^{-1}$ $k_{des} = 1.74 \times 10^{10} s^{-1}$ $\boldsymbol{H_{cc}^{g\to s} = 21.68}$ $\boldsymbol{H_{cc}^{s\to b} = 0.3254}$ $\boldsymbol{H_{cc}^{g\to b} = 7.05}$ $\boldsymbol{\delta = 1.46nm}$ ***estimated from expansion of interfacial region in PMF compared to 300K**	$k_{ads} = 1.84 \times 10^4 s^{-1}$ $k_{des} = 2.95 \times 10^{10} s^{-1}$ $\boldsymbol{H_{cc}^{g\to s} = 13.24}$ $\boldsymbol{H_{cc}^{s\to b} = 0.4545}$ $\boldsymbol{H_{cc}^{g\to b} = 6.02}$ $\boldsymbol{\delta = 1.3nm}$ ***calculated from the decay length of the double bond density.**	$k_{ads} = 1.91 \times 10^4 s^{-1}$ $k_{des} = 4.52 \times 10^{10} s^{-1}$ $\boldsymbol{H_{cc}^{g\to s} = 8.97}$ $\boldsymbol{H_{cc}^{s\to b} = 0.5331}$ $\boldsymbol{H_{cc}^{g\to b} = 4.78}$ $\boldsymbol{\delta = 1.14nm}$ ***estimated from compression of the interfacial region in PMF compared to 300K**	$k_{ads} = \frac{\bar{c}A}{4}$, where mean speed of Cl_2 is calculated from $\sqrt{\frac{8RT}{\pi M}}$. k_{ads}implemented here in one step following a pseudo first-order rate with $[Cl_2] = 10ppm$ matching the experimental conditions, no sensitivity is observed in the model for concentrations within an order of magnitude difference (1-100ppm) $k_{des} = \frac{k_{ads}\Gamma_{\infty(Cl_2)}}{H_{cc}^{g\to s}\delta} = \frac{k_{ads}[\mathrm{site}_{Cl_2}]}{H_{cc}^{g\to s}}$ $\boldsymbol{molecular\ area = 19.13}$Å $[\mathrm{site}_{Cl_2}] = \frac{V_{sur}}{molecular\ area}$

S2	$Cl_{2(ads)} \underset{k_{desol}}{\overset{k_{sol}}{\rightleftarrows}} Cl_{2(b)} + \text{site}_{Cl_2}$	$k_{sol} = 1.15 \times 10^{10} s^{-1}$ $k_{desol} = 6.78 \times 10^{-12} cm^3 molec^{-1} s^{-1}$ $\boldsymbol{\alpha = 0.399}^*$ ***estimated from bulk solvation energy gap to increase from room temperature according to surface to bulk solvation energy.**	$k_{sol} = 1.61 \times 10^{10} s^{-1}$ $k_{desol} = 6.78 \times 10^{-12} cm^3 molec^{-1} s^{-1}$ $\boldsymbol{\alpha = 0.355}^*$ ***calculated from branching of trajectories starting at the interface**	$k_{sol} = 1.60 \times 10^{10} s^{-1}$ $k_{desol} = 5.74 \times 10^{-12} cm^3 molec^{-1} s^{-1}$ $\boldsymbol{\alpha = 0.261}^*$ *** calculated from branching of trajectories starting at the interface**	$\alpha = \frac{k_{sol}}{k_{sol} + k_{des}}$ $k_{sol} = \frac{\alpha k_{des}}{1 - \alpha}$ $k_{desol} = \frac{k_{sol}\delta}{H_{cc}^{S \to b} \Gamma_{\infty(Cl_2)}} = \frac{k_{sol}}{H_{cc}^{S \to b} [\text{site}_{Cl_2}]}$
S3	$Cl_{2(ads)} + Sqe \rightarrow SqeCl_2 + \text{site}_{Cl_2}$	Surface reaction rate is set to be equal to bulk rate (reaction B1) or set uniformly (independent of temperature) to be larger by X amount from B1 rate at room temperature.			$[sqe] = 1.26 \times 10^{21} molec/cm^3$ from squalene density 0.858 g/cm^3
S4	$Cl_{2(ads)} + SqeCl_2 \rightarrow SqeCl_4 + \text{site}_{Cl_2}$	Zeng et al.[17] found that this reaction appears to be following a sequential mechanism where chlorine adds across double bonds for already chlorinated products. We assume these reactions proceed with the same rate as the initial oxidation rate S3.			
S5	$Cl_{2(ads)} + SqeCl_4 \rightarrow SqeCl_6 + \text{site}_{Cl_2}$	"			
S6	$Cl_{2(ads)} + SqeCl_6 \rightarrow SqeCl_8 + \text{site}_{Cl_2}$	"			
S7	$Cl_{2(ads)} + SqeCl_8 \rightarrow SqeCl_{10} + \text{site}_{Cl_2}$	"			
S8	$Cl_{2(ads)} + SqeCl_{10} \rightarrow SqeCl_{12} + \text{site}_{Cl_2}$	"			
D1	$Cl_{2(b)}$	$\boldsymbol{D_{Cl_2} = 2.33 \times 10^{-6} cm^2 s^{-1}}^*$ ***calculated from linear regression of higher temperature values across this small range**	$\boldsymbol{D_{Cl_2} = 3.49 \times 10^{-6} cm^2 s^{-1}}^*$ ***calculated directly from mean squared displacement analysis in the bulk region**	$\boldsymbol{D_{Cl_2} = 4.72 \times 10^{-6} cm^2 s^{-1}}^*$ ***calculated directly from mean squared displacement analysis in the bulk region**	Simulation is insensitive to the exact diffusion coefficient as long as it is larger than the compartment size, since we are simulating nm scale droplets no sensitivity is observed
D2	$Sqe/SqeCl_x$	Assumed same as 300K	$\boldsymbol{D_{Sqe/SqeCl_x} = 1 \times 10^{-6} cm^2 s^{-1}}^*$ ***calculated directly from mean squared displacement analysis in the bulk region**	Assumed same as 300K	"
B1	$Cl_{2(b)} + Sqe \rightarrow SqeCl_2$	$k = 1.6 \times 10^{-18} cm^3 molec^{-1} s^{-1}$	$k = 2.0 \times 10^{-18} cm^3 molec^{-1} s^{-1}$	$k = 2.5 \times 10^{-18} cm^3 molec^{-1} s^{-1}$	Estimated from chlorine addition to double bond of oleic acid in CCl_4 [18] multiplied X 6 to account for 6 double bonds in squalene, activation energy of 1.8kcal/mol calculated from temperature dependence of the oleic acid rate.
B2	$Cl_{2(b)} + SqeCl_2 \rightarrow SqeCl_4$	"	"	"	Subsequent reactions assumed to proceed with the same rate as B1
B3	$Cl_{2(b)} + SqeCl_4 \rightarrow SqeCl_6$	"	"	"	"
B4	$Cl_{2(b)} + SqeCl_6 \rightarrow SqeCl_8$	"	"	"	"

B5	$Cl_{2(b)} + SqeCl_8 \rightarrow SqeCl_{10}$	“	“	“	“
B6	$Cl_{2(b)} + SqeCl_{10} \rightarrow SqeCl_{12}$	“	“	“	“

2.5. Section S5: Comparison of WHAM Averaged Decomposition to Directly Simulated Higher Temperature PMF

The WHAM averaged enthalpy profile is shown in Fig. 2.S3A. Explicit umbrella sampling simulations were performed at T=323K using the same bias windows listed in Table 2.S3 and compared to the WHAM averaged decomposition estimate. Fig. 2.S3B shows the comparison between the WHAM calculated average estimate and the explicit simulation for T=323K.

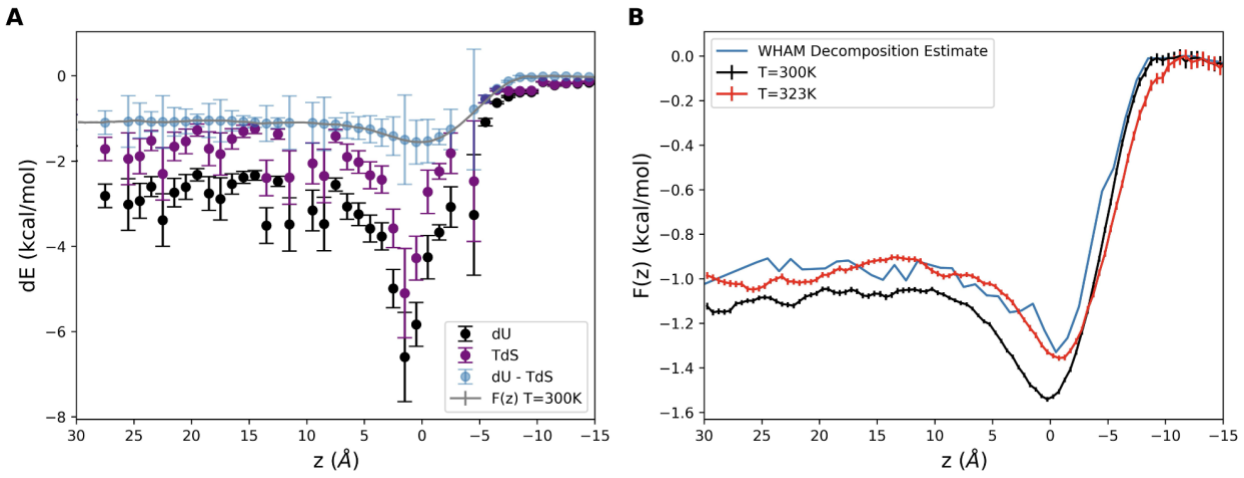

Figure 2.S3. (A) Enthalpy profile from WHAM estimate (black marker) and decomposition of entropy to match T=300 PMF (purple marker). (B) Explicitly calculated PMF from umbrella sampling at 323K (red) and 300K (black) with the WHAM decomposition estimate for 323K (blue line).

This procedure provides confidence that the decomposition accurately captures the change in the PMF with temperature and thus correctly calculates the changes Henry's law constants calculated from the energy differences. Both the shift in the slab dimensions due to less compact packing and overall magnitude of energy differences are preserved.

2.5. Section S6: Position Dependent Friction and Fokker Planck Propagation

To characterize the diffusive behavior of Cl_2 near the interface, we followed the procedure by Polley et at. detailed in Ref [41]. First, we evolved trajectories by placing chlorine in the gas phase; parameterized as a Gaussian centered at $z = -14$Å (45Å in box coordinates) with a thermally sampled velocity towards the squalene slab. Chlorine's center of mass position and velocity were recorded for 30ps in the z direction, to constrain the friction profile of a Cl_2 molecule in the interfacial region. The velocity and position are histogrammed to construct a time dependent position-velocity probability distribution of Cl_2 approaching the interfacial minimum of the PMF. The position probability distribution is shown in Fig. 2.S4.

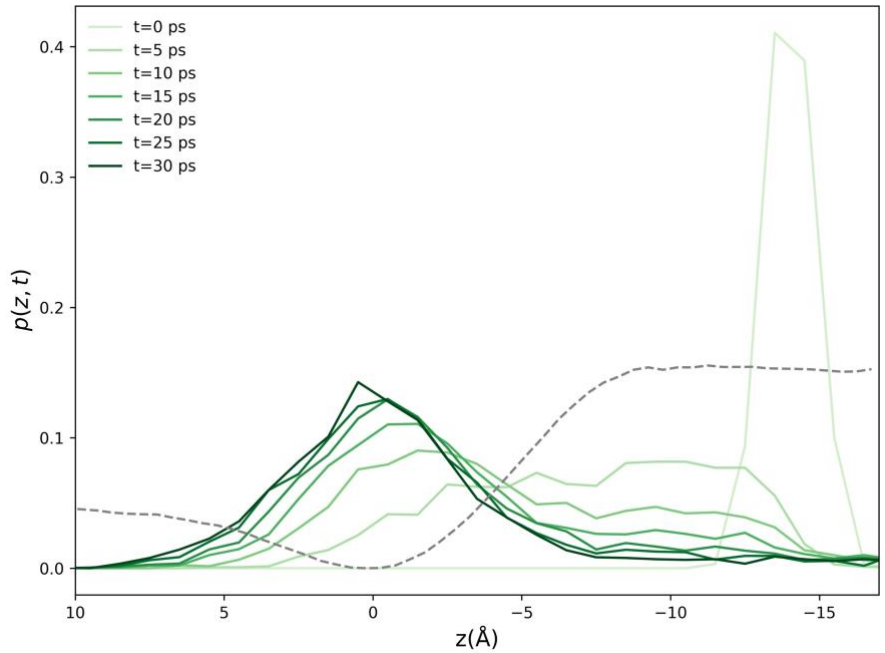

Figure 2.S4. Position probability distribution, p(z, t), of chlorine's MD shooting trajectories. The initial position is a gaussian centered around $z = -14$Å with initial velocity pointed towards the squalene slab. Chlorine's solvation PMF is shown with a dashed line and time traces are shown in green with darker colors corresponding to later time.

After 30ps trajectories cluster around the PMF minima with slow solvation into the bulk. When chlorine diffuses in the gas phase ($t = 0 \rightarrow t = 5$ ps), it does so quickly as it experiences very little friction. As it approaches the liquid slab it experiences increasing friction, and its position distribution changes very slightly from $t = 15ps \rightarrow t = 30ps$. These changes in the position probability distribution with time, encode the friction experienced by a chlorine molecule as it transitions from gas to bulk. The optimized friction $\gamma(z)$ should recover the probability distribution observed in the explicit MD shooting trajectories to properly describe the system. We then continue to launch simulations of the Fokker-Planck (FP) equation of motion for a variety of fit parameters to the functional form of the position dependent friction $\gamma(z)$ (Eq. (2.6) in the main text). For each random set of fit parameters, FP dynamics are propagated for 30 ps and probability distributions are computed every 1 ps. By constraining that the set of fit parameters will display the minimal difference between the position and velocity probability distribution of that set, and that obtained directly from MD, we can assure an accurate interpolation of the friction function from gas to bulk. The optimization was implemented in Julia following the code presented in Ref. [41] using a second-order central finite difference for derivative operators, and fourth order Runga-Kutta propagation scheme for the Fokker-Planck equation. Fig. 2.S5 shows the comparison between the position probability distribution calculated from the Fokker-Planck dynamics of the converged optimized friction $\gamma(z)$ and the MD shooting trajectories.

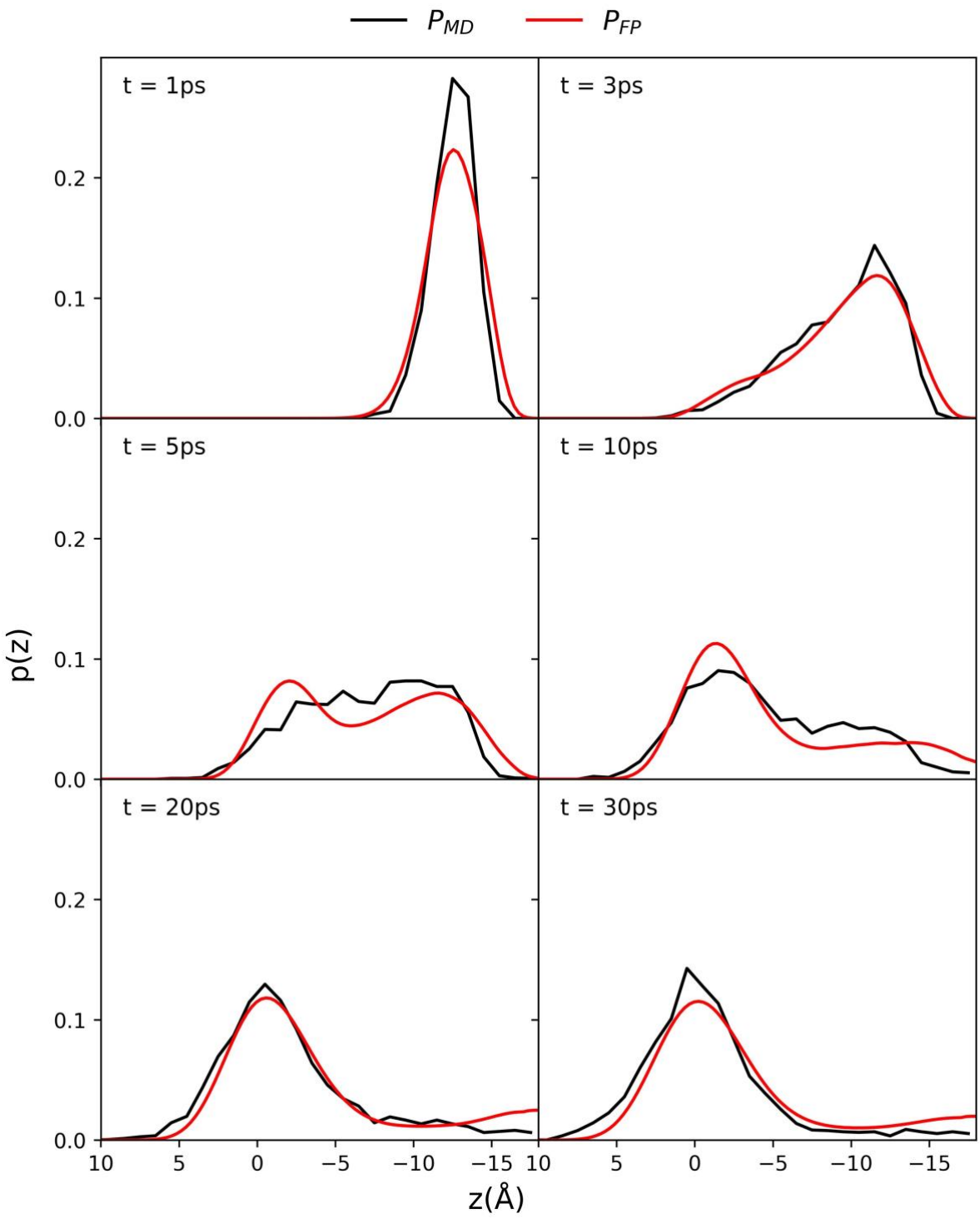

Figure 2.S5. Comparison of the position probability distribution between Fokker-Planck (FP) propagated dynamics with the converged friction function shown in red and the shooting trajectories from MD shown in black.

The Fokker-Planck propagated dynamics with the optimal friction parameter fit is in reasonable agreement with the MD shooting trajectories and features; replicating the transition from a single to bimodal distribution as Cl_2 encounters the interface.

The resulting friction profile is shown in Fig. 2.S6 and indicates that chlorine is influenced by fluctuating long-range dispersion forces between chlorine and squalene molecules far away from the Gibbs dividing surface. The friction profile is changing by four orders of magnitude transitioning from gas to bulk.

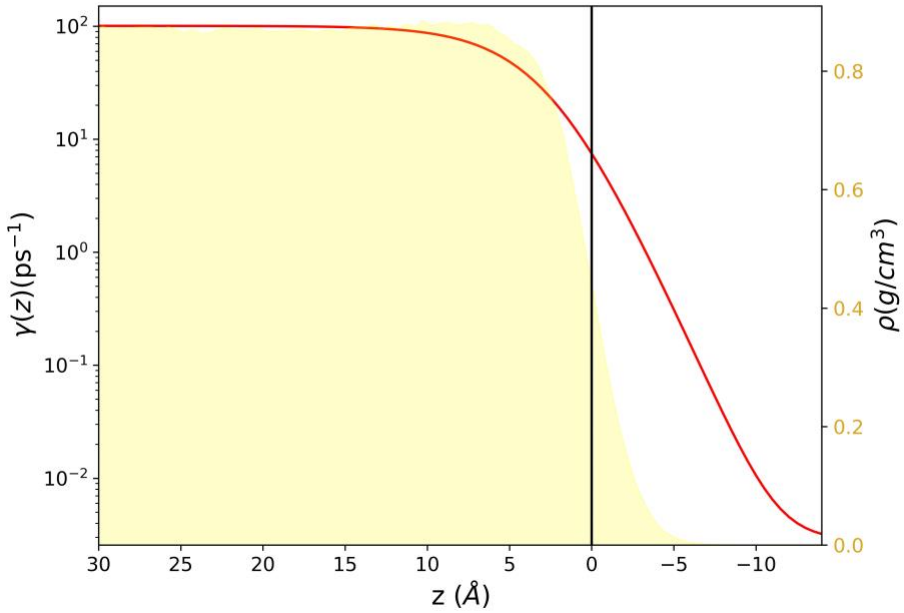

Figure 2.S6. Position dependent friction profile along the z axis is shown in red. Squalene slab density is shown as a shaded yellow area and scaled to fit axis. The Gibbs dividing surface is marked with a vertical line at $z = 0$Å.

2.5. Section S7: Interfacial Pre-exponential Factor Calculation

The position dependent encounter probability, C=C double bond density, chlorine diffusion constant and the pre-exponential factor are presented in Table 2.S5. $z(\text{Å})$ values are shifted to the Gibbs dividing surface as shown in main text.

Table 2.S5. Physical quantities used to calculate the interfacial pre-exponential factor.

$z(\text{Å})$	$P_{Cl_2-C_{Ter}}$	Correction of terminal DB to total DB density	$P_{Cl_2-C_{DB}}$	$\rho_{C_{DB}}$ (normalized to 1 in bulk)	D_{Cl_2} $(cm^2 s^{-1})$	$A_{interface}$ low limit (equally weighted)	$\frac{A_{interface}}{A_{bulk}}$ lower limit	$A_{interface}$ upper limit*	$\frac{A_{interface}}{A_{bulk}}$ upper limit*
Bulk	1.0	1.0	1.0	1.00E+00	3.49E-06	3.49E-06	1.0	3.49E-06	1.0
5	1.0	0.8	0.8	1.00E+00	7.23E-06	6.16E-06	1.8	6.16E-06	1.8
4.5	1.0	0.9	0.9	9.98E-01	8.12E-06	7.23E-06	2.1	7.23E-06	2.1
4	1.0	0.9	0.9	9.88E-01	9.25E-06	8.62E-06	2.5	8.62E-06	2.5
3.5	1.0	1.0	1.0	9.74E-01	1.07E-05	1.05E-05	3.0	1.05E-05	3.0
3	1.0	1.1	1.1	9.53E-01	1.26E-05	1.29E-05	3.7	1.29E-05	3.7
2.5	1.0	1.2	1.2	9.19E-01	1.51E-05	1.59E-05	4.6	1.59E-05	4.6
2	1.0	1.2	1.2	8.70E-01	1.83E-05	1.96E-05	5.6	1.96E-05	5.6
1.5	1.0	1.3	1.3	8.06E-01	2.26E-05	2.41E-05	6.9	2.41E-05	6.9
1	1.0	1.4	1.4	7.26E-01	2.84E-05	2.92E-05	8.4	2.92E-05	8.4
0.5	1.0	1.5	1.5	6.35E-01	3.63E-05	3.41E-05	9.8	3.41E-05	9.8
0	1.0	1.6	1.5	5.36E-01	4.70E-05	3.88E-05	11.1	3.88E-05	11.1
-0.5	1.0	1.7	1.6	4.36E-01	6.18E-05	4.42E-05	12.7	6.71E-03	1922.9
-1	1.0	1.8	1.8	3.42E-01	8.23E-05	5.16E-05	14.8	5.88E-03	1686.1
-1.5	1.2	1.9	2.3	2.57E-01	1.11E-04	6.45E-05	18.5	5.47E-03	1566.1
-2	1.2	2.0	2.5	1.87E-01	1.51E-04	6.94E-05	19.9	4.32E-03	1238.0
-2.5	1.3	2.1	2.7	1.30E-01	2.08E-04	7.35E-05	21.1	3.33E-03	952.8
-3	1.3	2.2	2.9	8.73E-02	2.88E-04	7.23E-05	20.7	2.36E-03	676.0
-3.5	1.4	2.3	3.1	5.67E-02	4.02E-04	7.14E-05	20.5	1.67E-03	478.2
-4	1.5	2.4	3.5	3.58E-02	5.65E-04	7.16E-05	20.5	1.19E-03	341.1
-4.5	1.6	2.5	4.1	2.15E-02	7.98E-04	7.00E-05	20.1	8.24E-04	236.1
-5	1.7	2.6	4.5	1.29E-02	1.13E-03	6.59E-05	18.9	5.47E-04	156.6
-5.5	1.9	2.7	5.2	7.25E-03	1.61E-03	6.08E-05	17.4	3.54E-04	101.6
-6	2.4	2.7	6.7	4.12E-03	2.30E-03	6.32E-05	18.1	2.59E-04	74.1
-6.5	2.7	2.8	7.5	2.34E-03	3.28E-03	5.73E-05	16.4	1.64E-04	47.0
-7	2.9	2.8	8.2	1.27E-03	4.67E-03	4.83E-05	13.8	9.71E-05	27.8
-7.5	2.9	2.8	8.2	6.68E-04	6.64E-03	3.64E-05	10.4	5.15E-05	14.8
-8	2.9	2.9	8.4	3.82E-04	9.40E-03	3.03E-05	8.7	3.03E-05	8.7

*We can calculate an upper limit for the pre-exponential factor by assuming that reactivity is dominated by the faster chlorine molecules arriving from the gas phase. For this assumption we assert that the diffusion constant of chlorine after the Gibbs surface ($z = 0$ Å) is equated to the gas edge of the interfacial region D at $z = -8$Å.

We can compute an overall enhancement of the pre-exponential factor by integrating over the whole interfacial region, which we define by the decay in the C=C double bond density (from $z = -8$Å in the gas phase to $z = 5$Å in the bulk. The pre-exponential factor at the surface is at a lower limit 12X and up to 437X larger than bulk.

2.6. References

(1) Ruiz-Lopez, M. F.; Francisco, J. S.; Martins-Costa, M. T. C.; Anglada, J. M. Molecular Reactions at Aqueous Interfaces. *Nat. Rev. Chem.* **2020**, *4* (9), 459–475. https://doi.org/10.1038/s41570-020-0203-2.

(2) Wei, Z.; Li, Y.; Cooks, R. G.; Yan, X. Accelerated Reaction Kinetics in Microdroplets: Overview and Recent Developments. *Annu. Rev. Phys. Chem.* **2020**, *71* (Volume 71, 2020), 31–51. https://doi.org/10.1146/annurev-physchem-121319-110654.

(3) Ahmed, M.; Blum, M.; Crumlin, E. J.; Geissler, P. L.; Head-Gordon, T.; Limmer, D. T.; Mandadapu, K. K.; Saykally, R. J.; Wilson, K. R. Molecular Properties and Chemical Transformations Near Interfaces. *J. Phys. Chem. B* **2021**, *125* (32), 9037–9051. https://doi.org/10.1021/acs.jpcb.1c03756.

(4) LaCour, R. A.; Heindel, J. P.; Zhao, R.; Head-Gordon, T. The Role of Interfaces and Charge for Chemical Reactivity in Microdroplets. *J. Am. Chem. Soc.* **2025**, *147* (8), 6299–6317. https://doi.org/10.1021/jacs.4c15493.

(5) Galib, M.; Limmer, D. T. Reactive Uptake of N2O5 by Atmospheric Aerosol Is Dominated by Interfacial Processes. *Science* **2021**, *371* (6532), 921–925. https://doi.org/10.1126/science.abd7716.

(6) Moon, S.; Limmer, D. T. Enhanced ClNO2 Formation at the Interface of Sea-Salt Aerosol. *J. Phys. Chem. Lett.* **2024**, *15* (37), 9466–9473. https://doi.org/10.1021/acs.jpclett.4c02289.

(7) M. Prophet, A.; Polley, K.; Berkel, G. J. V.; T. Limmer, D.; R. Wilson, K. Iodide Oxidation by Ozone at the Surface of Aqueous Microdroplets. *Chem. Sci.* **2024**, *15* (2), 736–756. https://doi.org/10.1039/D3SC04254E.

(8) Gong, C.; Yuan, X.; Xing, D.; Zhang, D.; Martins-Costa, M. T. C.; Anglada, J. M.; Ruiz-López, M. F.; Francisco, J. S.; Zhang, X. Fast Sulfate Formation Initiated by the Spin-Forbidden Excitation of SO2 at the Air–Water Interface. *J. Am. Chem. Soc.* **2022**, *144* (48), 22302–22308. https://doi.org/10.1021/jacs.2c10830.

(9) Zhong, J.; Zhao, Y.; Li, L.; Li, H.; Francisco, J. S.; Zeng, X. C. Interaction of the NH2 Radical with the Surface of a Water Droplet. *J. Am. Chem. Soc.* **2015**, *137* (37), 12070–12078. https://doi.org/10.1021/jacs.5b07354.

(10) Zhu, C.; Kumar, M.; Zhong, J.; Li, L.; Francisco, J. S.; Zeng, X. C. New Mechanistic Pathways for Criegee–Water Chemistry at the Air/Water Interface. *J. Am. Chem. Soc.* **2016**, *138* (35), 11164–11169. https://doi.org/10.1021/jacs.6b04338.

(11) Fang, Y.-G.; Wei, L.; Francisco, J. S.; Zhu, C.; Fang, W.-H. Mechanistic Insights into Chloric Acid Production by Hydrolysis of Chlorine Trioxide at an Air–Water Interface. *J. Am. Chem. Soc.* **2024**, *146* (30), 21052–21060. https://doi.org/10.1021/jacs.4c06269.

(12) Narayan, S.; Muldoon, J.; Finn, M. G.; Fokin, V. V.; Kolb, H. C.; Sharpless, K. B. "On Water": Unique Reactivity of Organic Compounds in Aqueous Suspension. *Angew. Chem. Int. Ed.* **2005**, *44* (21), 3275–3279. https://doi.org/10.1002/anie.200462883.

(13) Song, X.; Basheer, C.; Zare, R. N. Making Ammonia from Nitrogen and Water Microdroplets. *Proc. Natl. Acad. Sci.* **2023**, *120* (16), e2301206120. https://doi.org/10.1073/pnas.2301206120.

(14) Zhou, S.; Hwang, B. C. H.; Lakey, P. S. J.; Zuend, A.; Abbatt, J. P. D.; Shiraiwa, M. Multiphase Reactivity of Polycyclic Aromatic Hydrocarbons Is Driven by Phase Separation and Diffusion Limitations. *Proc. Natl. Acad. Sci.* **2019**, *116* (24), 11658–11663. https://doi.org/10.1073/pnas.1902517116.

(15) Gong, K.; Nandy, A.; Song, Z.; Li, Q.-S.; Hassanali, A.; Cassone, G.; Banerjee, S.; Xie, J. Revisiting the Enhanced Chemical Reactivity in Water Microdroplets: The Case of a Diels–Alder Reaction. *J. Am. Chem. Soc.* **2024**, *146* (46), 31585–31596. https://doi.org/10.1021/jacs.4c09400.
(16) Davidovits, P.; Kolb, C. E.; Williams, L. R.; Jayne, J. T.; Worsnop, D. R. Mass Accommodation and Chemical Reactions at Gas−Liquid Interfaces. *Chem. Rev.* **2006**, *106* (4), 1323–1354. https://doi.org/10.1021/cr040366k.
(17) Zeng, M.; Wilson, K. R. Experimental Evidence That Halogen Bonding Catalyzes the Heterogeneous Chlorination of Alkenes in Submicron Liquid Droplets. *Chem. Sci.* **2021**, *12* (31), 10455–10466. https://doi.org/10.1039/D1SC02662C.
(18) Roper, G. H. The Kinetics of the Addition of Chlorine to Olefins in Carbon Tetrachloride. *Chem. Eng. Sci.* **1953**, *2* (1), 27–31. https://doi.org/10.1016/0009-2509(53)80004-7.
(19) Yates, K.; Leung, H. W. Kinetics and Stereochemistry of the Addition of Chlorine to Styrenes. *J. Org. Chem.* **1980**, *45* (8), 1401–1406. https://doi.org/10.1021/jo01296a011.
(20) Worsnop, D. R.; Morris, J. W.; Shi, Q.; Davidovits, P.; Kolb, C. E. A Chemical Kinetic Model for Reactive Transformations of Aerosol Particles. *Geophys. Res. Lett.* **2002**, *29* (20), 57-1-57–4. https://doi.org/10.1029/2002GL015542.
(21) Thompson, A. P.; Aktulga, H. M.; Berger, R.; Bolintineanu, D. S.; Brown, W. M.; Crozier, P. S.; in 't Veld, P. J.; Kohlmeyer, A.; Moore, S. G.; Nguyen, T. D.; Shan, R.; Stevens, M. J.; Tranchida, J.; Trott, C.; Plimpton, S. J. LAMMPS - a Flexible Simulation Tool for Particle-Based Materials Modeling at the Atomic, Meso, and Continuum Scales. *Comput. Phys. Commun.* **2022**, *271*, 108171. https://doi.org/10.1016/j.cpc.2021.108171.
(22) Malde, A. K.; Zuo, L.; Breeze, M.; Stroet, M.; Poger, D.; Nair, P. C.; Oostenbrink, C.; Mark, A. E. An Automated Force Field Topology Builder (ATB) and Repository: Version 1.0. *J. Chem. Theory Comput.* **2011**, *7* (12), 4026–4037. https://doi.org/10.1021/ct200196m.
(23) Schmid, N.; Eichenberger, A. P.; Choutko, A.; Riniker, S.; Winger, M.; Mark, A. E.; van Gunsteren, W. F. Definition and Testing of the GROMOS Force-Field Versions 54A7 and 54B7. *Eur. Biophys. J.* **2011**, *40* (7), 843–856. https://doi.org/10.1007/s00249-011-0700-9.
(24) Andersen, H. C. Rattle: A "Velocity" Version of the Shake Algorithm for Molecular Dynamics Calculations. *J. Comput. Phys.* **1983**, *52* (1), 24–34. https://doi.org/10.1016/0021-9991(83)90014-1.
(25) Hockney, R. W.; Eastwood, J. W. *Computer Simulation Using Particles*, Special student ed.; A. Hilger: Bristol [England] ; Philadelphia, 1988.
(26) Martínez, L.; Andrade, R.; Birgin, E. G.; Martínez, J. M. PACKMOL: A package for building initial configurations for molecular dynamics simulations. *J. Comput. Chem.* **2009**, *30* (13), 2157–2164. https://doi.org/10.1002/jcc.21224.
(27) Grossfield, A. WHAM: The Weighted Histogram Analysis Method. , http://membrane.urmc.rochester.edu/content/wham/.
(28) Kumar, S.; Rosenberg, J. M.; Bouzida, D.; Swendsen, R. H.; Kollman, P. A. THE Weighted Histogram Analysis Method for Free-Energy Calculations on Biomolecules. I. The Method. *J. Comput. Chem.* **1992**, *13* (8), 1011–1021. https://doi.org/10.1002/jcc.540130812.
(29) Kumar, S.; Rosenberg, J. M.; Bouzida, D.; Swendsen, R. H.; Kollman, P. A. Multidimensional Free-Energy Calculations Using the Weighted Histogram Analysis Method. *J. Comput. Chem.* **1995**, *16* (11), 1339–1350. https://doi.org/10.1002/jcc.540161104.

(30) Taylor, N. W.; Hildebrand, J. H. Solubility. VIII. Solubility Relations Of Certain Gases. *J. Am. Chem. Soc.* **1923**, *45* (3), 682–694. https://doi.org/10.1021/ja01656a018.
(31) Souaille, M.; Roux, B. Extension to the Weighted Histogram Analysis Method: Combining Umbrella Sampling with Free Energy Calculations. *Comput. Phys. Commun.* **2001**, *135* (1), 40–57. https://doi.org/10.1016/S0010-4655(00)00215-0.
(32) Willis, M. D.; Wilson, K. R. Coupled Interfacial and Bulk Kinetics Govern the Timescales of Multiphase Ozonolysis Reactions. *J. Phys. Chem. A* **2022**, *126* (30), 4991–5010. https://doi.org/10.1021/acs.jpca.2c03059.
(33) Hinsberg, W.; Houle, F. Kinetiscope. https://hinsberg.net/kinetiscope/ (accessed 2025-03-01).
(34) Gerber, R. B.; Varner, M. E.; Hammerich, A. D.; Riikonen, S.; Murdachaew, G.; Shemesh, D.; Finlayson-Pitts, B. J. *Computational Studies of Atmospherically-Relevant Chemical Reactions in Water Clusters and on Liquid Water and Ice Surfaces*. ACS Publications. https://doi.org/10.1021/ar500431g.
(35) Li, H.; Wang, X.; Zhong, J.; Chu, B.; Ma, Q.; Zeng, X. C.; Francisco, J. S.; He, H. Mechanistic Study of the Aqueous Reaction of Organic Peroxides with HSO3− on the Surface of a Water Droplet. *Angew. Chem.* **2021**, *133* (37), 20362–20365. https://doi.org/10.1002/ange.202105416.
(36) Xu, Q.; Ma, F.; Xia, D.; Li, X.; Chen, J.; Xie, H.-B.; Francisco, J. S. Two-Step Noncatalyzed Hydrolysis Mechanism of Imines at the Air–Water Interface. *J. Am. Chem. Soc.* **2024**, *146* (42), 28866–28873. https://doi.org/10.1021/jacs.4c09080.
(37) von Domaros, M.; Liu, Y.; Butman, J. L.; Perlt, E.; Geiger, F. M.; Tobias, D. J. Molecular Orientation at the Squalene/Air Interface from Sum Frequency Generation Spectroscopy and Atomistic Modeling. *J. Phys. Chem. B* **2021**, *125* (15), 3932–3941. https://doi.org/10.1021/acs.jpcb.0c11158.
(38) Lakey, P. S. J.; Morrison, G. C.; Won, Y.; Parry, K. M.; von Domaros, M.; Tobias, D. J.; Rim, D.; Shiraiwa, M. The Impact of Clothing on Ozone and Squalene Ozonolysis Products in Indoor Environments. *Commun. Chem.* **2019**, *2* (1), 1–8. https://doi.org/10.1038/s42004-019-0159-7.
(39) Ocko, B. M.; Wu, X. Z.; Sirota, E. B.; Sinha, S. K.; Deutsch, M. X-Ray Reflectivity Study of Thermal Capillary Waves on Liquid Surfaces. *Phys. Rev. Lett.* **1994**, *72* (2), 242–245. https://doi.org/10.1103/PhysRevLett.72.242.
(40) Ghoufi, A.; Malfreyt, P.; Tildesley, D. J. Computer Modelling of the Surface Tension of the Gas–Liquid and Liquid–Liquid Interface. *Chem. Soc. Rev.* **2016**, *45* (5), 1387–1409. https://doi.org/10.1039/C5CS00736D.
(41) Polley, K.; Wilson, K. R.; Limmer, D. T. On the Statistical Mechanics of Mass Accommodation at Liquid–Vapor Interfaces. *J. Phys. Chem. B* **2024**, *128* (17), 4148–4157. https://doi.org/10.1021/acs.jpcb.4c00899.
(42) Tang, M. J.; Cox, R. A.; Kalberer, M. Compilation and Evaluation of Gas Phase Diffusion Coefficients of Reactive Trace Gases in the Atmosphere: Volume 1. Inorganic Compounds. *Atmospheric Chem. Phys.* **2014**, *14* (17), 9233–9247. https://doi.org/10.5194/acp-14-9233-2014.
(43) Shimizu, N.; Ito, J.; Kato, S.; Otoki, Y.; Goto, M.; Eitsuka, T.; Miyazawa, T.; Nakagawa, K. Oxidation of Squalene by Singlet Oxygen and Free Radicals Results in Different Compositions of Squalene Monohydroperoxide Isomers. *Sci. Rep.* **2018**, *8* (1), 9116. https://doi.org/10.1038/s41598-018-27455-5.

(44) Kropp, P. J.; Daus, K. A.; Tubergen, M. W.; Kepler, K. D.; Wilson, V. P.; Craig, S. L.; Baillargeon, M. M.; Breton, G. W. Surface-Mediated Reactions. 3. Hydrohalogenation of Alkenes. *J. Am. Chem. Soc.* **1993**, *115* (8), 3071–3079. https://doi.org/10.1021/ja00061a005.
(45) ATB, Squalene, PJMU. https://atb.uq.edu.au/molecule.py?molid=366488.
(46) ATB, Chlorine, E0W4. https://atb.uq.edu.au/molecule.py?molid=305477.
(47) von Domaros, M.; Liu, Y.; Butman, J. L.; Perlt, E.; Geiger, F. M.; Tobias, D. J. Molecular Orientation at the Squalene/Air Interface from Sum Frequency Generation Spectroscopy and Atomistic Modeling. *J. Phys. Chem. B* **2021**, *125* (15), 3932–3941. https://doi.org/10.1021/acs.jpcb.0c11158.
(48) Jorgensen, W. L.; Maxwell, D. S.; Tirado-Rives, J. Development and Testing of the OPLS All-Atom Force Field on Conformational Energetics and Properties of Organic Liquids. *J. Am. Chem. Soc.* **1996**, *118* (45), 11225–11236. https://doi.org/10.1021/ja9621760.
(49) Siu, S. W. I.; Pluhackova, K.; Böckmann, R. A. Optimization of the OPLS-AA Force Field for Long Hydrocarbons. *J. Chem. Theory Comput.* **2012**, *8* (4), 1459–1470. https://doi.org/10.1021/ct200908r.
(50) Haynes, W. M. *CRC Handbook of Chemistry and Physics, 95th Edition*, 95th ed.; CRC Press: Hoboken, 2014.
(51) Houle, F. A.; Hinsberg, W. D.; Wilson, K. R. Oxidation of a Model Alkane Aerosol by OH Radical: The Emergent Nature of Reactive Uptake. *Phys. Chem. Chem. Phys.* **2015**, *17* (6), 4412–4423. https://doi.org/10.1039/C4CP05093B.
(52) Liu, M. J.; Wiegel, A. A.; Wilson, K. R.; Houle, F. A. Aerosol Fragmentation Driven by Coupling of Acid–Base and Free-Radical Chemistry in the Heterogeneous Oxidation of Aqueous Citric Acid by OH Radicals. *J. Phys. Chem. A* **2017**, *121* (31), 5856–5870. https://doi.org/10.1021/acs.jpca.7b04892.
(53) Wiegel, A. A.; Liu, M. J.; Hinsberg, W. D.; Wilson, K. R.; Houle, F. A. Diffusive Confinement of Free Radical Intermediates in the OH Radical Oxidation of Semisolid Aerosols. *Phys. Chem. Chem. Phys.* **2017**, *19* (9), 6814–6830. https://doi.org/10.1039/C7CP00696A.
(54) Heine, N.; Houle, F. A.; Wilson, K. R. Connecting the Elementary Reaction Pathways of Criegee Intermediates to the Chemical Erosion of Squalene Interfaces during Ozonolysis. *Environ. Sci. Technol.* **2017**, *51* (23), 13740–13748. https://doi.org/10.1021/acs.est.7b04197.
(55) Houle, F. A.; Wiegel, A. A.; Wilson, K. R. Predicting Aerosol Reactivity Across Scales: From the Laboratory to the Atmosphere. *Environ. Sci. Technol.* **2018**, *52* (23), 13774–13781. https://doi.org/10.1021/acs.est.8b04688.
(56) Houle, F. A.; Wiegel, A. A.; Wilson, K. R. Changes in Reactivity as Chemistry Becomes Confined to an Interface. The Case of Free Radical Oxidation of C30H62 Alkane by OH. *J. Phys. Chem. Lett.* **2018**, *9* (5), 1053–1057. https://doi.org/10.1021/acs.jpclett.8b00172.
(57) Heine, N.; Arata, C.; Goldstein, A. H.; Houle, F. A.; Wilson, K. R. Multiphase Mechanism for the Production of Sulfuric Acid from SO2 by Criegee Intermediates Formed During the Heterogeneous Reaction of Ozone with Squalene. *J. Phys. Chem. Lett.* **2018**, *9* (12), 3504–3510. https://doi.org/10.1021/acs.jpclett.8b01171.
(58) Wilson, K. R.; Prophet, A. M.; Rovelli, G.; Willis, M. D.; Rapf, R. J.; Jacobs, M. I. A Kinetic Description of How Interfaces Accelerate Reactions in Micro-Compartments. *Chem. Sci.* **2020**, *11* (32), 8533–8545. https://doi.org/10.1039/D0SC03189E.

(59) Fan, H.; Masaya, T. W.; Goulay, F. Effect of Surface–Bulk Partitioning on the Heterogeneous Oxidation of Aqueous Saccharide Aerosols. *Phys. Chem. Chem. Phys.* **2019**, *21* (6), 2992–3001. https://doi.org/10.1039/C8CP06785F.
(60) Vácha, R.; Slavíček, P.; Mucha, M.; Finlayson-Pitts, B. J.; Jungwirth, P. Adsorption of Atmospherically Relevant Gases at the Air/Water Interface: Free Energy Profiles of Aqueous Solvation of N2, O2, O3, OH, H2O, HO2, and H2O2. *J. Phys. Chem. A* **2004**, *108* (52), 11573–11579. https://doi.org/10.1021/jp046268k.

Chapter 3. Molecular Insight into how Alcohol Catalyzes the Interfacial Chlorination of Squalene

3.1. Introduction

Liquid–vapor interfaces are dynamic environments where molecular structure, solvation, and transport properties differ substantially from those in bulk solutions.[1–3] At these boundaries, the interplay between phases gives rise to distinctive reaction landscapes, where selective partitioning, orientation, and modified solvation shells, create nano-environments that can stabilize transition states or bring reactive species into closer proximity.[4–11] While bulk-phase reactions often proceed through well-characterized pathways, interfaces can enable alternative mechanisms, leading to catalytic amplification or unexpected inhibition of reaction rates that are inaccessible in a single phase. These effects can strongly influence chemical reactivity in a wide range of systems, from atmospheric aerosols and cloud droplets to engineered materials and biological membranes. Understanding how changes in composition shape the interfacial environment is essential for interpreting multiphase chemistry and for developing novel approaches to heterogeneous catalysis. In this work, we use squalene chlorination as a model system to explore how the addition of non-reactive long-chain alcohols alters the heterogeneous chlorination rate of squalene. By examining changes in interfacial organization, diffusion, and interfacial solvation free energy, we provide molecular-level insight into how compositional complexity can give rise to catalytic behavior at the liquid-vapor interface.

The chlorination of squalene in small aerosol particles has been previously investigated using mass spectrometry in a flow tube apparatus.[12] These experiments revealed that the presence of alcohols and other oxygenated species, which are unreactive towards Cl_2, significantly accelerates the reaction compared to pure squalene, without altering the product distribution (*i.e.,* acting as a catalyst). Figure 3.1 compares the reaction kinetics of pure squalene with those of a representative mixture containing 80% squalene and 20% of the long-chain alcohol 2-decyl-1-tetradecanol ($C_{24}OH$), hereafter referred to as Sqe/Alc. The measured kinetic decay of squalene with exposure to chlorine gas (Cl_2)[12] is shown in Figure 3.1A. Fitting the decay profile to an exponential function is used to calculate the uptake coefficient, a dimensionless parameter that normalizes the heterogeneous reaction rate relative to the gas–particle collision frequency. A larger uptake coefficient indicates a faster decay rate. The uptake coefficient as a function of temperature is shown in Figure 3.1B. Sqe/Alc exhibits an uptake coefficient that is an order of magnitude larger than the pure system over the temperature range probed in the experiment.

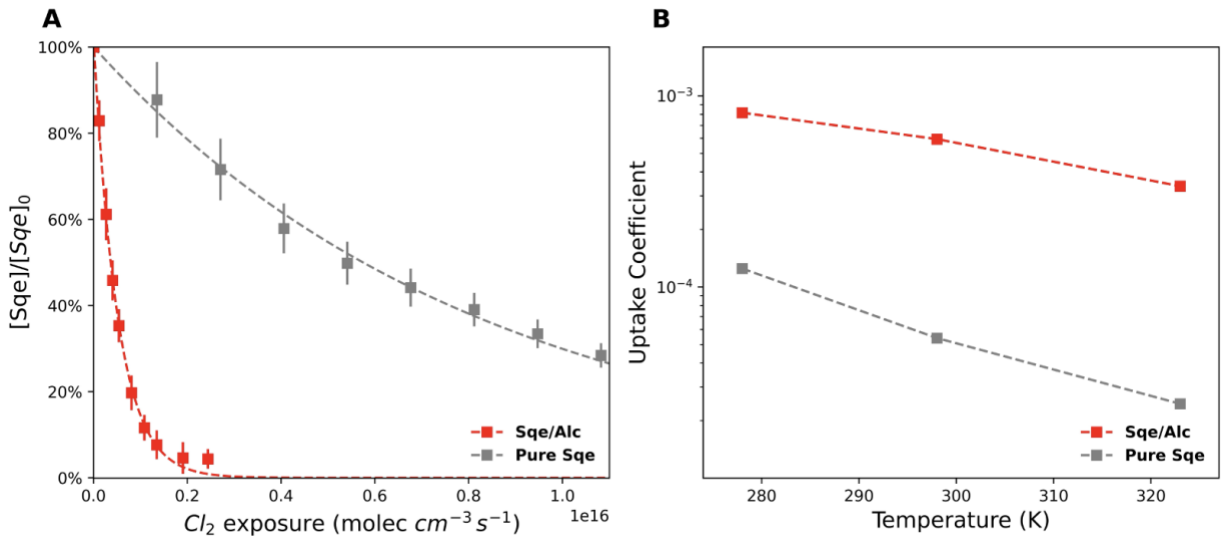

Figure 3.1. Squalene chlorination kinetics of Sqe/Alc (shown in red) and pure squalene (Sqe) (shown in grey), are reproduced from Ref [12]. (A) Normalized decay of squalene signal as a function of Cl_2 exposure. Exponential fit is shown with a dashed line to guide the eye. (B) Uptake coefficient as a function of temperature.

Figure 3.1 raises two key questions: (1) What drives the faster reaction kinetics in the alcohol-containing mixture compared to pure squalene? and (2) Why is the inverse temperature dependence of the uptake coefficient less pronounced in the mixed system than in pure system? To address these questions, we employ molecular dynamics simulations together with kinetic modeling to investigate how the addition of long-chain alcohols modifies interfacial structure and impacts the chlorination kinetics of squalene. Our analysis focuses on changes in interfacial thickness, molecular orientation, and transport properties introduced by alcohol incorporation, and how these factors influence reaction rates in both the surface and bulk regions.

3.2. Methods

To examine the molecular details of the squalene alcohol mixture system, we performed all-atom classical molecular dynamics simulations. Simulations, conducted in LAMMPS[13], used 230 squalene and 58 $C_{24}OH$ molecules in a slab geometry to replicate the mole fraction (20%) of alcohol used in the experiment. A liquid region (~60Å) is enclosed by two interfaces along the z axis with periodic boundary conditions in all directions. The total box dimension is 60 X 60 X 240 Å. The molecular force field for squalene is taken from the Automated Topology Builder (ATb) repository,[14] optimized for GROMOS_54A7.[15] Full details of force field selection for squalene is available in our previous work,[16] and $C_{24}OH$ force field is taken similarly from ATb.[17] Simulations are performed in the canonical ensemble (NVT) using the velocity-Verlet integrator with 2 fs timesteps. Temperature is regulated using a Langevin thermostat with a 1 ps damping time. Carbon-hydrogen bonds are constrained using the RATTLE algorithm.[18] Short-range interactions are described by a Lennard-Jones (LJ) potential truncated at 14Å,

$$U_{LJ}(r) = 4\varepsilon_{ij}\left[\left(\frac{\sigma_{ij}}{r}\right)^{12} - \left(\frac{\sigma_{ij}}{r}\right)^{6}\right], \quad (3.1)$$

where ε_{ij} and σ_{ij} are the energy and size parameters described in GROMOS_54A7[15], and r_{ij} is the distance between atoms. Long range Coulomb interactions are described by Particle–particle–

particle–mesh method[19] with a relative error of 10^{-4}. Initial configurations were generated by PACKMOL[20] and equilibrated for 80ns prior to production runs. The potential of mean force (PMF) for z component of the chlorine center of mass was computed as,

$$F(z) = -k_B T \ln\langle \delta(z - z_0)\rangle + F_0, \tag{3.2}$$

where k_B is Boltzmann's constant, T is temperature, the angle brackets represent an ensemble average for chlorine's center of mass z_0, and F_0 is the reference free energy set to zero at the gas phase. The potential of mean force (PMF) is obtained from umbrella sampling using a biasing potential acting on the chlorine molecule's center of mass of the form,

$$U_{bias}(z) = \frac{1}{2} k(z - z_0)^2, \tag{3.3}$$

where z_0 is the constrained position, z is the instantaneous position, and k is the spring constant. A list of the biased simulation windows and spring constants is presented in Table 3.S1. Reconstruction of the PMF from the biased simulations is done using the Grossfield implementation[21] of the Weighted Histogram Analysis Method (WHAM).[21–25] Calculation of averaged quantities in biased simulation windows is reweighted from WHAM using the method of Souaille and Roux.[25] The mass accommodation coefficient is computed from trajectories obtained from an independent series of simulations. For each trajectory, a Cl_2 is initially placed at the at the Gibbs dividing surface, its z position is recorded until it enters the either the gas or liquid regions of the simulation, defined as 10Å above or below the Gibbs dividing surface. The mass accommodation is computed as,

$$\alpha = \frac{n_\mathrm{b}}{n_\mathrm{g} + n_\mathrm{b}}, \tag{3.4}$$

where n_b is the number of trajectories where chlorine enters the bulk region of the liquid and n_g is the number of trajectories where chlorine enters the gas region.

Bulk diffusivities are calculated from non-biased 150ns simulation trajectories using mean-squared displacement analysis limited to the bulk region ($-10 < z < 10$ Å),

$$D = \lim_{t\to\infty} \frac{\langle |r(t) - r_0|^2 \rangle}{6\,t}, \tag{3.5}$$

where r is the center of mass position, D is the diffusion constant, and t is time. To characterize the diffusive behavior of Cl_2 near the interface, we run trajectories by placing chlorine in the gas phase, parameterized as a Gaussian centered at $z = -15$Å with an initial velocity directed towards the slab. Chlorine's center of mass position and velocity were recorded in the z direction, to constrain the friction profile of a Cl_2 molecule in the interfacial region following a procedure developed by Polley et al.[26]

Kinetic modelling of squalene chlorination in aerosols containing a liquid mixture of squalene and $C_{24}OH$ is implemented in Kinetiscope,[27] using a framework developed by Willis and Wilson,[28] and previously implemented in our work modeling pure squalene chlorination.[16] The aerosol particle is simplified into two reaction compartments: surface and bulk. Model parameters are directly constrained from the molecular simulations, and complete model assumptions and parameters are provided in the Supporting Information.

3.3. Results and Discussion

Previous aerosol measurements of this reaction[12] provide valuable information on multiphase reactivity and offer indirect insights into the interfacial environment due to their high

surface-to-volume ratio. Since measurements alone are not capable of directly probing the chemical composition at the interface, MD simulations are used as a computational microscope to examine the squalene/alcohol liquid mixture distribution across the interfacial region. Figure 3.2A shows the density profile for the Sqe/Alc system. Contrary to the hypothesis made in the experimental work,[12] the long chain alcohol $C_{24}OH$ does not partition to the interface but is, in fact, repelled from the Gibbs dividing surface (see horizontal line in Fig. 3.2A). Instead, alcohol groups are found to be enriched (~40% more than in the bulk) in a sub-surface layer located ~1 nm below the interface.

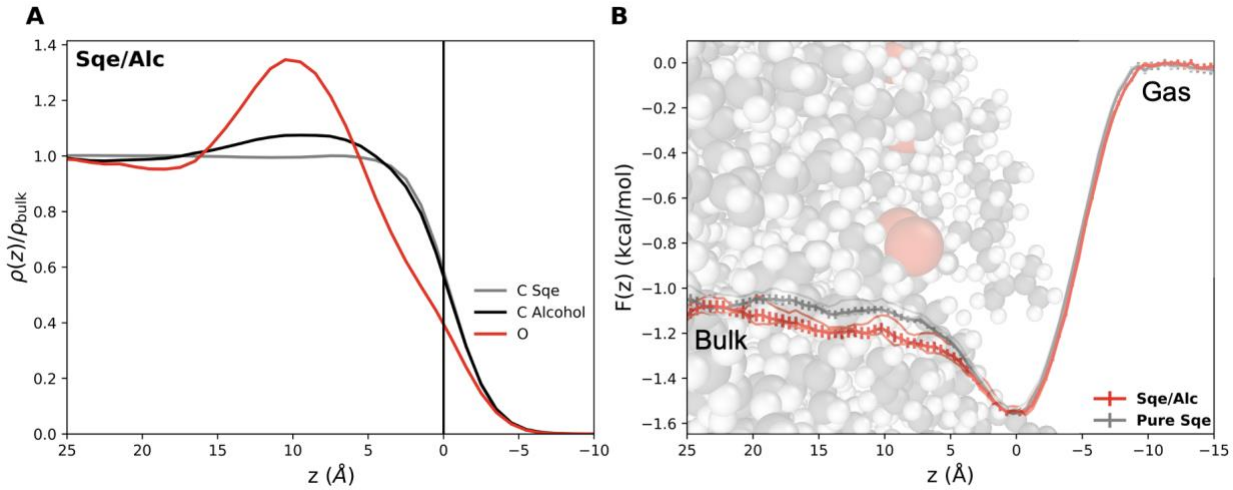

Figure 3.2. (A) Density profile along the slab axis z of Sqe/Alc system normalized to bulk values. The Gibbs Dividing surface is marked with a black horizontal line at $z = 0$ Å, with positive z values corresponding to the bulk liquid and negative z values to the gas region. (B) The potential of mean force (PMF) for chlorine solvation along the z axis in both pure squalene (Sqe) and Sqe/Alc. Light grey and red lines represent half the data to exemplify PMF precision. (*Inset*) MD snapshot of Sqe/Alc slab, carbon is shown in grey, hydrogen in white, and oxygen in red.

The PMF for chlorine solvation in Sq/Alc is shown in Figure 3.2B with the pure squalene system shown for comparison. The addition of $C_{24}OH$ does not influence the overall bulk solubility of chlorine as indicated by the similar free energy differences between gas and bulk for the two systems. The solvation of Cl_2 in Sq/Alc is slightly more favorable in the sub-surface region corresponding to the peak of the alcohol group distribution along the slab axis z (Figure 3.2A).

Since there is no significant change to chlorine's solubility with the addition of alcohol, the experimental results in Figure 3.1 cannot be explained simply by differences in the concentration of Cl_2 in the aerosol. Rather, alkene chlorination is known to exhibit a strong dependence on solvent polarity, since the electrophilic addition mechanism is thought to proceed through polarizable intermediates such as carbocations or carbon radicals, whose stabilization by polar solvents accelerates reaction rates.[29–33] Shown in Fig. 3.S1 is a compilation of experimental reaction rate coefficients are plotted as a function of the solvent dielectric constant. Remarkably, a small increase in solvent polarity, from non-polar carbon tetrachloride ($\kappa = 2.2$)[34] to moderately polar acetic acid ($\kappa = 6.2$),[34] increases the reaction rate by two orders of magnitude. Since, to the best of our knowledge, there are no known bulk rates for squalene chlorination in $C_{24}OH$, we proceed to further analyze simulation results and construct a kinetic model in an attempt to offer a quantitative explanation for the aerosol experimental results (Figure 3.1).

In our previous work on the chlorination reaction in pure squalene nanodroplets,[16] we found evidence that the interfacial rate constant was about two orders of magnitude faster than in the bulk liquid. We identified two mechanisms for this interfacial acceleration: (1) faster diffusion of chlorine at the interface, and (2) a unique mechanism termed "tail spearfishing", in which squalene tails, protruding into the gas phase, exert a thermodynamic force that increases the chlorine–double bond encounter probability. Both mechanisms increase the reaction rate via the pre-exponential factor (A) in the Arrhenius equation, $k = Ae^{-\frac{E_a}{k_B T}}$, without altering the elementary reaction steps or lowering the activation energy. As such, their influence on the reaction kinetics might persist quantitatively in the mixed system, even if the reaction mechanism is altered by the presence of alcohol, since changes to the pre-exponential factor - governed by diffusion and molecular encounter frequency - are generally less sensitive to the specific chemical pathway than the activation energy. Figure 3.2A indicates that the addition of $C_{24}OH$ results in the subsurface enrichment of the alcohol group with the carbon chains distributed both towards the interface and the bulk, thus, it becomes critical to determine whether the two interfacial mechanisms identified in the pure system remain operative in the alcohol mixture.

To determine if squalene tails in the Sqe/Alc system persist in interacting more frequently with chlorine at the interface, we compute the average probability of contact between Cl_2 and a carbon in a double bond conditioned on the chlorine's $z$position. Contact is defined as the average number of simulation timesteps in which the shortest atomic distance between a chlorine atom in Cl_2 and a carbon atom in a squalene C=C double bond is less than 3.5Å (Figure 3.3A). This cutoff coincides with the Lennard-Jones sigma parameter between Cl and C is $\sigma_{Cl-C} = 3.52$Å, corresponding to the effective interaction range where steric and van der Waals forces begin to influence reactivity.

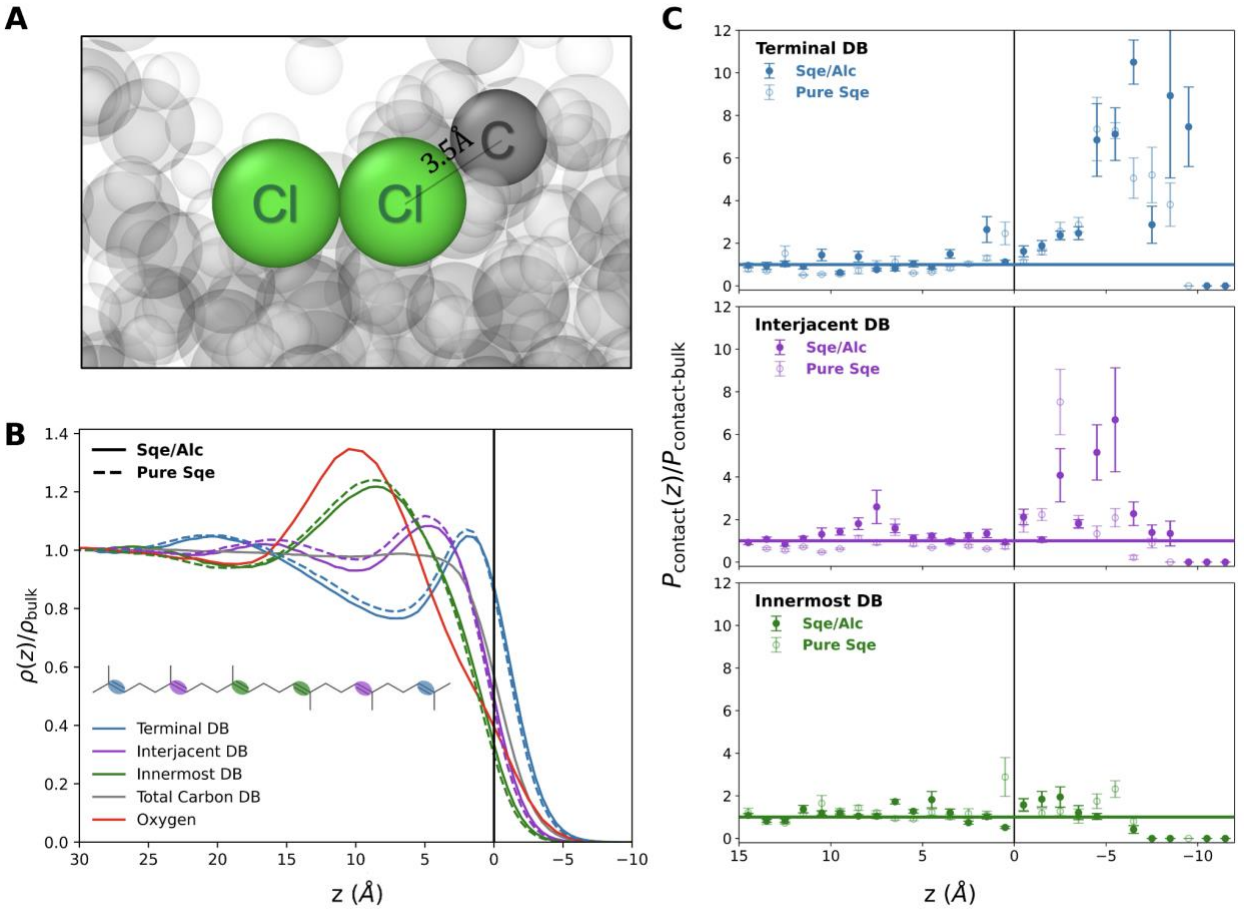

Figure 3.3. (A) Cartoon depicting the definition of contact between a chlorine atom in Cl_2 and a carbon in a double bond of squalene. Contact is computed as the average number of timesteps in which a chlorine atom is at a distance smaller 3.5Å. (B) Distribution of double bonds (DBs) along the slab axis z, pure squalene system is shown with a dashed line for comparison. Terminal DB shown in blue preferentially stick out towards the gas phase, alcohol oxygen is shown in red and has minimal effect on the distribution of DBs. The Gibbs dividing surface is shown as a horizontal black line at z=0. (Inset) Squalene chemical structure with color coding of DB types. (C) Probability of contact along the slab axis z for all double bond types. Results are shown for both Sqe/Alc (solid colors) and pure squalene (lighter shaded colors). Probabilities are normalized to the total DB density and the bulk average contact probability. A horizontal line at 1 represents the bulk average. Contact on the gas side of the interface is enhanced compared to bulk contact.

Figure 3.3B shows the distribution of C=C double bonds along the *z* axis of the slab. The addition of $C_{24}OH$ does not significantly alter the z-positioning of squalene's C=C double bonds compared to the pure system. This is a key observation; that the alignment of squalene molecules with the surface normal is undisturbed by $C_{24}OH$, despite the enrichment of the alcohol headgroups (shown in red) and their saturated hydrocarbon tails near the interface. Figure 3.3C shows the probability of Cl_2 and C=C double bond contact for the three types of double bonds in squalene, normalized to the total double bond density and the average contact probability in the bulk. Similar to the pure squalene system, terminal C=C double bonds in the squalene tails that extend into the gas side of the interface, interact with increased probability with chlorine, up to an order of magnitude more frequently than in the bulk. This effect is observed to be perhaps even more pronounced in the Sqe/Alc system than in the pure system, showing some additional interaction of the interjacent double bonds with chlorine.

Figure 3.3C clearly indicates that the tail-spearfishing mechanism remains active in the Sqe/Alc system, maintaining its role in facilitating enhanced Cl_2 and C=C double bond interactions at the interface. The reactivity at the surface is also governed by chlorine's mobility, which is examined through an analysis of interfacial diffusion dynamics. Following the procedure developed by Polley *et al.*,[26] and implemented in our previous work on the pure squalene system,[16] we use MD shooting trajectories of Cl_2 from the gas phase onto the liquid slab to constrain the friction profile across the interface, which allows us to quantify chlorine's diffusion constant. Full details for this analysis are available in the Supplementary Information Section S3. Briefly, the procedure constrains fit parameters to the functional form of the friction by comparing Fokker-Planck (FP) propagated dynamics to those obtained directly from the MD shooting trajectories. We find that the friction profile and FP dynamics obtained in Ref. [16] for the pure squalene system are nearly identical to those obtained here for the Sqe/Alc system (Figure 3.S4). The resulting friction profile across the interfacial region is shown in Figure 3.4.

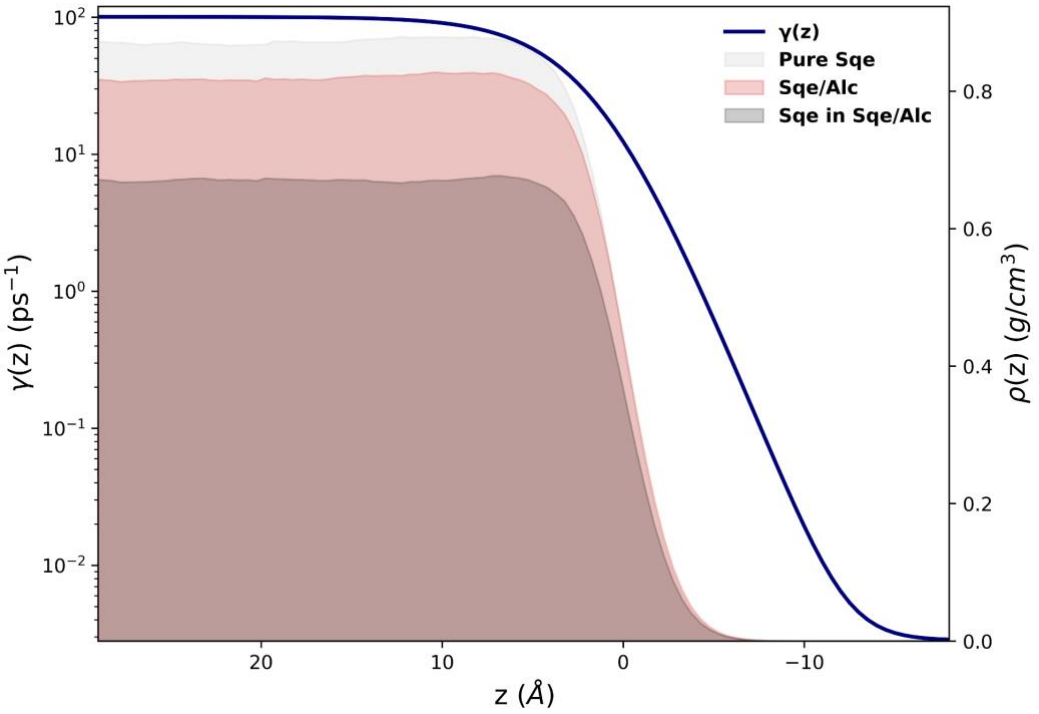

Figure 3.4. Position dependent friction profile along the z axis is shown in blue. Pure squalene slab density is shown as a shaded grey area. Sqe/Alc total slab density is shown as shaded red area, and the density of only the squalene molecules in Sqe/Alc is shown as shaded black area.

Figure 3.4 indicates that although the total density of the Sqe/Alc slab is slightly lower (~6%) than that of pure squalene, the overall friction profile is largely unchanged. The friction rises from the gas phase value well before the Gibbs dividing surface ($z = 0$) due to long-range dispersion interactions between chlorine and molecules in the liquid. The observed similarity of the friction profile between the pure and alcohol-containing system likely arises from the interplay of two opposing factors. A reduced bulk density in the mixed system would lead to decreased friction, whereas enhanced dispersion interactions between Cl and O atoms (relative to Cl and C) will increase friction. Altogether, the diffusion of chlorine, which is inversely proportional to the

friction (*i.e.,* the Einstein relation), is about an order magnitude faster at the Gibbs dividing surface and changes by about three orders of magnitude across the interfacial region. The contribution of faster chlorine diffusion to accelerating the interfacial reaction rate in pure squalene is expected to have a comparable effect in the Sqe/Alc mixture.

Thus, the addition of $C_{24}OH$ does not appear to significantly alter the mechanisms identified in the pure squalene system.[16] Accordingly, the interfacial reaction rate in the Sqe/Alc mixture is expected to be similarly accelerated by about two orders of magnitude relative to the bulk liquid due to increased encounter frequency.

Constructing a kinetic model to explain the experimental results shown in Figure 3.1, requires information on the changes in the Henry's law constant for partitioning of chlorine between gas, interface, and bulk across the temperature range examined in the aerosol experiments. The PMF for Cl_2 solvation across the temperature range examined in the aerosol experiments is shown in Figure 3.5.

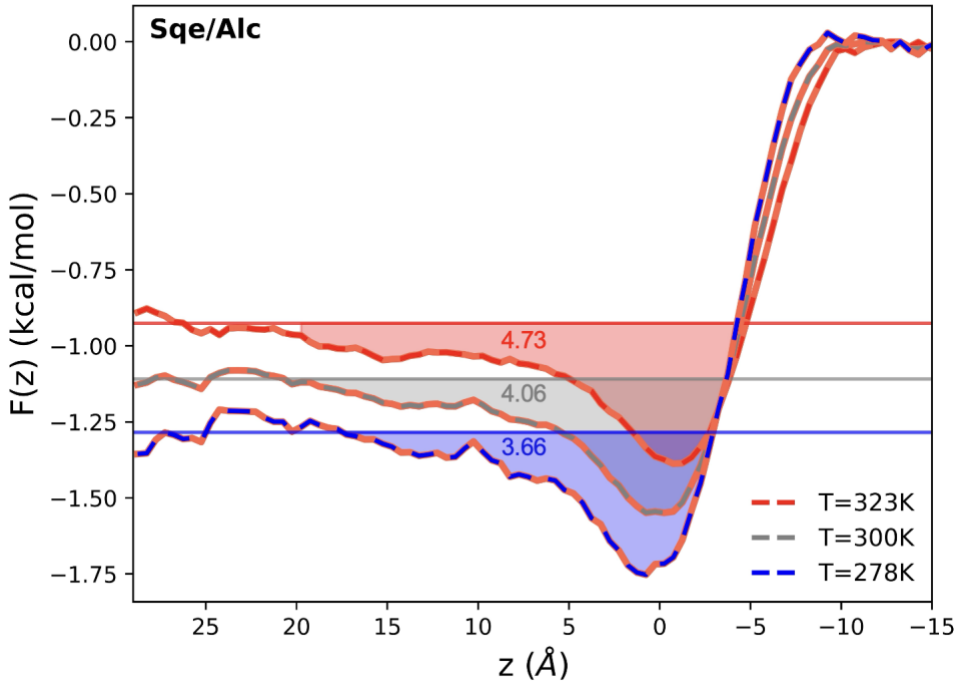

Figure 3.5. PMF for chlorine solvation in the Sqe/Alc system at the temperatures used in previous aerosol experiments: 278K (blue dash), 300K (grey dash), 323K (red dash). The integrated interfacial well area is shown as a shaded region with listed values in units of $\frac{\text{kcal}}{\text{mol}\text{Å}}$.

The PMF at 323K is computed using the same bias simulation windows applied to the room temperature PMF at 300K (Figure 3.2B). Alternatively, the PMF at 278 K was estimated via entropy decomposition, based on the temperature-scaled difference between the PMF at 300 K and 323 K. One key molecular detail that varies substantially between the pure and alcohol-mixed systems is the change in the interfacial solvation free energy profile with temperature. For Sqe/Alc, the total area of the interfacial region (see shaded regions of Fig. 3.5) decreases as the temperature drops. In contrast to the pure squalene system where this area increases as the temperature decreases (Ref. [16] and Figure 3.S5). One would typically expect that as temperature decreases,

reduced thermal energy makes it more likely for chlorine to remain at the interfacial free energy minimum, resulting in longer residence times at the surface. This behavior was observed in the pure squalene system. Instead, both the depth and width of the interfacial region in the alcohol mixed system increase with temperature. This counterintuitive observation is due to the presence of OH groups in the subsurface region, increasing the interfacial heterogeneity and changing the overall thermodynamics of interfacial solvation in this system.

Having constrained the necessary molecular inputs, such as the temperature dependent Henry's law constant for Cl_2, and interfacial well area changes with temperature for the Sqe/Alc, we can proceed to construct a kinetic model for the multiphase reactivity probed in the aerosol experiments. Since, to the best of our knowledge, there is no known rate constant for chlorination in $C_{24}OH$ or Sqe/$C_{24}OH$ mixtures, and considering the large variation in rate constants observed in Figure 3.S1, we avoid making an assumption for the bulk reaction rate constant. Unlike the pure squalene case, where the bulk rate could be reasonably estimated, this current analysis uses the kinetic model to explore how much interfacial acceleration is required to match the experimental data. Fitting the bulk reaction rate to the room-temperature data allows us to explore the degree of interfacial rate acceleration necessary to achieve reasonable agreement with experimental results. Complete kinetic model inputs are available in Table 3.S2 of the Supplementary Information.

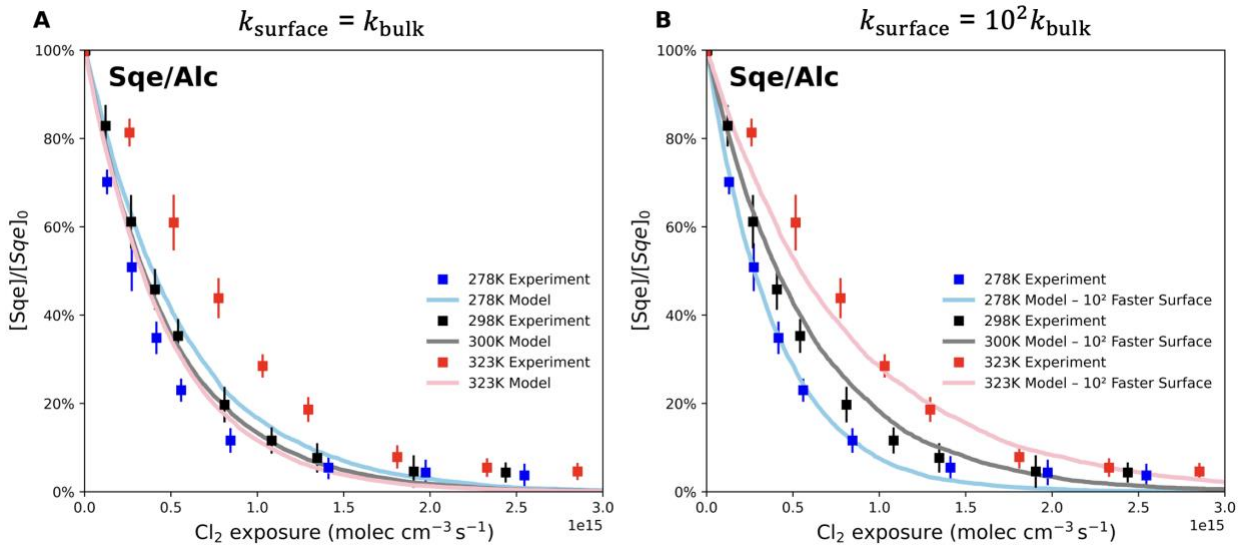

Figure 3.6. Kinetic model predictions for two scenarios: (A) a surface reaction rate that is equal to the bulk rate, and (B) a surface rate that is 100 times faster than the bulk. Experimental data and model predictions are shown for 278 K (blue), room temperature (black and gray), and 323 K (red). Model scenarios show that a faster surface rate that is two orders of magnitude faster than bulk compares well to the experimental results.

Figure 3.6 shows the comparison of the kinetic model predictions with the aerosol experimental results for two model scenarios: (Fig. 3.6A) fitting the bulk reaction rate to match the experimental kinetic trace at room temperature and assuming that surface and bulk reaction rates are equal (i.e., $k_{surface} = k_{bulk}$), and (Fig. 3.6B) assuming that the surface reaction rate is two orders of magnitude faster than bulk and fitting the bulk rate in $k_{surface} = 10^2 k_{bulk}$ to match the experimental results at room temperature when the surface rate is faster. There are no adjustable parameters in the kinetic model other than reaction rate constants. The first scenario predicts a temperature dependence opposite to what is observed experimentally. This arises from the

interplay between three factors: solubility, interfacial thickness, and bulk reaction rate. As expected for a bimolecular reaction, the bulk rate increases with temperature (the activation energy is assumed based on alkene chlorination in acetic acid – Figure 3.S8). Additionally, based on the analysis above, the interfacial thickness is also expected to increase with temperature. Together, these effects counteract the decrease in solvation with increasing temperature and result in a prediction that does not align with the experimental results. In contrast, the second scenario with the faster surface rate predicts faster reaction kinetics with decreasing temperature, which replicates the experimental trends.

Scenario B is supported by the analysis above, which predicts that a similar two orders of magnitude acceleration of the interfacial rate, is expected in the Sqe/Alc mixture. The resulting bulk rate at room temperature is determined to be $k = 2.0 \times 10^{-17}\mathrm{cm}^3\mathrm{molec}^{-1}\mathrm{s}^{-1}$, which is exactly one order of magnitude larger than the bulk rate for chlorination in pure squalene.[16] This increase is attributed to dielectric stabilization of charged or polarizable intermediates, as discussed above, which influences the overall bulk reaction rate by affecting both the pre-exponential factor and the activation energy. Examination of the compiled alkene chlorination rates as a function of solvent dielectric constant (Figure 3.S1) shows that the order of magnitude increase predicted by Scenario B is consistent with trends observed across solvents of increasing polarity. The corresponding surface rate, $k = 2.0 \times 10^{-15}\mathrm{cm}^3\mathrm{molec}^{-1}\mathrm{s}^{-1}$, is three orders of magnitude larger than that pure squalene bulk rate, underscoring the substantial catalytic effect that the alcohol mixed interface can exert on this reaction.

This kinetic model, combined with the observed increase in the interfacial well area with temperature, also explains the weaker temperature dependence of the mixture compared to pure squalene shown in Figure 3.1B. In the alcohol mixture, the interfacial thickness increases with temperature, which moderates the significance of the interface due to predicted changes in Henry's law partitioning and reduces the kinetic model divergence with temperature. Although the trend still predicts faster reaction at lower temperatures, it is less pronounced than in pure squalene, where the interfacial region widens upon cooling, further enhancing the surface contribution and accelerating the observed kinetics with decreasing temperature. Finally, if we accept Scenario B and that in both the pure and alcohol mixed system the interfacial rate is two orders of magnitude faster than bulk, we recover the kinetic trend in Figure 3.1A.

The structure of this work contrasts with our previous work on the pure squalene system.[16] In that case, we began with a well-constrained kinetic model that predicted the interfacial chlorination rate to be approximately 100 times faster than in the bulk. This prediction then motivated further analysis of simulation results to uncover the underlying mechanisms of interfacial acceleration. In the current study, we first confirmed that the two contributing mechanisms - enhanced chlorine diffusion at the surface and the tail-spearfishing effect - are expected to remain active in the in the Sqe/Alc mixed system. These findings, in turn, support the prediction emerging from a less-constrained kinetic model.

3.4. Conclusions

Understanding multiphase reactivity requires bridging experimental observations with molecular-level insight. In this work, we combined molecular simulations with kinetic modeling

to explore how the addition of long-chain alcohols alters the interfacial environment and the overall multiphase kinetics of squalene chlorination. While prior experimental work showed that alcohols accelerate the reaction without changing the mechanism, the molecular origin of this catalytic effect remained unclear. Our simulations reveal that, contrary to initial assumptions, the alcohol group in 2-decyl-1-tetradecanol is repelled from the interface and instead accumulates in a subsurface layer, which alters local solvation and density but leaves the interfacial orientation of squalene tails largely unchanged. As a result, the mechanisms we have identified in our previous work on the pure squalene system is preserved in the alcohol mixed system. Chlorine continues to diffuse more rapidly at the surface, and squalene double bonds that extend into the gas phase come in contact with chlorine at a higher probability. By recognizing that a similar two-order-of-magnitude acceleration in interfacial reactivity is likely to occurs in the mixed system, we are able to construct a kinetic model that captures the experimentally observed multiphase kinetics. This model predicts that the bulk reaction rate increases by approximately one order of magnitude relative to the pure system due to increased solvent polarity which likely stabilizes reaction intermediates.

Furthermore, our simulations provide a molecular-level explanation for the weaker inverse temperature dependence of the measured uptake coefficient observed in the alcohol-containing system. The increase in interfacial well area with temperature diminishes the surface contribution to reactivity at lower temperatures, thereby reducing the extent of the reversed temperature trend compared to that seen in pure squalene. The overall three orders of magnitude acceleration between the bulk rate in pure squalene and the surface rate in the squalene–alcohol mixture highlights the catalytic potential of liquid–vapor interfaces, where structural organization and interfacial dynamics promote reactivity beyond what is possible in homogeneous phases. Collectively, these results show how even small compositional shifts can preserve, amplify, or tune interfacial reactivity, offering a more nuanced view of how chemical complexity shapes reaction kinetics in multiphase systems, thus highlighting the potential to deliberately control interfacial structure and composition as a means to drive and optimize catalytic behavior.

3.5. Supporting Information

3.5. Section S1: Chlorine Solvation PMF Umbrella Sampling

The combination of spring constants used in umbrella sampling bias windows used to construct the potential of mean force (PMF) are shown in Table 3.S1.

Table 3.S1. Umbrella sampling bias windows details

$k\left(\frac{kcal}{mol\text{Å}^2}\right)$	Constrained Position in box $z_0(\text{Å})$	Constrained Position shifted to zero at Gibbs dividing surface (matching coordinates presented in the paper) $z_0(\text{Å})$	Simulation length per window
1	-47.5,-46.5,…,46.5,47.5 -35,-34,…,34,35	-17.5,-16.5,…,76.5,77.5 -5,-4,…,64,65	10ns
3	-47.5,-46.5,…,46.5,47.5 -35,-34,…,34,35	-17.5,-16.5,…,76.5,77.5 -5,-4,…,64,65	20ns
5	-40,-39.5,..,39.5,40	-10,-9.5,..,69.5,70	20ns
8	-30,-29.5,…,29.5,30	0,0.5,..,59.5,60	20ns

3.5. Section S2: Reaction Rates for Alkene Chlorination in Polar Solvents

Compilation of experimental reaction rates for chlorination of alkenes as a function the solvent dielectric constant is shown in Figure 3.S1. Rate constants are gathered from references [29–32], solvent dielectric constants are taken from NIST.[34]

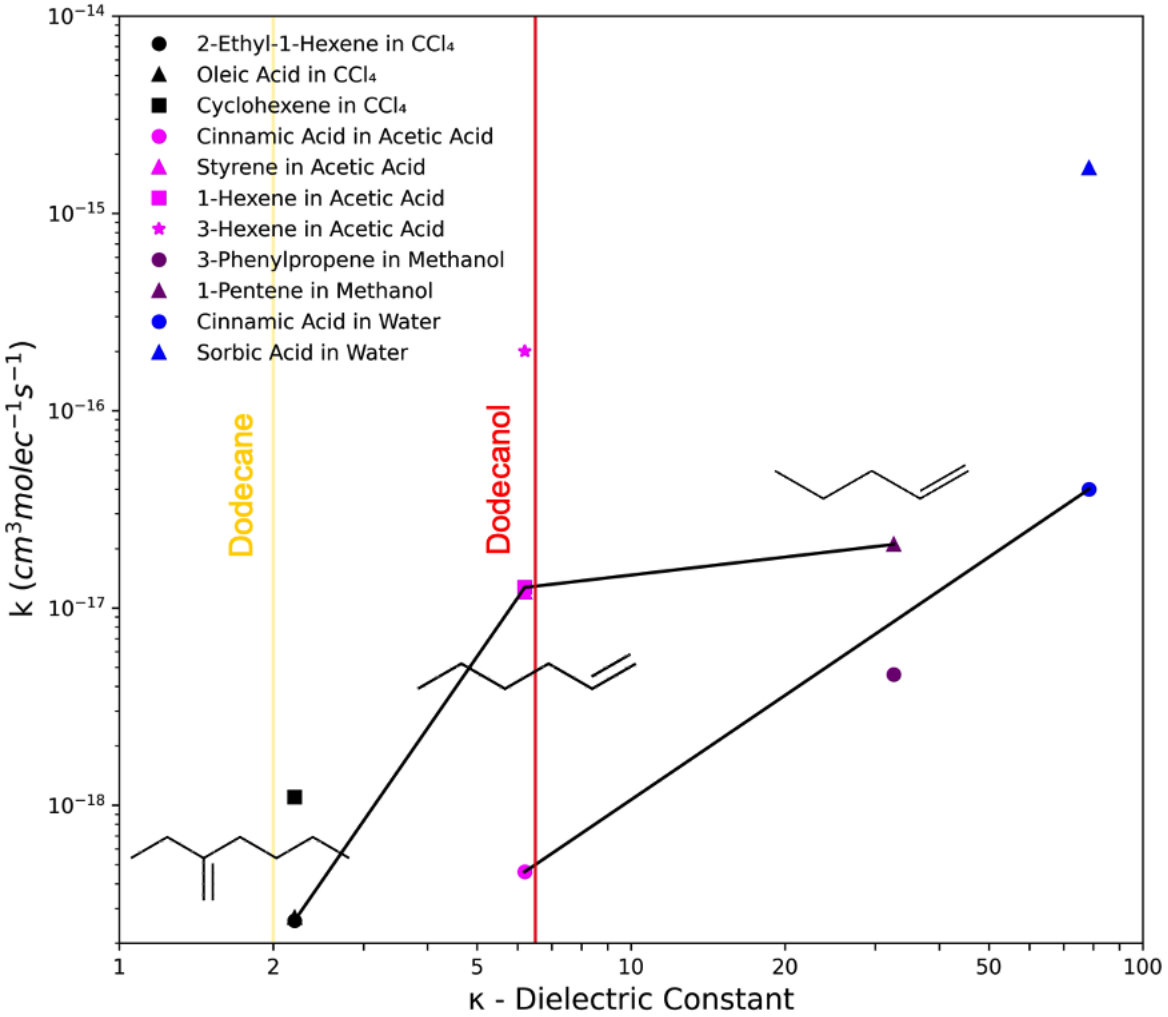

Figure 3.S1. Reaction rate constants for chlorination of various alkenes plotted as a function of solvent dielectric constant on a log-log scale. Solvents are color coded: CCl_4 is shown in black, acetic acid shown in pink, methanol is shown in purple, and water is shown in blue. Black lines are shown to connect similar/identical alkenes subject to chlorination. Structures are shown for 2-ethyl-1-hexane (black circle), 1-hexene (pink square), 1-pentene (purple triangle). Two horizontal lines mark the dielectric constant of dodecane and dodecanol.

Examination of Figure 3.S1 offers multiple insights. First, the reaction rate of a single alkene or similar compound is highly sensitive to the solvent polarity and can change by over two orders of magnitude as the solvent dielectric constant increases. Second, even within the same solvent, there is a large variation of rate constants depending on the alkene identity. Structure-reactivity relationship for chlorination is expected to follow stability of carbocation or radical reaction intermediate, as such it is highly dependent on the functional groups adjacent to the double bond. Thus, it is difficult to make an assumption from the available data of what the bulk rate of

squalene chlorination in $C_{24}OH$ or in a mixture of squalene and $C_{24}OH$ would be, but the two horizontal lines provide a bracket of non-polar solvent (Dodecane) compared to an alcohol with a carbon chain (dodecanol). A mixture of long carbon chain $C_{24}OH$ and squalene is expected to have a dielectric constant smaller than dodecanol. We were unable to find a literature reference for alkene chlorination in a solvent with a dielectric constant between that of carbon tetrachloride and acetic acid. However, the observed trend shown as a black line, based on 2-ethyl-1-hexene (black circle), 1-hexene (pink square), and 1-pentene (purple triangle) - suggests a stronger rate acceleration when moving from a non-polar to a slightly polar solvent, compared to moving between two polar solvents, even when the latter transition involves a larger change in dielectric constant. This claim is further strengthened by the fact that 2-ethyl-1-hexane is expected to react faster than 1-hexene or 1-pentene since it has a methyl group adjacent to the double bond instead of hydrogen. Hence, a true line connecting a C5-C6 terminal alkene in CCl_4 is expected to be plotted as an even lower rate constant.

3.5. Section S3: MD Shooting Trajectories and Position Dependent Friction

To characterize the diffusive behavior of Cl_2 near the interface, we followed the procedure by Polley et at. detailed in Ref [26]. Briefly, chlorine's position was initialized in the gas phase as a Gaussian centered at $z = -15$Å (45Å in box coordinates) with a thermally sampled velocity towards the Sqe/Alc slab. Chlorine's center of mass position and velocity were recorded for 30ps in the z direction, to constrain the friction profile of a Cl_2 molecule in the interfacial region. The velocity and position are binned to construct a time dependent position-velocity probability distribution of Cl_2 approaching the interfacial minimum of the PMF. The position probability distribution is shown in Fig. 3.S2.

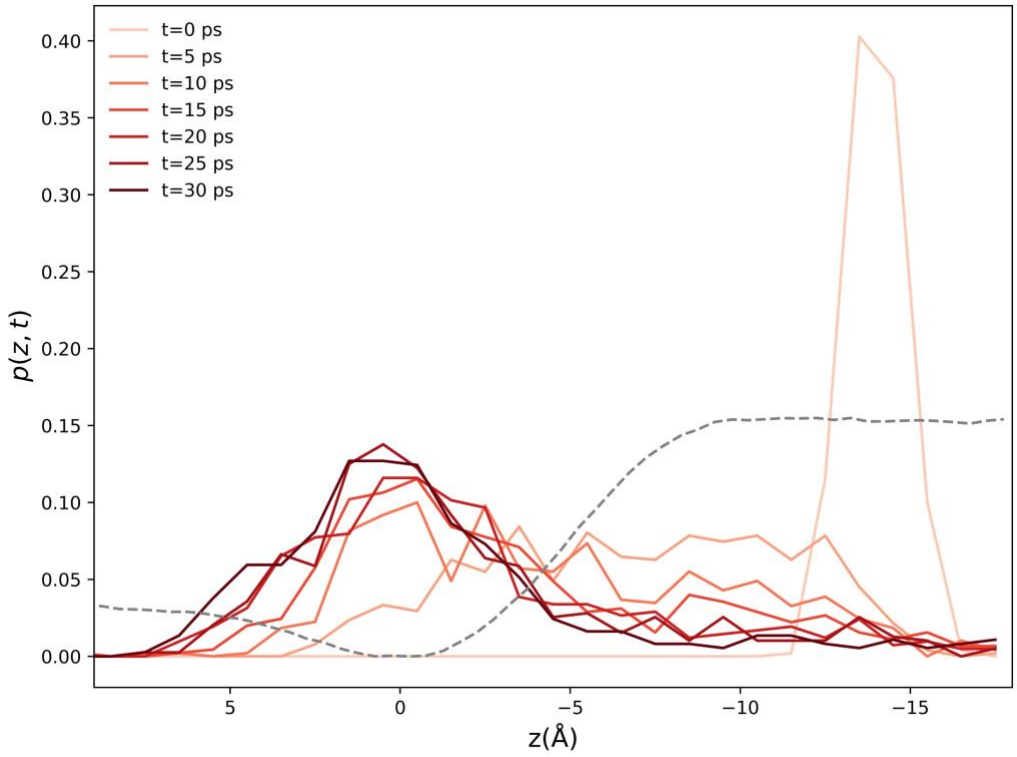

Figure 3.S2. Position probability distribution, p(z, t), of chlorine's MD shooting trajectories for the Sqe/Alc mixture. The initial position is a gaussian centered around $z = -15$Å with initial velocity pointed towards the slab. Chlorine's solvation PMF is shown with a dashed line and time traces are shown in red with darker colors corresponding to later time.

After 30ps trajectories tend to accumulate towards the PMF minima with slow solvation into the bulk. At early time, when chlorine is diffusing in the gas phase ($t = 0 \rightarrow t = 5$ ps), it does so very quickly as it experiences little friction. As it approaches the liquid slab, chlorine's position changes very slightly from $t = 15ps \rightarrow t = 30ps$, as it starts to experience increasing friction approaching the molecules at the interface. This evolving position distribution captures the frictional resistance encountered by Cl_2 as it traverses from the gas phase into the liquid phase.

Bulk diffusivities were computed from collecting simulation trajectories limited to the bulk region ($-10 < z < 10$ Å) out of a 150ns non-biased simulation. Using mean-squared displacement analysis (Figure 3.S3), we can calculate the diffusion constant for chlorine in the bulk (Eq. 5 main text).

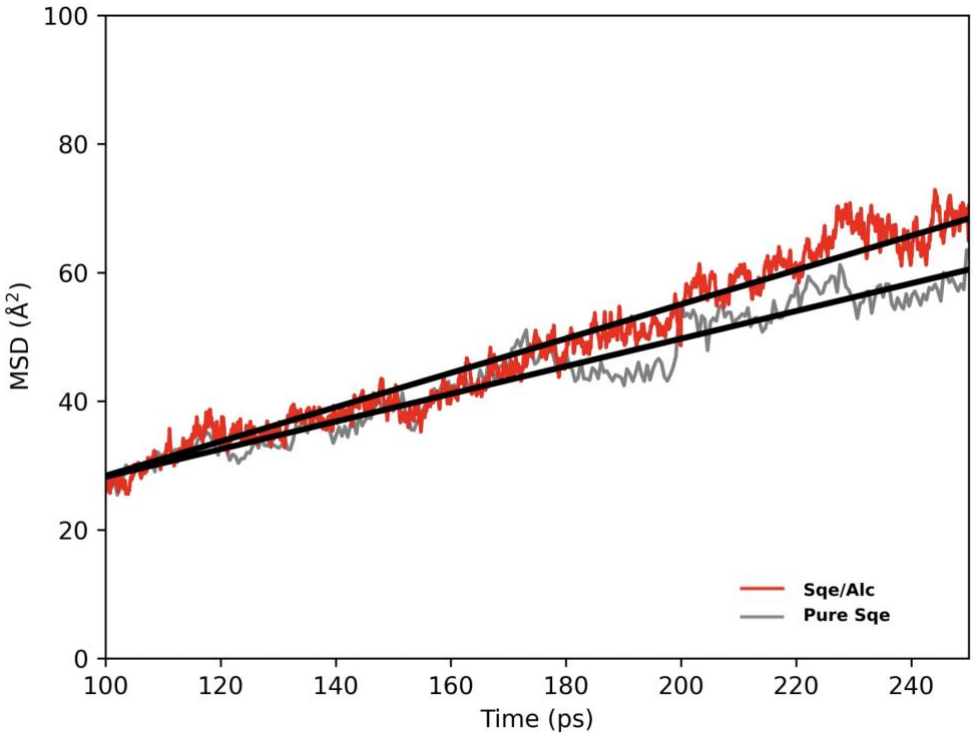

Figure 3.S3. Mean squared displacement analysis for Sqe/Alc (shown in red) and pure squalene system (shown in grey). The diffusion constant is extracted from the slope using Eq. 5 in the main text.

The bulk diffusion constant for chlorine calculated from the slope for pure squalene is $D_{Sqe} = 3.49 \pm 0.24 \times 10^{-6} \frac{cm^2}{s}$, and the of Sqe/Alc is $D_{Sqe/Alc} = 4.42 \pm 0.13 \times 10^{-6} \frac{cm^2}{s}$. The diffusion of chlorine in Sqe/Alc is slightly faster than that of the pure system.

The second stage of the process of constraining the friction profile experienced by chlorine in the interfacial region includes propagating the Fokker-Planck(FP) equation of motion,

$$\frac{\partial p(z,v,t)}{\partial t} = -v\frac{\partial p}{\partial z} + \frac{\partial}{\partial v}\left[\frac{\partial_z F(z)}{m} + \gamma(z)v\right]p + \frac{k_B T\gamma(z)}{m}\frac{\partial^2 p}{\partial v^2}, \tag{3.S1}$$

where $F(z)$ is the potential of mean force, $\gamma(z)$ is the position-dependent friction experienced by the particle of mass m, and v is velocity. The friction profile is described by a smoothly varying hyperbolic tangent function,

$$\gamma(z) = \left(\gamma_{\mathrm{l}} - \gamma_{\mathrm{g}}\right)\left(\tanh\frac{(w(s-z))}{2} + \frac{1}{2}\right)^n + \gamma_{\mathrm{g}}, \tag{3.S2}$$

where γ_{l} is the friction of the bulk liquid, γ_{g} is the friction in the gas phase, and s, w, and n are the fitting parameters controlling the transition region between the gas and bulk friction limits. The friction in the bulk and gas regions is determined from the diffusion coefficients using the Einstein relation,

$$\gamma_{\mathrm{l/g}} = \frac{k_{\mathrm{B}}T}{mD_{\mathrm{l/g}}}, \tag{3.S3}$$

where k_B is Boltzmann's constant, T is temperature, and $D_{\mathrm{l/g}}$ is the liquid or gas diffusion constant, respectively. The FP equation is subsequently propagated using a variety of fit parameters s,w, and n, until the probability distribution compares well to the MD shooting trajectory shown in Figure 3.S2.

When compared to prior analysis of chlorine diffusion at the pure squalene interface,[16] there is overlap between the results obtained for the pure system and that of the alcohol mixed system. While it is interesting to examine how the small changes in the observed diffusion in the interfacial and bulk regions affect the friction profile of this system. A comparison between the two systems and the FP propagated dynamics using the converged optimal friction $\gamma(z)$ of the pure squalene is shown in Figure 3.S4.

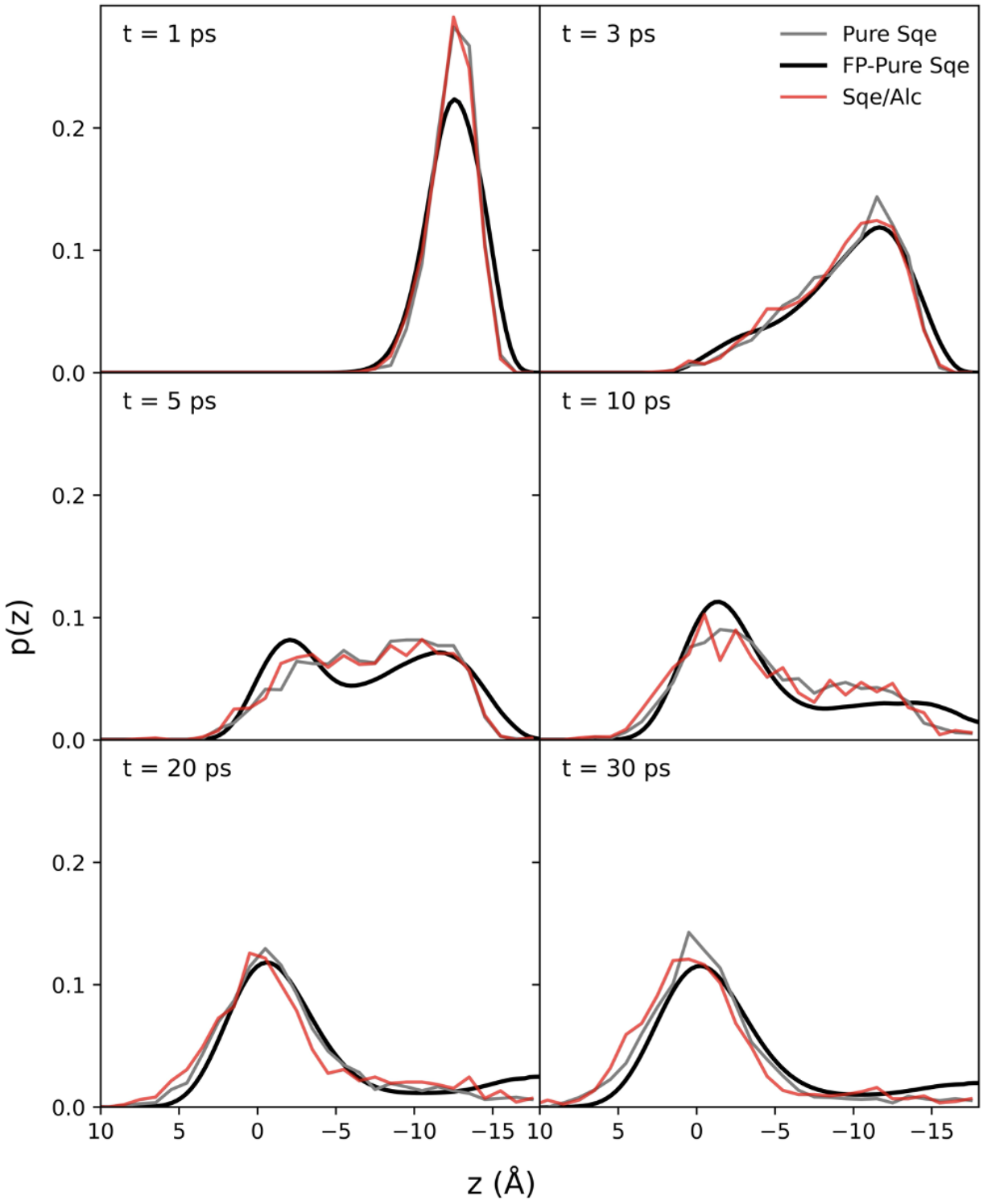

Figure 3.S4. Comparison of the position probability distribution between Fokker-Planck (FP) propagated dynamics with the converged friction function for the pure squalene system shown in black and the shooting trajectories from MD shown in grey for the pure system and in red of the Sqe/Alc.

The Fokker-Planck propagated dynamics with the optimal friction parameter fit of pure squalene is in reasonable agreement with the MD shooting trajectories for both pure squalene and the Sqe/Alc system.

3.5. Section S4: Interfacial Area in the Pure Squalene System

The temperature dependent PMF for the pure squalene system for the temperatures examined in the aerosol experiments is computed using WHAM averaged enthalpy and shown in Figure 3.S5A. The comparison between the WHAM calculated average estimate and the explicit simulation for T=323K is shown if Figure 3.S5B, both reproduced from ref [16].

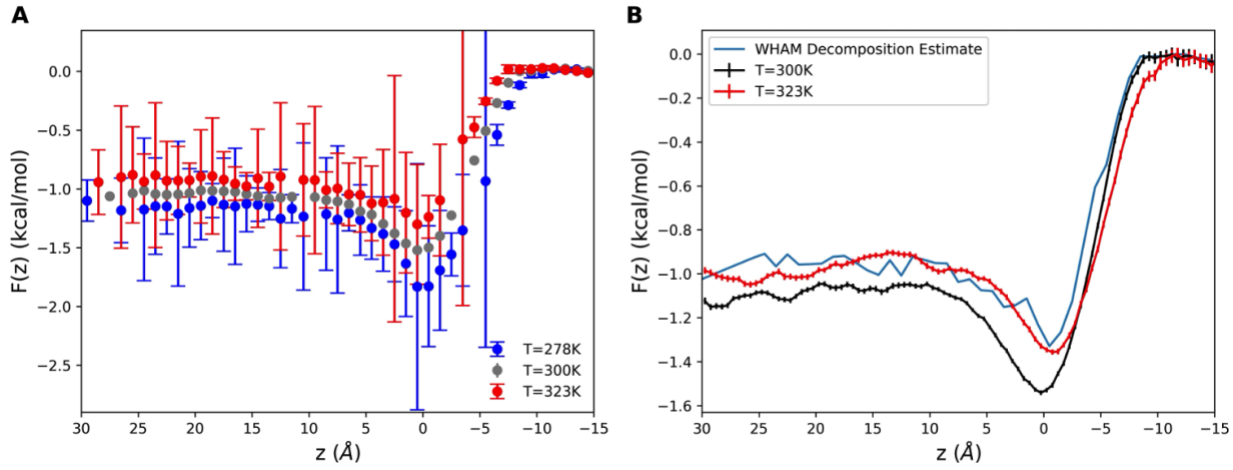

Figure 3.S5. (A) PMF as function of the temperatures used in previous in aerosol experiments: 278K (blue), 300K (grey), and 323K (red), error bars represent standard error. (B) Explicitly calculated PMF from umbrella sampling at 323K (red) and 300K (black) with the WHAM decomposition estimate for 323K (blue line). Rep. from ref [16].

Both the WHAM averaged decomposition estimate of the temperature dependent PMF, and the direct comparison of explicitly calculated PMFs at 300 K and 323 K reveal the same trend: the interfacial well area- both depth and width increases as temperature decreases in pure squalene.

If the PMF were independent of temperature, a decrease in temperature would increase the probability of finding chlorine at the interface, as the system would more frequently occupy the PMF minimum. Conversely, higher temperatures would reduce this interfacial probability, leading to a diminished contribution from surface reactions to the overall uptake. In the case of pure squalene, this effect is amplified by the fact that the interfacial well in the PMF becomes both shallower and narrower with increasing temperature, further decreasing the likelihood of chlorine being present at the interface and reducing the interfacial contribution. In contrast, for the Sqe/Alc mixture, the PMF well becomes deeper and broader as temperature increases, partially offsetting the expected decrease in interfacial occupancy. As a result, the contribution of interfacial reactions to the total uptake remains more stable across temperatures, and the reversed temperature dependence observed experimentally is noticeably weaker in the mixed system compared to pure squalene.

3.5. Section S5: Kinetic Model Details

The kinetic model for 80% squalene and 20% $C_{24}OH$ (by mole fraction) is implemented in Kinetiscope, [27] an open-source stochastic simulator that models reaction–diffusion processes via probability-weighted random walks. The simulation scheme closely follows the framework by

Willis and Wilson,[28] which describes an aerosol particle as comprised of two reaction compartments: surface and bulk. The kinetic model built for the Sqe/Alc system is similar to the one described in our previous work on squalene chlorination in the pure squalene system (Section S4 in SI ref [16] and Figure 3.S6 here). To preserve the correct surface-to-volume scaling for a spherical particle, the bulk compartment height is set to a/3 (where a is the aerosol or particle radius), and the surface compartment height is set to the interfacial thickness that is directly constrained from the temperature dependent PMF. The compartments are assumed to be internally well-mixed, and molecules diffuse between compartments by Fick's Law. To calculate volumetric concentration, the length and width of both compartments is set to 1 nm. These dimensions have been shown to not influence simulation results. [28]

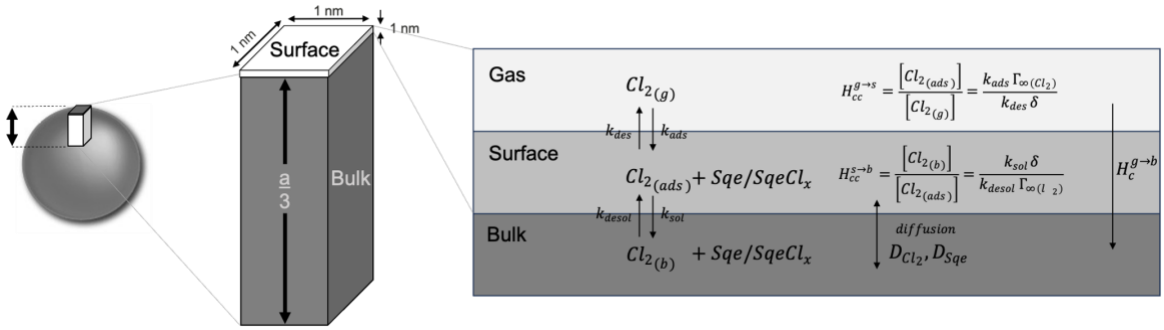

Figure 3.S6. Framework for kinetic modeling. Simulation preserves surface area to volume ratio of a sphere with surface compartment that is 1nm thick and bulk compartment with height of a/3. Three kinetic regions: gas, surface ,and bulk, maintain concentrations through coupled equilibrium determined by Henry's law coefficients calculated from MD. Surface and bulk species can react with squalene or diffuse between compartments. Maximum surface concentration $\Gamma_{\infty(Cl_2)}$ (from chlorine molecular size) and interfacial thickness δ determines the concentration of surface sites. (reproduced from Figure 3.S3 in ref [16])

The interfacial thickness δ is calculated based on linear scaling of the area of the interfacial well area. Figure 3.S7 shows the comparison between the pure squalene and Sqe/Alc systems.

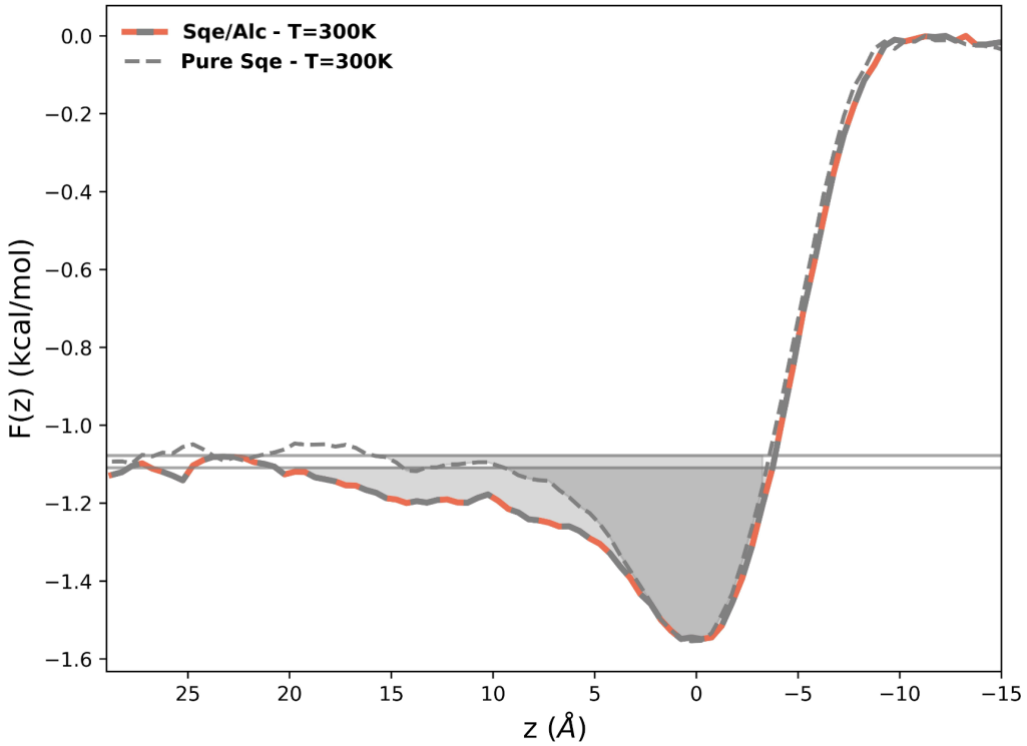

Figure 3.S7. Comparison of the interfacial well area in the Sqe/Alc vs. pure squalene.

The total area of the interfacial well is calculated to be $4.06\frac{kcal}{mol\text{Å}}$ in Sqe/Alc and $3.35\frac{kcal}{mol\text{Å}}$ for pure squalene. Scaling based on the interfacial thickness used in the pure squalene kinetic model taken from C=C density profile of $\delta_{Pure\ Sqe-300K} = 1.3nm$ the interfacial thickness calculated for the Sqe/Alc mixture is $\delta_{Sqe/Alc-300K} = 1.58nm$. Temperature dependence of the interfacial thickness is computed from the linear scaling of the interfacial areas shown in Figure 3.5 in the main text as $A_{interface_{Sqe/Alc-323K}} = 4.73\frac{kcal}{mol\text{Å}}$ and $A_{interface_{Sqe/Alc-278K}} = 3.66\frac{kcal}{mol\text{Å}}$, corresponding to $\delta_{Sqe/Alc-323K} = 1.84nm$ and $\delta_{Sqe/Alc-278K} = 1.42nm$.

The scheme features three kinetic regions: gas, surface, and bulk. Chlorine concentrations in each region are governed by a dimensionless Henry's law constant (H_{cc}) computed from the solvation free energy difference obtained by the Cl_2 PMF described above,

$$H_{cc}^{x\to y} = e^{-\frac{\Delta G_{x\to y}}{RT}}. \tag{3.S4}$$

$\Delta G_{x\to y}$ is the free energy difference of Cl_2 between different regions (e.g. x = gas, y = bulk). The gas to surface Henry's law constant is,

$$H_{cc}^{g\to s} = \frac{\left[Cl_{2(ads)}\right]}{\left[Cl_{2(g)}\right]} = \frac{k_{ads}\Gamma_{\infty(Cl_2)}}{k_{des}\delta}, \tag{3.S5}$$

where k_{ads} and k_{des} are rate coefficients that describe the adsorption and desorption of Cl_2 to the interface. $\Gamma_{\infty(Cl_2)}$ is the maximum surface concentration, and δ is the interfacial thickness. Surface sites are represented as volumetric concentrations ($\frac{\Gamma_{\infty(Cl_2)}}{\delta}$). $\Gamma_{\infty(Cl_2)}$ is computed from the molecular area of Cl_2 (19.1Å – taken from force field parameters for Cl_2). k_{ads} is set to the collision frequency of chlorine gas, which assumes a sticking probability of 1,

$$k_{ads} = \frac{\bar{c}A}{4}, \tag{3.S6}$$

where $\bar{c}$ is the mean speed of chlorine gas (299 m/s at 300K) and A is the area of the surface compartment. k_{des} is computed from Eq. (3.S5) using k_{ads} and $H_{cc}^{g\to s}$ obtained in the simulations. Surface to bulk partitioning is described by a second Henry's law constant,

$$H_{cc}^{s\to b} = \frac{\left[Cl_{2(b)}\right]}{\left[Cl_{2(ads)}\right]} = \frac{k_{sol}\delta}{k_{desol}\Gamma_{\infty(Cl_2)}}, \tag{3.S7}$$

where the solvation rate (k_{sol}) is computed from k_{des} and the mass accommodation coefficient obtained directly from simulations,

$$\alpha = \frac{k_{sol}}{k_{sol}+k_{des}} \to k_{sol} = \frac{\alpha k_{des}}{1-\alpha} \tag{3.S8}$$

From k_{sol} and $H_{cc}^{s\to b}$, k_{desol} is determined using Eq. (3.S7). All model parameters other than the reaction rate constant are directly constrained from our MD simulations. Since to the best of our knowledge there is no known rate constant for squalene chlorination in $C_{24}OH$ or its mixtures with squalene—and the wide variability observed in Figure 3.S1—we do not assume a bulk reaction rate. The kinetic model is used here to estimate how much the interfacial rate must be accelerated to reproduce the experimental data. Fitting the bulk rate to room-temperature measurements allows us to quantify the required surface enhancement.

The activation energy observed in more polar solvents than CCl_4 is higher. Considering that the kinetics change substantially from the pure squalene case it seems appropriate to correct the assumption for the magnitude of the activation energy or the change in the bulk rate with temperature, to account for a more polar solvent. Figure 3. S8 is showing the reaction rate constant as function of temperature for chlorination of m-chloro-styrene in acetic acid from ref [30].

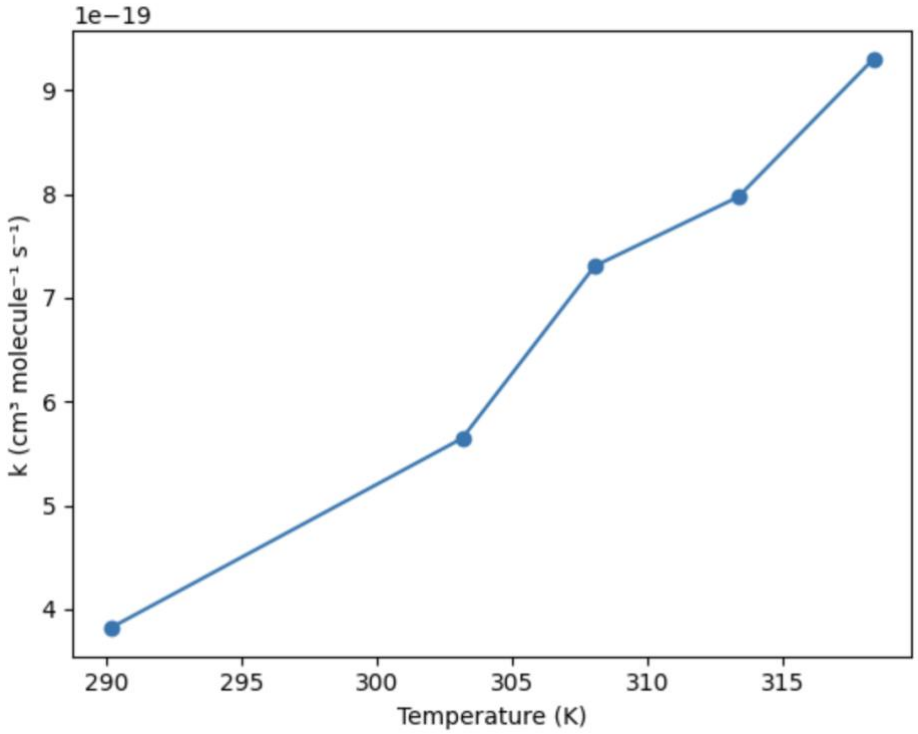

Figure 3.S8. Reaction rate constant as function of temperature for m-chloro-styrene in acetic acid, data points are taken from Ref [30]. Lines are a guide for the eye.

The activation energy calculated from Figure 3.S8 is 5.86 kcal/mol, which is 3 times higher than the estimate we used for the pure squalene from chlorination oleic acid in CCl_4.[16,29]

A complete list of model parameters is given in the Table 3.S2. The kinetic formulation is adapted from the model we previously developed for the pure squalene system,[16] with rates and parameters modified to reflect the properties of the alcohol-mixed system.

Table 3.S2. Elementary reaction steps, rate and diffusion coefficients used in the Kinetiscope simulations. Quantities derived directly from MD simulations are shown in **Bold**. Reaction steps that occur at the surface compartment are labeled with S, diffusion steps between the surface and bulk compartment are labeled with D, and reaction steps in the bulk are labeled with B.

#	Reaction	Rate Coefficient			Notes
		278K	300K	323K	
S1	$\text{site}_{Cl_2} \underset{k_{des}}{\overset{k_{ads}}{\rightleftarrows}} Cl_{2(ads)}$	$k_{ads} = 1.77 \times 10^4 s^{-1}$ $k_{des} = 2.33 \times 10^{10} s^{-1}$ $\boldsymbol{H_{cc}^{g\to s} = 22.98}$ $\boldsymbol{H_{cc}^{s\to b} = 0.4564}$ $\boldsymbol{H_{cc}^{g\to b} = 10.49}$ $\boldsymbol{\delta = 1.42nm}$ ***calculated from scaling the integrated area of the interfacial well in Sqe/Alc at T=278K vs room temperature thickness of $\boldsymbol{\delta = 1.58nm}$ (Figure 3.5 – main text).**	$k_{ads} = 1.84 \times 10^4 s^{-1}$ $k_{des} = 4.77 \times 10^{10} s^{-1}$ $\boldsymbol{H_{cc}^{g\to s} = 12.96}$ $\boldsymbol{H_{cc}^{s\to b} = 0.4807}$ $\boldsymbol{H_{cc}^{g\to b} = 6.23}$ $\boldsymbol{\delta = 1.58nm}$ ***calculated from scaling the integrated area of the interfacial well in the pure squalene vs Sqe/Alc system (Figure 3.S7).**	$k_{ads} = 1.91 \times 10^4 s^{-1}$ $k_{des} = 6.68 \times 10^{10} s^{-1}$ $\boldsymbol{H_{cc}^{g\to s} = 8.39}$ $\boldsymbol{H_{cc}^{s\to b} = 0.4648}$ $\boldsymbol{H_{cc}^{g\to b} = 3.90}$ $\boldsymbol{\delta = 1.84nm}$ ***calculated from scaling the integrated area of the interfacial well in Sqe/Alc at T=323K vs room temperature thickness of $\boldsymbol{\delta = 1.58nm}$ (Figure 3.5 – main text).**	$k_{ads} = \frac{\bar{c}A}{4}$, where mean speed of Cl_2 is calculated from $\sqrt{\frac{8RT}{\pi M}}$. k_{ads}implemented here in one step following a pseudo first-order rate with $[Cl_2] = 10ppm$ matching the experimental conditions, no sensitivity is observed in the model for concentrations within an order of magnitude difference (1-100ppm) $k_{des} = \frac{k_{ads}\Gamma_{\infty(Cl_2)}}{H_{cc}^{g\to s}\delta} = \frac{k_{ads}[\text{site}_{Cl_2}]}{H_{cc}^{g\to s}}$ $\boldsymbol{molecular\ area = 19.13}$Å $[\text{site}_{Cl_2}] = \frac{V_{sur}}{molecular\ area}$
S2	$Cl_{2(ads)} \underset{k_{desol}}{\overset{k_{sol}}{\rightleftarrows}} Cl_{2(b)} + \text{site}_{Cl_2}$	$k_{sol} = 3.17 \times 10^{10} s^{-1}$ $k_{desol} = 9.36 \times 10^{-12} cm^3 molec^{-1} s^{-1}$ $\boldsymbol{\alpha = 0.577}$* ***estimated from bulk solvation energy gap to increase from room temperature according to surface to bulk solvation energy.**	$k_{sol} = 3.34 \times 10^{10} s^{-1}$ $k_{desol} = 8.41 \times 10^{-12} cm^3 molec^{-1} s^{-1}$ $\boldsymbol{\alpha = 0.412}$* ***calculated from branching of trajectories starting at the interface**	$k_{sol} = 2.69 \times 10^{10} s^{-1}$ $k_{desol} = 8.01 \times 10^{-12} cm^3 molec^{-1} s^{-1}$ $\boldsymbol{\alpha = 0.287}$* *** calculated from branching of trajectories starting at the interface**	$\alpha = \frac{k_{sol}}{k_{sol} + k_{des}}$ $k_{sol} = \frac{\alpha k_{des}}{1-\alpha}$ $k_{desol} = \frac{k_{sol}\delta}{H_{cc}^{s\to b}\Gamma_{\infty(Cl_2)}} = \frac{k_{sol}}{H_{cc}^{s\to b}[\text{site}_{Cl_2}]}$
S3	$Cl_{2(ads)} + Sqe \rightarrow SqeCl_2 + \text{site}_{Cl_2}$	Surface reaction rate is set to be equal to bulk rate (reaction B1) or set uniformly (independent of temperature) to be larger by X amount from B1 rate at room temperature.			$[sqe] = 1 \times 10^{21} molec/cm^3$ from squalene density 0.858 g/cm^3 and 80% .mol fraction in aerosol
S4	$Cl_{2(ads)} + SqeCl_2 \rightarrow SqeCl_4 + \text{site}_{Cl_2}$	Zeng et al.[12] found that this reaction appears to be following a sequential mechanism where chlorine adds across double bonds for already chlorinated products. We assume these reactions proceed with the same rate as the initial oxidation rate S3. No sensitivity is observed for the rates of sequential chlorination since in nm scale droplets chlorine's concentration is in a well-mixed regime.			
S5	$Cl_{2(ads)} + SqeCl_4 \rightarrow SqeCl_6 + \text{site}_{Cl_2}$	"			
S6	$Cl_{2(ads)} + SqeCl_6 \rightarrow SqeCl_8 + \text{site}_{Cl_2}$	"			
S7	$Cl_{2(ads)} + SqeCl_8 \rightarrow SqeCl_{10} + \text{site}_{Cl_2}$	"			
S8	$Cl_{2(ads)} + SqeCl_{10} \rightarrow SqeCl_{12} + \text{site}_{Cl_2}$	"			
D1	$Cl_{2(b)}$	Assumed same as 300K	$\boldsymbol{D_{Cl_2} = 4.42 \times 10^{-6} cm^2 s^{-1}}$*	Assumed same as 300K	Simulation is insensitive to the exact

			***calculated directly from mean squared displacement analysis in the bulk region**		diffusion coefficient as long as it is larger than the compartment size, since we are simulating nm scale droplets no sensitivity is observed
D2	$Sqe/SqeCl_x$	Assumed same as 300K	$\boldsymbol{D_{Sqe/SqeCl_x} = 1 \times 10^{-6} cm^2 s^{-1}}$* ***calculated directly from mean squared displacement analysis in the bulk region**	Assumed same as 300K	"
B1	$Cl_{2(b)} + Sqe \rightarrow SqeCl_2$	When $k_{\text{surface}} = k_{\text{bulk}}$: $k = 1.8 \times 10^{-16} cm^3 molec^{-1} s^{-1}$ When $k_{\text{surface}} = 10^2 k_{\text{bulk}}$: $k = 9.2 \times 10^{-18} cm^3 molec^{-1} s^{-1}$	When $k_{\text{surface}} = k_{\text{bulk}}$: $k = 4 \times 10^{-16} cm^3 molec^{-1} s^{-1}$ When $k_{\text{surface}} = 10^2 k_{\text{bulk}}$: $k = 2 \times 10^{-17} cm^3 molec^{-1} s^{-1}$	When $k_{\text{surface}} = k_{\text{bulk}}$: $k = 8 \times 10^{-16} cm^3 molec^{-1} s^{-1}$ When $k_{\text{surface}} = 10^2 k_{\text{bulk}}$: $k = 4 \times 10^{-17} cm^3 molec^{-1} s^{-1}$	Activation energy of 5.86 kcal/mol is estimated from chlorination of m-chloro-styrene in acetic acid (Figure 3.S8)
B2	$Cl_{2(b)} + SqeCl_2 \rightarrow SqeCl_4$	"	"	"	Subsequent reactions assumed to proceed with the same rate as B1
B3	$Cl_{2(b)} + SqeCl_4 \rightarrow SqeCl_6$	"	"	"	"
B4	$Cl_{2(b)} + SqeCl_6 \rightarrow SqeCl_8$	"	"	"	"
B5	$Cl_{2(b)} + SqeCl_8 \rightarrow SqeCl_{10}$	"	"	"	"
B6	$Cl_{2(b)} + SqeCl_{10} \rightarrow SqeCl_{12}$	"	"	"	"

3.6. References

(1) Ruiz-Lopez, M. F.; Francisco, J. S.; Martins-Costa, M. T. C.; Anglada, J. M. Molecular Reactions at Aqueous Interfaces. *Nat. Rev. Chem.* **2020**, *4* (9), 459–475. https://doi.org/10.1038/s41570-020-0203-2.

(2) Wei, Z.; Li, Y.; Cooks, R. G.; Yan, X. Accelerated Reaction Kinetics in Microdroplets: Overview and Recent Developments. *Annu. Rev. Phys. Chem.* **2020**, *71* (Volume 71, 2020), 31–51. https://doi.org/10.1146/annurev-physchem-121319-110654.

(3) Ahmed, M.; Blum, M.; Crumlin, E. J.; Geissler, P. L.; Head-Gordon, T.; Limmer, D. T.; Mandadapu, K. K.; Saykally, R. J.; Wilson, K. R. Molecular Properties and Chemical Transformations Near Interfaces. *J. Phys. Chem. B* **2021**, *125* (32), 9037–9051. https://doi.org/10.1021/acs.jpcb.1c03756.

(4) Knipping, E. M.; Lakin, M. J.; Foster, K. L.; Jungwirth, P.; Tobias, D. J.; Gerber, R. B.; Dabdub, D.; Finlayson-Pitts, B. J. Experiments and Simulations of Ion-Enhanced Interfacial Chemistry on Aqueous NaCl Aerosols. *Science* **2000**, *288* (5464), 301–306. https://doi.org/10.1126/science.288.5464.301.

(5) Jang, M.; Czoschke, N. M.; Lee, S.; Kamens, R. M. Heterogeneous Atmospheric Aerosol Production by Acid-Catalyzed Particle-Phase Reactions. *Science* **2002**, *298* (5594), 814–817. https://doi.org/10.1126/science.1075798.

(6) Kumar, M.; Trabelsi, T.; Gómez Martín, J. C.; Saiz-Lopez, A.; Francisco, J. S. HIOx–IONO2 Dynamics at the Air–Water Interface: Revealing the Existence of a Halogen Bond at the Atmospheric Aerosol Surface. *J. Am. Chem. Soc.* **2020**, *142* (28), 12467–12477. https://doi.org/10.1021/jacs.0c05232.

(7) Kumar, M.; Zhong, J.; Zeng, X. C.; Francisco, J. S. Reaction of Criegee Intermediate with Nitric Acid at the Air–Water Interface. *J. Am. Chem. Soc.* **2018**, *140* (14), 4913–4921. https://doi.org/10.1021/jacs.8b01191.

(8) Hoehn, R. D.; Carignano, M. A.; Kais, S.; Zhu, C.; Zhong, J.; Zeng, X. C.; Francisco, J. S.; Gladich, I. Hydrogen Bonding and Orientation Effects on the Accommodation of Methylamine at the Air-Water Interface. *J. Chem. Phys.* **2016**, *144* (21), 214701. https://doi.org/10.1063/1.4950951.

(9) Galib, M.; Limmer, D. T. Reactive Uptake of N2O5 by Atmospheric Aerosol Is Dominated by Interfacial Processes. *Science* **2021**, *371* (6532), 921–925. https://doi.org/10.1126/science.abd7716.

(10) Moon, S.; Limmer, D. T. Enhanced ClNO2 Formation at the Interface of Sea-Salt Aerosol. *J. Phys. Chem. Lett.* **2024**, *15* (37), 9466–9473. https://doi.org/10.1021/acs.jpclett.4c02289.

(11) Moise, T.; Rudich, Y. Uptake of Cl and Br by Organic Surfaces—A Perspective on Organic Aerosols Processing by Tropospheric Oxidants. *Geophys. Res. Lett.* **2001**, *28* (21), 4083–4086. https://doi.org/10.1029/2001GL013583.

(12) Zeng, M.; Wilson, K. R. Experimental Evidence That Halogen Bonding Catalyzes the Heterogeneous Chlorination of Alkenes in Submicron Liquid Droplets. *Chem. Sci.* **2021**, *12* (31), 10455–10466. https://doi.org/10.1039/D1SC02662C.

(13) Thompson, A. P.; Aktulga, H. M.; Berger, R.; Bolintineanu, D. S.; Brown, W. M.; Crozier, P. S.; in 't Veld, P. J.; Kohlmeyer, A.; Moore, S. G.; Nguyen, T. D.; Shan, R.; Stevens, M. J.; Tranchida, J.; Trott, C.; Plimpton, S. J. LAMMPS - a Flexible Simulation Tool for Particle-Based Materials Modeling at the Atomic, Meso, and Continuum Scales. *Comput. Phys. Commun.* **2022**, *271*, 108171. https://doi.org/10.1016/j.cpc.2021.108171.

(14) Malde, A. K.; Zuo, L.; Breeze, M.; Stroet, M.; Poger, D.; Nair, P. C.; Oostenbrink, C.; Mark, A. E. An Automated Force Field Topology Builder (ATB) and Repository: Version 1.0. *J. Chem. Theory Comput.* **2011**, *7* (12), 4026–4037. https://doi.org/10.1021/ct200196m.
(15) Schmid, N.; Eichenberger, A. P.; Choutko, A.; Riniker, S.; Winger, M.; Mark, A. E.; van Gunsteren, W. F. Definition and Testing of the GROMOS Force-Field Versions 54A7 and 54B7. *Eur. Biophys. J.* **2011**, *40* (7), 843–856. https://doi.org/10.1007/s00249-011-0700-9.
(16) Cohen, L.; Dodin, A.; Wilson, K.; Limmer, D. Accelerated Chlorination at the Surface of Organic Aerosol. ChemRxiv March 19, 2025. https://doi.org/10.26434/chemrxiv-2025-r0wcd.
(17) ATB, Squalene, KFEY. https://atb.uq.edu.au/molecule.py?molid=1175737#panel-information.
(18) Andersen, H. C. Rattle: A "Velocity" Version of the Shake Algorithm for Molecular Dynamics Calculations. *J. Comput. Phys.* **1983**, *52* (1), 24–34. https://doi.org/10.1016/0021-9991(83)90014-1.
(19) Hockney, R. W.; Eastwood, J. W. *Computer Simulation Using Particles*, Special student ed.; A. Hilger: Bristol [England] ; Philadelphia, 1988.
(20) Martínez, L.; Andrade, R.; Birgin, E. G.; Martínez, J. M. PACKMOL: A package for building initial configurations for molecular dynamics simulations. *J. Comput. Chem.* **2009**, *30* (13), 2157–2164. https://doi.org/10.1002/jcc.21224.
(21) Grossfield, A. WHAM: The Weighted Histogram Analysis Method. , http://membrane.urmc.rochester.edu/content/wham/.
(22) Kumar, S.; Rosenberg, J. M.; Bouzida, D.; Swendsen, R. H.; Kollman, P. A. THE Weighted Histogram Analysis Method for Free-Energy Calculations on Biomolecules. I. The Method. *J. Comput. Chem.* **1992**, *13* (8), 1011–1021. https://doi.org/10.1002/jcc.540130812.
(23) Kumar, S.; Rosenberg, J. M.; Bouzida, D.; Swendsen, R. H.; Kollman, P. A. Multidimensional Free-Energy Calculations Using the Weighted Histogram Analysis Method. *J. Comput. Chem.* **1995**, *16* (11), 1339–1350. https://doi.org/10.1002/jcc.540161104.
(24) Roux, B. The Calculation of the Potential of Mean Force Using Computer Simulations. *Comput. Phys. Commun.* **1995**, *91* (1), 275–282. https://doi.org/10.1016/0010-4655(95)00053-I.
(25) Souaille, M.; Roux, B. Extension to the Weighted Histogram Analysis Method: Combining Umbrella Sampling with Free Energy Calculations. *Comput. Phys. Commun.* **2001**, *135* (1), 40–57. https://doi.org/10.1016/S0010-4655(00)00215-0.
(26) Polley, K.; Wilson, K. R.; Limmer, D. T. On the Statistical Mechanics of Mass Accommodation at Liquid–Vapor Interfaces. *J. Phys. Chem. B* **2024**, *128* (17), 4148–4157. https://doi.org/10.1021/acs.jpcb.4c00899.
(27) Hinsberg, W.; Houle, F. Kinetiscope. https://hinsberg.net/kinetiscope/ (accessed 2025-03-01).
(28) Willis, M. D.; Wilson, K. R. Coupled Interfacial and Bulk Kinetics Govern the Timescales of Multiphase Ozonolysis Reactions. *J. Phys. Chem. A* **2022**, *126* (30), 4991–5010. https://doi.org/10.1021/acs.jpca.2c03059.
(29) Roper, G. H. The Kinetics of the Addition of Chlorine to Olefins in Carbon Tetrachloride. *Chem. Eng. Sci.* **1953**, *2* (1), 27–31. https://doi.org/10.1016/0009-2509(53)80004-7.
(30) Yates, K.; Leung, H. W. Kinetics and Stereochemistry of the Addition of Chlorine to Styrenes. *J. Org. Chem.* **1980**, *45* (8), 1401–1406. https://doi.org/10.1021/jo01296a011.

(31) Bienvenüe-Goëtz, E.; Ratsimandresy, B.; Ruasse, M. F.; Dubois, J. E. The Polar Reaction Constant for Alkene Chlorination. Similarity and Differences in the Chloronium and Bromonium Ion like Transition States. *Tetrahedron Lett.* **1982**, *23* (32), 3273–3276. https://doi.org/10.1016/S0040-4039(00)87590-5.
(32) Li, J.; Jiang, J.; Manasfi, T.; von Gunten, U. Chlorination and Bromination of Olefins: Kinetic and Mechanistic Aspects. *Water Res.* **2020**, *187*, 116424. https://doi.org/10.1016/j.watres.2020.116424.
(33) Asinger, F. CHAPTER 6 - THE CHLORINATION OF THE OLEFINS. In *Mono-Olefins*; Asinger, F., Ed.; Pergamon, 1968; pp 506–627. https://doi.org/10.1016/B978-0-08-011547-4.50009-4.
(34) Maryott, A. A. Circular of the Bureau of Standards No. 514::Table of Dielectric Constants of Pure Liquids. *NIST* **1951**.

Chapter 4. Kinetics of pH Dependent Fenton Chemistry and Iron(IV) Formation

This chapter is adapted from Cohen, L.; Willis, M.; Wilson, K. Iron (IV) Formation and the pH Dependent Kinetics of the Fenton Reaction* **2025. DOI: 10.26434/chemrxiv-2025-mmwkn.

4.1. Introduction

The Fenton reaction involves the oxidation of Fe^{2+} to Fe^{3+} by hydrogen peroxide, producing an intermediate with a stronger oxidizing ability. Since its discovery in 1894,[1] the Fenton reaction has been thoroughly examined in large part due to its central importance in biological,[2] environmental, and atmospheric[3–6] chemistry as well as for its application in advanced oxidation processes for water remediation and wastewater treatment.[7–9] Although the formation mechanism and identity of the strong oxidant in this reaction continue to be actively debated, there are two generally accepted mechanisms.[10] The Haber-Weiss mechanism forms hydroxyl radicals:[11]

$$Fe^{2+} + H_2O_2 \rightarrow Fe^{3+} + OH^- + \cdot OH \qquad \text{(R1)}$$

An alternative mechanism, proposed by Bray and Gorin, forms a highly reactive high-valent Fe(IV) intermediate:[12]

$$Fe^{2+} + H_2O_2 \rightarrow Fe^{IV}O^{2+} + H_2O \qquad \text{(R2)}$$

The formation of hydroxyl radicals in R1 is supported by many studies,[13–15] and is broadly accepted. More recent investigations, however, report evidence that at certain reaction conditions, oxidation does not proceed solely or predominantly through the OH radical pathway.[16–19] Instead, it was hypothesized that at neutral and higher pH,[19–23] Fe(IV) is formed.[16,18,24–28]

Important evidence for Fe(IV) was reported by Bataineh *et al.*,[21] where the differences in the oxidation products of dimethyl sulfoxide (DMSO) were used to distinguish between the two reactive intermediates. DMSO oxidized by OH radicals produces methlysulfinic acid and ethane[29,30], whereas reaction with Fe(IV) produces dimethyl sulfone[31] ($DMSO_2$). NMR measurements showed that the Fe(IV) pathway was undetectable in acidic conditions but became substantial at pH = 6-7. This shift in product distributions with pH led Bataineh *et al.*[21] to propose the following mechanism and rate coefficients,

$$Fe(H_2O)_6^{2+} \rightleftharpoons Fe(H_2O)_5OH^+ + H^+ \qquad pKa = 9.5 \qquad \text{(R3)}$$

Haber-Weiss Mechanism (OH Radical)

$$Fe(H_2O)_6^{2+} + H_2O_2 \rightarrow Fe(III) + \cdot OH \qquad k_4 = 58\ \text{M}^{-1}\text{s}^{-1} \qquad \text{(R4)}$$

$$\cdot OH + DMSO \rightarrow CH_3SO_2H + 0.5\,C_2H_6 \qquad k_5 = 7 \times 10^9\ \text{M}^{-1}\text{s}^{-1} \qquad \text{(R5)}$$

$$\cdot OH + Fe(H_2O)_6^{2+} \rightarrow Fe(III) \qquad k_6 = 3.2 \times 10^8\ \text{M}^{-1}\text{s}^{-1} \qquad \text{(R6)}$$

Bray-Gorin Mechanism (Fe(IV))

$$Fe(H_2O)_5OH^+ + H_2O_2 \rightarrow Fe(IV) \qquad k_7 = 592\ \text{M}^{-1}\text{s}^{-1} \qquad \text{(R7)}$$

$$Fe(IV) + DMSO \rightarrow DMSO_2 + Fe(H_2O)_6^{2+} \qquad k_8 / k_9 = 1.7 \times 10^{-4} \qquad \text{(R8)}$$

$$Fe(IV) + Fe(II) \rightarrow 2Fe(III) \qquad \text{(R9)}$$

Fe(II) in R3 ultimately governs oxidant formation (·OH vs. Fe(IV)). For example, $Fe(H_2O)_6^{2+}$ produces OH· radicals via the Haber Weiss mechanism, whereas $Fe(H_2O)_5OH^+$ produces Fe(IV) via the Bray-Gorin mechanism. Each oxidant can react with Fe(II) or with DMSO to yield the observed products.

Here, we re-analyze both the experimental results and the kinetic model presented by Bataineh *et al.*[21] Our analysis suggests that although the Bataineh *et al.*[21] model qualitatively explains the branching between OH· and Fe(IV) via the acid-base equilibrium in R3, the rate constant for R7 appears to be derived based upon the total [Fe(II)] without explicitly accounting for its speciation. This oversight is particularly significant at pH 6-7 since $Fe(H_2O)_5OH^+$, the precursor for Fe(IV) in R7, is a small fraction (~0.1%) of the total Fe(II). As detailed below, our reconstruction of the mechanism using the correct Fe(II) speciation, suggests that the rate coefficient for forming Fe(IV) in R7 is actually ~1500 times ($k_7 \sim 10^6$ M^{-1} s^{-1}) larger than originally reported by Bataineh *et al.*[21] (*i.e.*, $k_7 = 592$ $M^{-1}s^{-1}$). Combining our reanalysis of Bataineh *et al.*[21] with recent work by Stanbury,[32] which details how thermodynamic equilibria govern speciation and thus the Fenton mechanism at acidic pH, enables the formulation of a unified kinetic model that faithfully replicates the oxidation kinetics of Fe(II) by H_2O_2 from acidic to neutral conditions.

4.2. Methods

Kinetic simulations are performed in Kinetiscope,[33] a stochastic reaction-diffusion simulator that randomly selects outcomes from probability-weighted reaction steps. Like ordinary differential equation solvers, mechanisms are built up from elementary reaction steps and rate constants. The rate constants used by Bataineh *et al.*[21] are obtained from prior literature for the Haber-Weiss mechanism (R4-R6)[29]. The Bray-Gorin rate constants (R7-R9) were constrained by Bataineh *et al.*[21] by fitting their experimental kinetics, which were obtained by monitoring Fe(III) formation through its absorbance at 270nm in a stopped flow apparatus. Although Bataineh *et al.*[21] compare simulation results from Kinsim[34] with their observations (Fig. 3 in Ref [21]) there is insufficient information for us to replicate the mechanism (R3-R9). For example, there is no description of the forward and backward rate coefficients that comprise the iron acid-base equilibrium in R3, nor what values of the absolute rate constants were used for R8 and R9. Without these details, we reconstruct their mechanism using the following assumptions:

1) The backward rate coefficient for the acid-base equilibrium is diffusion-limited with a rate constant of $k_r = 10^{10}\ M^{-1}s^{-1}$. The forward rate constant is set to a value that maintains the correct pKa, (*i.e.,* $k_f = k_r \times k_a = 3.2\ s^{-1}$).
2) R9 is set to be diffusion limited with a rate constant of $k_9 = 10^{10}$ $M^{-1}s^{-1}$, with $k_8 = 1.7 \times 10^6$ $M^{-1}s^{-1}$ calculated to obtain the correct ratio of k_8 / k_9 reported by Bataineh *et al.*[21].
3) The Fe(II) species produced in R8 and consumed in R9 is $Fe(H_2O)_6^{2+}$, which is appropriate, as this is the predominant Fe(II) species present at pH < 9.5.

Assumptions 1-3 preserve the rate constants that are said to be constrained by experimental data and the original model (i.e., k_7 and k_8 / k_9). Assumptions 1 and 2 use rate coefficients at or near a kinetic upper limit to drive the overall reaction as fast as possible, since, as will be shown below, the base model proposed by Bataineh *et al.*[21] substantially underpredicts the observed kinetics. The reconstructed kinetic model using assumptions 1-3 is termed RM.

4.3. Results

A comparison between RM kinetic simulations and the experimental kinetics for Fe(III) formation recorded by Bataineh *et al.*[21] is shown in Figure 4.1. RM substantially underpredicts the rate of formation of Fe(III) observed in the experiment. Complete conversion of the reagents should yield [Fe(III)] = 2×10^{-5} M. However, we note that converting the raw absorbance provided by Bataineh *et al.*[21] to concentration recovers a slightly smaller value (*i.e,* 1.9×10^{-5} M). A comparison of RM predictions and the formation kinetics of Fe(III) as a function of [DMSO] is shown in the Supplementary Information (Figure 4.S1) and similarly yields slower simulated kinetics than are observed in the experiment.

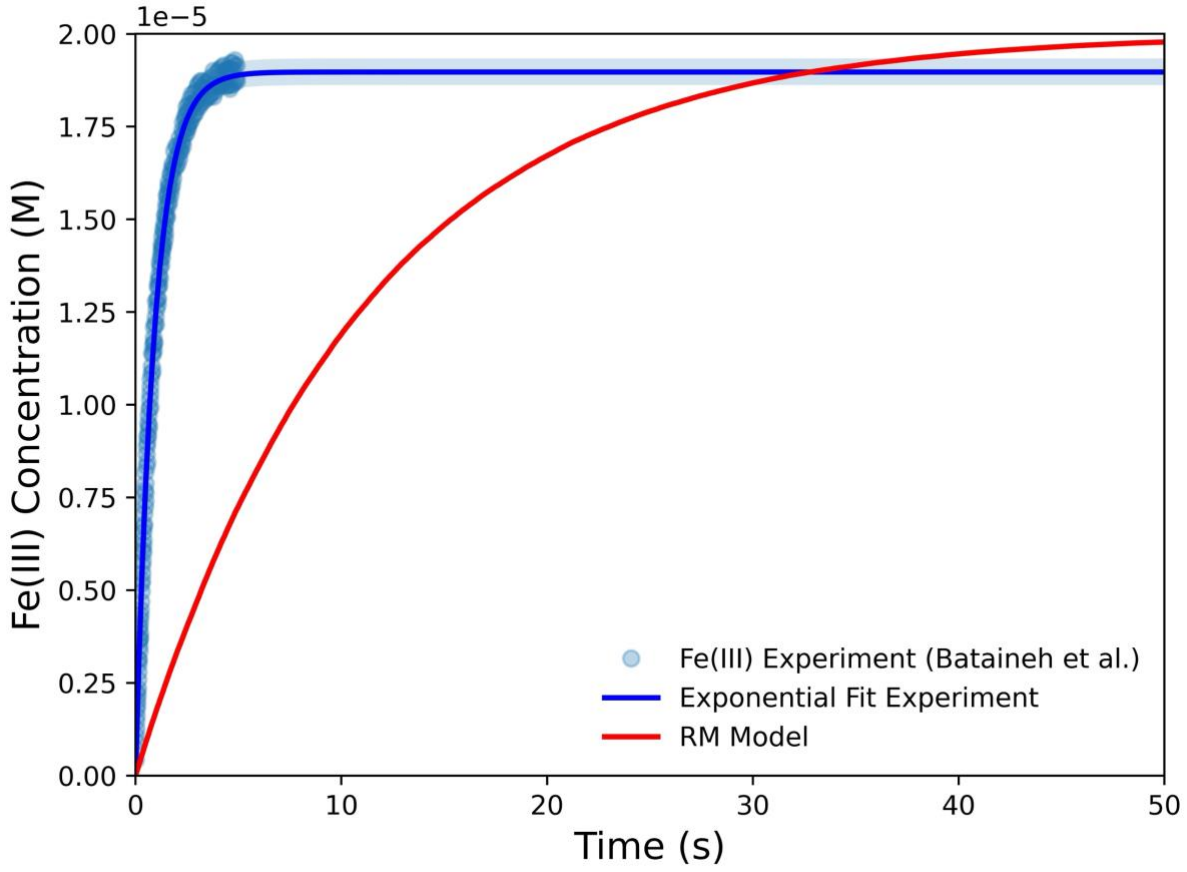

Figure 4.1 – Fe(III) concentration as a function of time for the RM model (red) and experimental data (blue) reproduced from Fig. S6 in the Supplementary Information of Bataineh et al[21] and converted to concentration using their reported extinction coefficient. Experimental conditions: 0.02mM Fe(II), 0.78mM H_2O_2, pH = 6.2 (buffered by 0.56mM MES).

When properly accounting for Fe(II) speciation in R3, the rate constant (k_7) for the formation of Fe(IV) as reported by Bataineh *et al.*[21] is simply too small to replicate the experimental results (Figure 4.1). As a result, we are left to conclude that iron speciation was omitted in their kinetic simulations. To test this hypothesis, we replaced $Fe(H_2O)_6^{2+}$ and $Fe(H_2O)_5OH^+$ with a generic Fe(II) species, thereby effectively eliminating iron speciation in RM. This species is used in R4 and R7 to form OH· and Fe(IV), respectively. As a result, the acid–

base equilibrium no longer governs the reactivity of Fe(IV). A comparison of this non-speciated version of RM with the experimental results is shown in Figure 4.2. For this case, the simulations replicate the experiment.

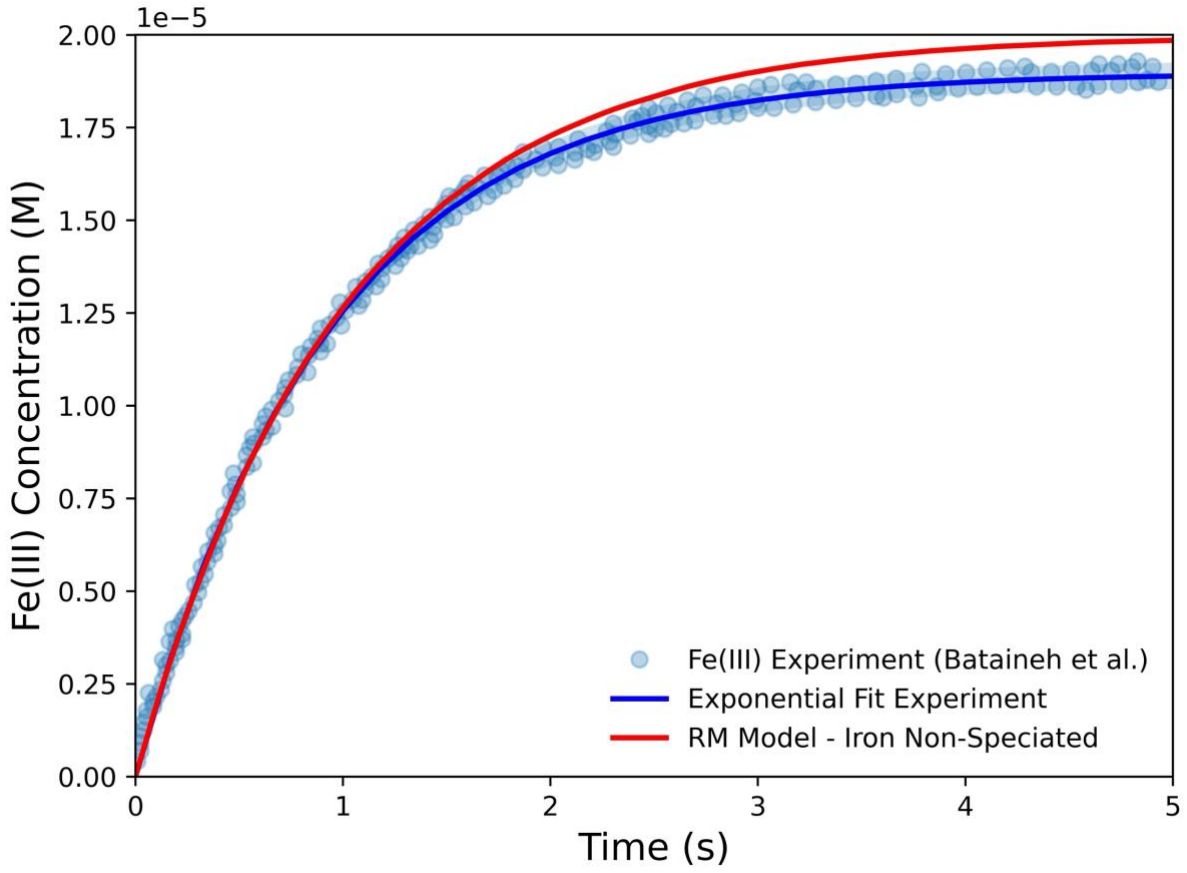

Figure 4.2 – Fe(III) concentration as a function of time for the RM model with no iron speciation (red) and experimental data (blue) reproduced from Fig. S6 in supplementary information of Bataineh et al[21]. Experimental conditions: 0.02mM Fe(II), 0.78mM H_2O_2, pH 6.2 (buffered by 0.56mM MES).

The rate constant (k_{Fe}) for the Fenton reaction when one of the reagents is in excess is defined as $-\frac{d[H_2O_2]}{dt} = -\frac{1}{2}\frac{d[Fe(II)]}{dt} = k_{Fe}[Fe(II)][H_2O_2]$. Subsequently, k_{obs} in Bataineh *et al.*[21] is the observed rate, not corrected for stoichiometry, measured by the Fe(III) formation rate when H_2O_2 is in excess, *i.e.* $k_{obs} = 2k_{Fe} = \frac{d[Fe(III)]}{dt}\frac{1}{[H_2O_2]}$ in units of $M^{-1}s^{-1}$. Shown in Figure 4.3 is the observed rate of Fe(III) formation (k_{obs}) as a function of [DMSO] reported in Ref. [21] compared with different versions of the RM model. There is general agreement between the experimental results and the *non-speciated* RM model across varying DMSO concentrations. In contrast, however, when including Fe(II) speciation in R3, k_{obs} predicted by the RM model to be an order of magnitude smaller and somewhat invariant to [DMSO]. Although the *non-speciated* RM agrees with the experimental results, it does so using unphysical iron speciation. At pH=6, the experimental conditions are more than three pH units away from the pKa of Fe(II). This means that the concentration of $Fe(H_2O)_5OH^+$, the species required for Fe(IV) formation, is less than 0.1% of the total Fe(II) species in solution. As a result, the model's agreement arises from an unrealistic assumption rather than an accurate mechanistic representation. Moreover, without

including explicit Fe(II) speciation, the model cannot capture pH dependence, as the original premise was to link Fe(IV) formation to the iron acid-base equilibrium (R3) in order to construct a predictive kinetic model across varying pH conditions. In addition to explicit kinetic simulations, Bataineh *et al.*[21] provided a closed-form approximation to predict how k_{obs} varies with [DMSO] (See Eq. 10 in Ref. [21]). Further analysis of that equation (see SI Section S2) points to the same conclusion; that the derivation of this equation neglected iron speciation.

Thus, we conclude that the rate constant suggested by Bataineh et al.[21] for the formation of Fe(IV) in R7 must be substantially underestimated since it is derived without considering the actual concentration of $Fe(H_2O)_5OH^+$ at pH = 6. This is why increasing the Fe(IV) formation rate constant k_7 (from 592 $M^{-1}s^{-1}$ to $1.4 \times 10^6 M^{-1}s^{-1}$) is required to match the experimental results (Figure 4.3 and Fig. S4).

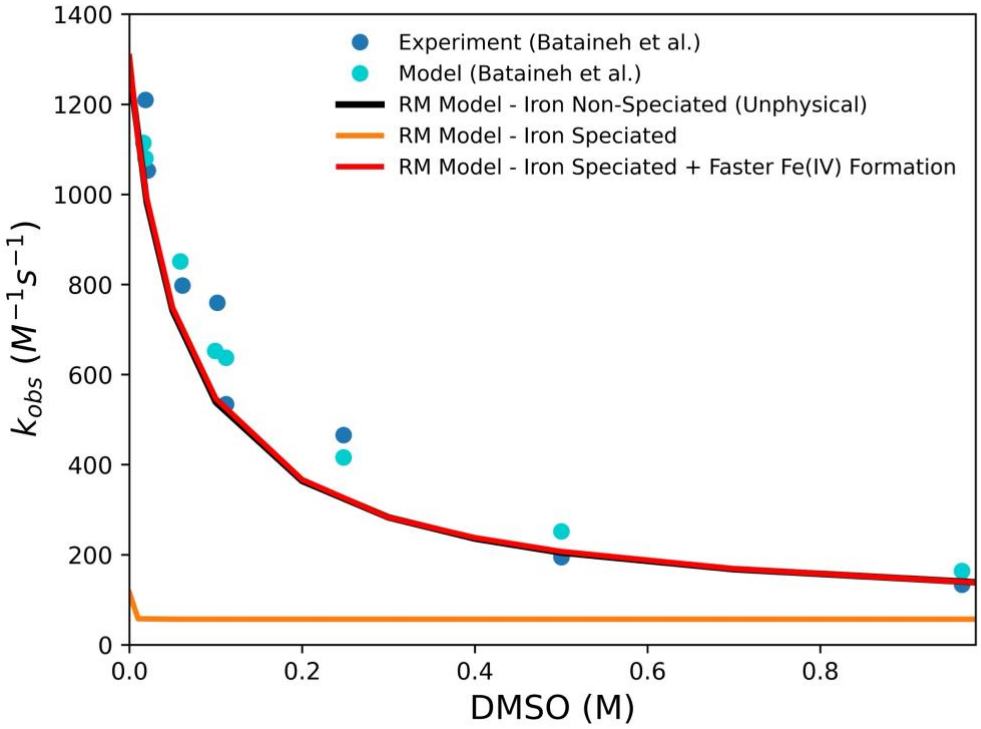

Figure 4.3 – k_{obs} is plotted as a function of DMSO concentration showing Bataineh et al.[21] experimental results at pH=6 (blue circles) and model simulation (cyan circles) reproduced from their Fig. 3. The iron speciated RM model is shown in orange (data point for 0M DMSO is shown in Figure 4.1), and the non-speciated RM model is shown in black (data point for 0M DMSO is shown in Figure 4.2). RM model accounting for both iron speciation and a faster formation rate of Fe(IV) $k_7 = 1.4 \times 10^6 M^{-1}s^{-1}$ is shown in red. A line connecting each model prediction is shown to guide the eye.

The RM model incorporating faster Fe(IV) formation and explicit Fe(II) speciation gets closer to a realistic representation of the Fenton reaction but remains unsatisfactory, since it omits Fe(III) speciation, which is known to vary substantially with pH (see Sanez et al.[35] Fig. 2 or Remucal and Sedlak[20] Fig. 3). Furthermore, because the Fe(IV) formation rate was adjusted to fit the experimental data in shown Figure 4.3 at pH=6, the model performs well under these conditions. However, when extended to pH=7, the modified RM model underpredicts the observed

reaction rate (Figure 4.S4), suggesting that in its current form, it does not fully capture the pH dependent increase in Fe(II) oxidation.

Recently, Stanbury[32] conducted an exhaustive survey of Fenton reaction kinetics, identifying more than 200 published kinetic models that violate the principle of detailed balancing, *i.e.* that the ratio of forward and reverse rate constants for each elementary step must equal the corresponding equilibrium constant. In addition to this critical analysis, Stanbury[32] presented a validated radical mechanism for the Fenton reaction under acidic conditions. Expanding on this work, we set out to develop a unified reaction mechanism spanning acidic to neutral conditions that incorporates both Fe(IV) formation and the correct thermodynamic speciation of iron and radical species (*i.e.*, $\cdot OH, HO_2\cdot$, and $O_2^{\cdot-}$). The full reaction mechanism, including literature references for the steps and rate constants, is shown in Table 4. 1.

Table 4.1: Fenton Chemistry Kinetic Model from Acidic to Neutral pH. For simplicity, the iron species appear without water coordination, i.e. Fe^{2+} represents $Fe(H_2O)_6{}^{2+}$ and $Fe(OH)^+$ represents $Fe(H_2O)_5OH^+$. Reactions M19, M6, M20, and M25 or M26 in Table 4. 1 are analogous to R3, R4, R7, and R9, respectively, in Bataineh *et al.* kinetic model or RM model. *modified from Ref. [32]. Equilibrium constants are shown in SI units with concentrations given in moles per liter (M), water is assumed to have an activity of 1, and not concentration of 55M.

Reaction	Equilibrium/Rate Constants	Ref.	#
$\mathbf{HO_2\cdot \rightleftharpoons H^+ + O_2^{\cdot-}}$	$K = 1.3\times10^{-5}$M $k_f = 1.3\times10^{5}$ M^{-1}s^{-1} $k_r = 10^{10}$ s^{-1}	32,36	M1
$\mathbf{Fe^{3+} + H_2O \rightleftharpoons Fe(OH)^{2+} + H^+}$	$K = 4\times10^{-3}$M $k_f = 4\times10^{7}$ M$^{-1}s^{-1}$ $k_r = 10^{10}$ s^{-1}	32,37*	M2
$\mathbf{Fe^{3+} + H_2O_2 \rightleftharpoons Fe(HO_2)^{2+} + H^+}$	$K = 2\times10^{-3}$ $k_f = 2\times10^{7}$ M$^{-1}s^{-1}$ $k_r = 10^{10}$ s^{-1}	32,37	M3
$\mathbf{Fe(HO_2)^{2+} \rightleftharpoons Fe^{2+} + HO_2\cdot}$	$k_f = 1.6\times10^{-3}$ s^{-1} $k_r = 2.1\times10^{6}$ M^{-1}s^{-1}	32	M4
$\mathbf{Fe(HO_2)^{2+} + Fe(OH)^{2+} \rightarrow 2\,Fe^{2+} + O_2 + H_2O}$	$k = 5.0$ M^{-1}s^{-1}	32	M5
$\mathbf{Fe^{2+} + H_2O_2 \rightarrow Fe(OH)^{2+} + \cdot OH}$	$k = 68$ M^{-1}s^{-1}	32	M6
$\mathbf{\cdot OH + H_2O_2 \rightarrow HO_2\cdot + H_2O}$	$k = 1.7\times10^{7}$ M^{-1}s^{-1}	32	M7
$\mathbf{Fe^{3+} + O_2^{\cdot-} \rightarrow Fe^{2+} + O_2}$	$k = 4\times10^{8}$ M^{-1}s^{-1}	32	M8
$\mathbf{Fe^{2+} + \cdot OH \rightarrow Fe(OH)^{2+}}$	$k = 3\times10^{8}$ M^{-1}s^{-1}	32	M9
$\mathbf{HO_2\cdot + HO_2\cdot \rightarrow H_2O_2 + O_2}$	$k = 8.3\times10^{5}$ M^{-1}s^{-1}	32	M10
$\mathbf{Fe^{3+} + 2\,H_2O \rightleftharpoons Fe(OH)_2{}^{+} + 2\,H^+}$	$K = 1.6\times10^{-5}$ M^2 $\mathbf{k_f = 1.6\times10^{5}\ M^{-1}s^{-1}}$ k_r $\mathbf{= 10^{10}\ s^{-1}}$	32	M11
$\mathbf{2\,Fe^{3+} + 2\,H_2O \rightleftharpoons Fe_2(OH)_2{}^{4+} + 2\,H^+}$	$K = 7.9\times10^{-4}$M $k_f = 7.9\times10^{3}$ M^{-1}s^{-1} $k_r = 10^{7}$ s^{-1}	32,38	M12
$\mathbf{Fe(OH)^{2+} + H_2O_2 \rightleftharpoons Fe(OH)(HO_2)^{2+} + H^+}$	$K = 2\times10^{-4}$ $k_f = 2\times10^{6}$ M^{-1}s^{-1} $k_r = 10^{10}$ s^{-1}	32	M13
$\mathbf{Fe(OH)(HO_2)^{2+} \rightleftharpoons Fe^{2+} + O_2^{\cdot-} + H_2O}$	$K = 2.4\times10^{-11}$M $k_f = 2.4\times10^{-4}$M^{-1}s^{-1} $k_r = 10^{7}$s^{-1}	32	M14
$\mathbf{Fe(OH)_2{}^{+} + H_2O_2 \rightleftharpoons Fe^{2+} + O_2^{\cdot-} + 2\,H_2O}$	$K = 1.2\times10^{-12}$ $k_f = 1.2\times10^{-2}$ M^{-1}s^{-1}$k_r = 10^{10}$s^{-1}	32*	M15
$\mathbf{HO_2\cdot + O_2^{\cdot-} + H_2O \rightarrow H_2O_2 + O_2 + \cdot OH}$	$k = 9.7\times10^{7}$ M^{-2}s^{-1}	39	M16
$\mathbf{Fe^{2+} + O_2^{\cdot-} + H_2O \rightleftharpoons Fe(OH)^{2+} + HO_2^-}$	$K = 4.5\times10^{2}$ $k_f = 10^{7}$ M$^{-1}s^{-1}$ $k_r = 2.2\times10^{4}$ s^{-1}	32	M17
$\mathbf{H_2O_2 \rightleftharpoons H^+ + HO_2^-}$	$K = 2.2\times10^{-12}$ M $k_f = 2.2\times10^{-2}$M$^{-1}s^{-1}k_r$ $= 10^{10}$s^{-1}	32,40	M18
$\mathbf{Fe^{2+} + H_2O \rightleftharpoons Fe(OH)^{+} + H^+}$	$K = 7.9\times10^{-10}$M $k_f = 7.9$ M$^{-1}s^{-1}$ $k_r = 10^{10}$ s^{-1}	37	M19
$\mathbf{Fe(OH)^{+} + H_2O_2 \rightarrow Fe^{IV}O^{2+} + H_2O + OH^-}$	$\mathbf{k = \sim1\times10^{6}\ M^{-1}s^{-1}}$		M20
$\mathbf{Fe^{IV}O^{2+} + H_2O \rightarrow Fe^{3+} + \cdot OH + OH^-}$	$k = 1.3\times10^{-2}$ s^{-1}	41	M21
$\mathbf{Fe^{IV}O^{2+} + \cdot OH + H^+ \rightarrow Fe^{3+} + H_2O_2}$	$k = 1\times10^{7}$ M^{-1}s^{-1}	41	M22
$\mathbf{Fe^{IV}O^{2+} + H_2O_2 \rightarrow Fe^{3+} + HO_2\cdot + OH^-}$	$k = 1\times10^{4}$ M^{-1}s^{-1}	41	M23

$Fe^{IV}O^{2+} + HO_2 \cdot \rightarrow Fe^{3+} + O_2 + OH^-$	$k = 2 \times 10^6$ $M^{-1}s^{-1}$	[41]	M24
$Fe^{2+} + Fe^{IV}O^{2+} + H_2O \rightarrow 2\,Fe^{3+} + 2\,OH^-$	$k = 7.2 \times 10^4$ $M^{-1}s^{-1}$	[41]	M25
$Fe^{2+} + Fe^{IV}O^{2+} + H_2O \rightarrow Fe(OH)_2Fe^{4+}$	$k = 1.8 \times 10^4$ $M^{-1}s^{-1}$	[41]	M26
$Fe(OH)_2Fe^{4+} \rightarrow 2\,Fe^{3+} + 2\,OH^-$	$k = 0.49$ s^{-1}	[41]	M27
$Fe(OH)_2Fe^{4+} + 2\,H^+ \rightarrow 2\,Fe^{3+} + 2\,H_2O$	$k = 2$ s^{-1}	[41]	M28

Reactions M1-M10 are adapted from Scheme 3 in Stanbury,[32] while reactions M11-M19 extend the model to include additional speciation or radical reactivity relevant at higher pH values. The equilibrium constants for M2 and M15 are noted with an asterisk since they are modified from Ref. [32] to ensure compliance with Wegscheider's condition and internal consistency of the model reaction loops (Supplementary Information Section S5). Rate constants for the reactions of Fe(IV) in M21-M28 are taken from Jacobsen *et al.*[41], which characterized ferryl ion reactivity in acidic solutions. The only *unknown* irreversible rate constant in the model is M20; the rate of Fe(IV) formation. This rate constant is set to $k_{\mathrm{M20}} = 1 \times 10^6 \mathrm{M^{-1}s^{-1}}$, since the analysis presented above using the iron speciated RM model suggests a rate constant on that order is needed. Furthermore, k_{M20} is of similar magnitude to the formation rate of Fe(IV) in the reaction of Fe(II) with ozone ($8.5 \pm 0.9 \times 10^5$ $\mathrm{M^{-1}s^{-1}}$)[41].

To implement the propagation of reactions in a kinetic scheme, we assume that equilibrium is maintained using diffusion-limited kinetics in cases where no explicit slower forward or reverse rate constants are available. This is achieved by using a diffusion limit of 10^{10} $M^{-1}s^{-1}$ for reactions M1-M3, M13, M15, M18, M19, and a termolecular limit of $10^7 M^{-2}$ s^{-1} for reactions M12, M14, M17. An exception was applied to M11; although three species are involved in the reverse reaction, a bimolecular limit is assumed since equilibrium replenishing at pH=7 was shown to proceed on a time scale of minutes. Changing this rate had little to no effect on the overall observed rate but influenced Fe(III) speciation above pH = 4 (Supplementary Information Section S6).

Our unified kinetic model predictions for buffered pH conditions are presented in Figure 4.4. The model replicates the experimental results and captures the pH-dependent transition of the Fenton reaction rate $k_{Fe}(M^{-1}s^{-1})$, measured in the presence of excess of H_2O_2. It reproduces the flat kinetic dependence at acidic pH (pH<3), followed by a pronounced rate acceleration as the system approaches near-neutral pH. In contrast, the radical only oxidation pathway, *i.e.* disabling Fe(IV) formation in the unified kinetic framework, shows minimal pH sensitivity with some uptake at pH>4. This weaker pH dependence suggests that the radical mechanism alone cannot account for the substantial increase in Fe(II) oxidation rate at higher pH, underscoring the importance of including Fe(IV)-mediated pathways and pH-sensitive iron speciation in kinetic models seeking to accurately represent Fenton chemistry.

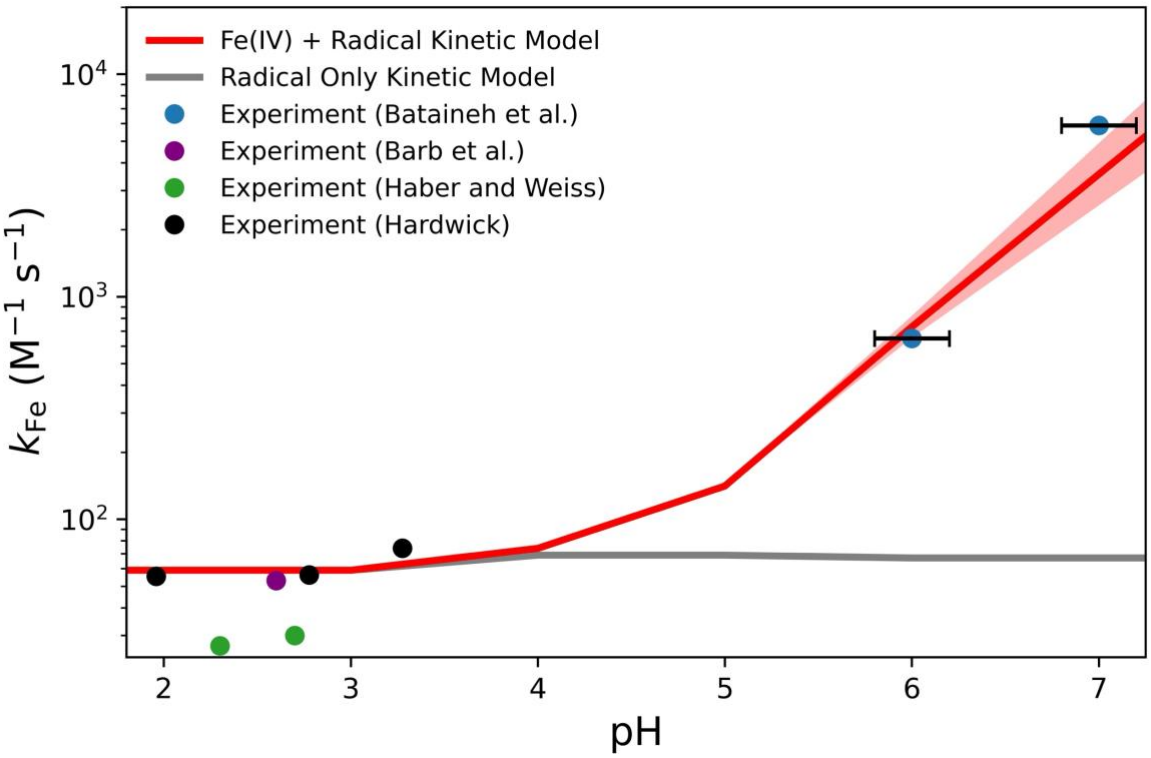

Figure 4.4 – The pseudo first order rate constant for the Fenton reaction $k_{Fe}(M^{-1}s^{-1})$ for conditions with excess H_2O_2 is plotted against the buffered pH conditions. Experimental results are shown with circle markers from Bataineh et al.[21] in non-coordinating buffers: MES for pH=6 and MOPS for pH=7(blue), in acidic conditions experimental results are from Barb et al.[42] (purple), Haber and Weiss[11] (green), and Hardwick[43] (black). Kinetic model predictions are shown for the unified model in red with a red shaded area describing the uncertainty in estimating the exponential fit and k_{Fe} from the model kinetic traces. Predictions for the radical only oxidation pathway are shown in grey. A line to guide the eye is shown connecting model predictions.

4.4. Discussion

To the best of our knowledge, the unified model presented above and shown in Figure 4.4 is the first framework for Fenton chemistry that uses physically realistic iron speciation and correctly describes the pH dependence of the reaction. This framework is proposed as a base kinetic model that establishes a mechanistic foundation for describing Fenton chemistry across a core pH range. However, it does not capture all the complexities that can arise from ionic strength effects, photo-Fenton reactions, ligand coordination, and complexation. These factors are all known to significantly influence Fenton chemistry in complex ways.[6,18,20,22,41,42,44–50] A more complex model would be required to begin incorporating these additional influences.

An advantage of using a kinetic framework for Fenton chemistry that includes detailed iron speciation is that further complexities can be evaluated through their direct effect on a specific species or equilibrium constants. Further constraining kinetic rates for forward and reverse equilibrium reactions, applying corrections to equilibrium constants and irreversible reactions based on ionic strength and temperature, and additional experimental data for Fe(IV) reactivity and speciation, will all increase the kinetic model accuracy and its capabilities in describing Fenton chemistry. The availability of this framework enables targeted exploration of specific systems, experimentally or computationally, by tuning rate constants, modifying equilibria, or introducing

new elementary steps to represent ligand binding or competitive complexation that are relevant to the system of interest. This framework lays the groundwork to promote a shift from isolated system-specific studies toward a transferable and mechanistically consistent understanding of Fenton chemistry.

Beyond its application to canonical Fenton systems, it is also possible to use this framework to describe "Fenton-like" reactions starting from Fe(III) oxidation, although a more rigorous treatment of iron precipitation would be required. For Fenton reaction timescales on the order of seconds to minutes, such as those plotted in Figure 4.4, little to no precipitation of newly formed Fe(III) hydroxide is expected to occur or significantly impact the kinetic results.[51] In contrast, starting from a solution of fully equilibrated Fe(III) will involve solid precipitates. Accurately modeling "Fenton-like" systems or very slow Fenton chemistry within this framework is feasible, provided that solid-phase equilibria are incorporated to account for precipitation effects on iron speciation and reactivity. This example highlights a specific opportunity to broaden the framework's application to address more complex chemical systems that include solid-phase interactions or additional equilibrium constraints.

A significant advantage of a robust kinetic model is that it can be used to test the "kinetic viability" of theoretical predictions. For example, theoretical work by Lu *et al.*[52] reported evidence that Fe(IV) is formed after complexation with hydrogen peroxide. Specifically, at pH < 7.7, Fe(IV) was proposed to form via the reaction of OH radical with water coordinated $Fe(OH)^{2+}$, *i.e.* $(H_2O)_5Fe^{III}(OH)^{2+}$. To evaluate this mechanism, we replaced the Fe(IV) formation step (M20) in our model with that proposed by Lu *et al.*[52] : $Fe(OH)^{2+} + \cdot OH \rightarrow FeO^{2+} + H_2O$. The resulting predictions at pH 6 are too slow to reproduce the experimental data (Supplementary Information Section S8). While this reaction pathway may be energetically favorable, our model suggests that its overall contribution to the Fenton reaction rate is kinetically insignificant. Thermodynamic favorability alone does not translate to kinetic relevance in this case, as assigning the reaction a diffusion-limited rate constant, pushing to a kinetic upper limit, still results in Fe(IV) formation rate that is too low to account for the acceleration observed in near-neutral pH. No fitting parameters were used to evaluate the validity of the Fe(IV) formation pathway proposed by Lu *et al.*[52] within the framework, since the only fit parameter (the reaction rate of M20) was removed from the analysis. This ensures an unbiased comparison between the kinetic validity of that pathway vs. reaction M20, already included in the model. Evidently, our model is found to assert that the primary mechanism for an accelerated rate of Fenton chemistry in the transition from acidic to neutral pH is the Fe(IV) formation pathway through the reaction of $Fe(OH)^{+}$ with hydrogen peroxide (M20). This pathway was also supported in *ab-initio* molecular dynamics simulations conducted by Ensing et al.[27]

4.5. Conclusions

A unified kinetic model for Fenton Chemistry is developed that includes both OH radical and Fe(IV) formation pathways. To our best knowledge, this is the first kinetic model that is able to quantitatively reproduce the pH dependence of the Fenton reaction while incorporating valid iron speciation. Since the model treats speciation explicitly, further complexities can be added as influencing a single species or through their effect on thermodynamic equilibria. The model provides a flexible kinetic framework that opens up opportunities for both experiment and theory to challenge assumptions and iterate on its current formulation. This framework advances our

fundamental understanding of Fenton chemistry, a mechanism debated in the literature for over a hundred years.

4.6. Supporting Information

4.6. Section S1: RM Model Predictions and Comparison to Experiments

Comparison of the RM model formation rate of Fe(III) to the experimental kinetics reported in Bataineh *et al.*[21] Fe(III) concentrations are calculated using the extinction coefficient of $2650 \pm 50 M^{-1} cm^{-1}$ and path length of 1cm given in Ref. [21] using Beer-Lambert law.

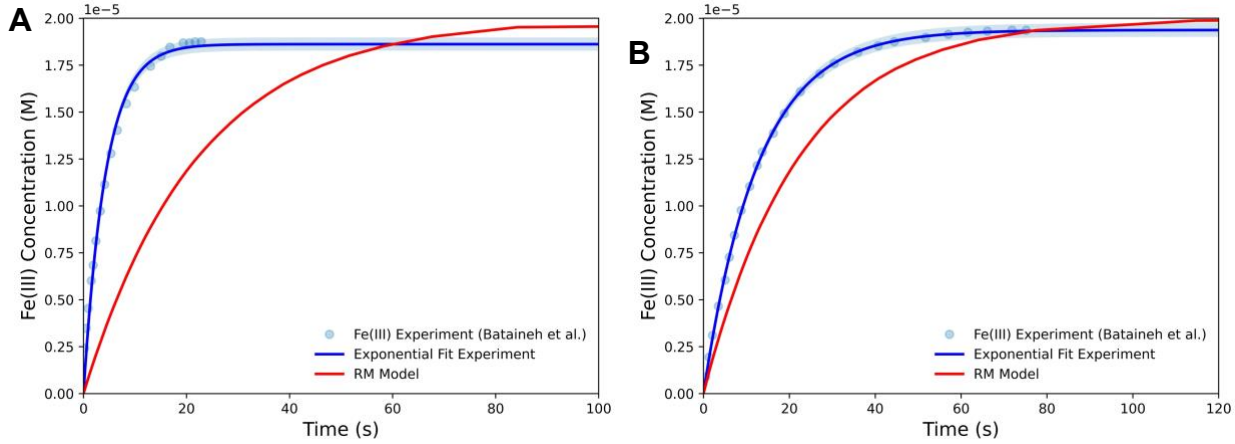

Figure 4.S1: Comparison of RM model to the experimental traces from Bataineh *et al*. (reproduced from Fig. S7 and S8)[21] at (A) [DMSO] = 0.5M and (B) [DMSO] = 0.98M. Experimental conditions: 0.02mM Fe(II), 0.78mM H_2O_2, pH = 6.2 (buffered by 0.56mM MES).

Similar to Figure 4.4.1 in the main text, the RM model consistently underpredicts the formation rate of Fe(III) reported in Ref [21] across increasing [DMSO]. Complete conversion of the reagents should yield [Fe(III)] = 2×10^{-5}M. Yet, inspection of Figures 1(main text), S1A, and S1B shows recovery of only $1.86 - 1.94 \times 10^{-5}$M.

A comparison of the non-speciated RM model formation rate of Fe(III) is shown in Figure 4.S2.

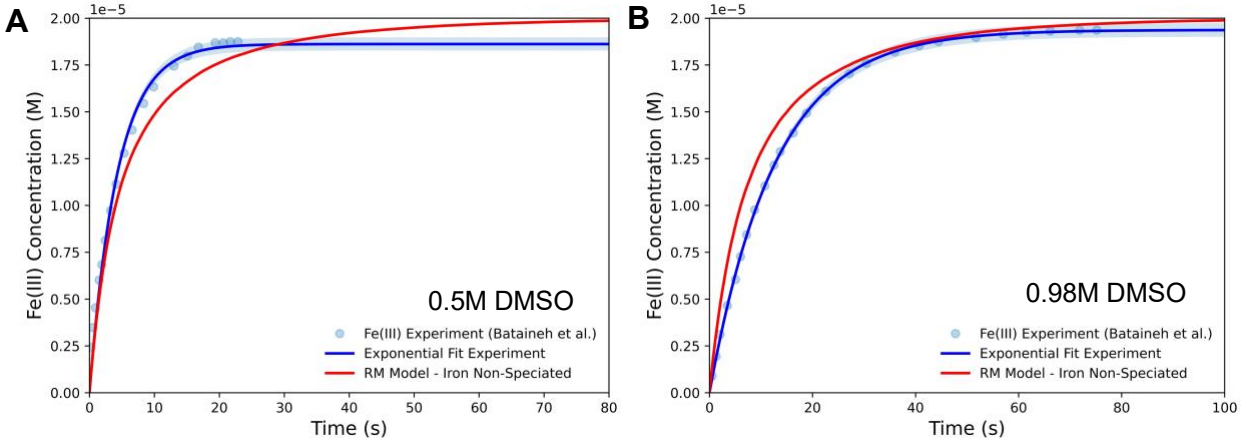

Figure 4.S2: Comparison of non-speciated RM model to experiment traces from Bataineh et al. (reproduced from Fig S7 and S8)[21] Experimental conditions: 0.02mM Fe(II), 0.78mM H_2O_2, pH 6.2 (buffered by 0.56mM MES) and (A) 0.5M DMSO or (B) 0.98M DMSO.

Figure 4.S2 shows that across DMSO concentrations, the non-speciated RM model is in good agreement with the experimental results.

4.6. Section S2: Derivation of k_{obs} - Eq. 10 in Bataineh et al.

A derivation of an expression for k_{obs} is shown below. We begin from the kinetic rate law expressions shown in Scheme 1 presented in the main text.

$$\frac{d[Fe(III)]}{dt} = k_4\left[Fe(H_2O)_6{}^{2+}\right][H_2O_2] + k_6\left[Fe(H_2O)_6{}^{2+}\right][OH\cdot] + 2k_9[Fe(IV)][Fe(II)] \quad \text{Eq. (S1)}$$

$$\frac{d[OH\cdot]}{dt} = k_4\left[Fe(H_2O)_6{}^{2+}\right][H_2O_2] - k_5[DMSO][OH\cdot] - k_6\left[Fe(H_2O)_6{}^{2+}\right][OH\cdot] \quad \text{Eq. (S2)}$$

$$\frac{d[Fe(IV)]}{dt} = k_7[Fe(H_2O)_5OH^+][H_2O_2] - k_8[Fe(IV)][DMSO] - k_9[Fe(IV)][Fe(II)] \quad \text{Eq. (S3)}$$

Applying the steady state approximation to both OH · (Eq. S2) and Fe(IV) (Eq. S3),

$$0 = \frac{d[OH\cdot]}{dt} = k_4\left[Fe(H_2O)_6{}^{2+}\right][H_2O_2] - k_5[DMSO][OH\cdot] - k_6\left[Fe(H_2O)_6{}^{2+}\right][OH\cdot] \quad \text{Eq. (S4)}$$

$$[OH\cdot] = \frac{k_4\left[Fe(H_2O)_6{}^{2+}\right][H_2O_2]}{k_5[DMSO]+k_6\left[Fe(H_2O)_6{}^{2+}\right]} \quad \text{Eq. (S5)}$$

$$0 = \frac{d[Fe(IV)]}{dt} = k_7[Fe(H_2O)_5OH^+][H_2O_2] - k_8[Fe(IV)][DMSO] - k_9[Fe(IV)][Fe(II)] \quad \text{Eq. (S6)}$$

$$[Fe(IV)] = \frac{k_7[Fe(H_2O)_5OH^+][H_2O_2]}{k_8[DMSO]+k_9[Fe(II)]} \quad \text{Eq. (S7)}$$

Eqs. (S5) and (S7) are substituted into the formation rate of Fe(III) in Eq. (S1) to yield,

$$\frac{d[Fe(III)]}{dt} = k_4\left[Fe(H_2O)_6{}^{2+}\right][H_2O_2] + k_6\left[Fe(H_2O)_6{}^{2+}\right]\frac{k_4\left[Fe(H_2O)_6{}^{2+}\right][H_2O_2]}{k_5[DMSO]+k_6\left[Fe(H_2O)_6{}^{2+}\right]} + 2k_9\frac{k_7\left[Fe(H_2O)_5OH^+\right][H_2O_2]}{k_8[DMSO]+k_9[Fe(II)]_{\_}}[Fe(II)] \quad \text{Eq. (S8)}$$

To arrive at the expression for k_{obs} reported in Bataineh *et al.*,[21] we need to assume no iron speciation,

$$\left[Fe(H_2O)_6{}^{2+}\right] = [Fe(H_2O)_5OH^+] \equiv [Fe(II)] \quad \text{Eq. (S9)}$$

which yields,

$$\frac{d[Fe(III)]}{dt} = k_4[Fe(II)][H_2O_2] + k_6[Fe(II)]\frac{k_4[Fe(II)][H_2O_2]}{k_5[DMSO]+k_6[Fe(II)]} + 2k_9\frac{k_7[Fe(II)][H_2O_2]}{k_8[DMSO]+k_9[Fe(II)]}[Fe(II)] \quad \text{Eq. (S10)}$$

Dividing Eq. (S10) by $[Fe(II)][H_2O_2]$,

$$k_{obs} = k_4 + k_6\frac{k_4[Fe(II)]}{k_5[DMSO]+k_6[Fe(II)]} + 2k_9\frac{k_7[Fe(II)]}{k_8[DMSO]+k_9[Fe(II)]} \quad \text{Eq. (S11)}$$

Eq. (S10) is identical to Eq. 10 in Bataineh *et al*.[21], which provides additional support that iron speciation is neglected in their original analysis.

4.6. Section S3: RM Model with Iron Speciation and Faster Fe(IV) Formation Rate

RM model predictions with iron speciation and a faster formation rate of Fe(IV) (*i.e.*, $k_7 = 1.4 \times 10^6 M^{-1}s^{-1}$) are shown in Figure 4.S3 for pH = 6 and in Figure 4.S4 for pH = 7.

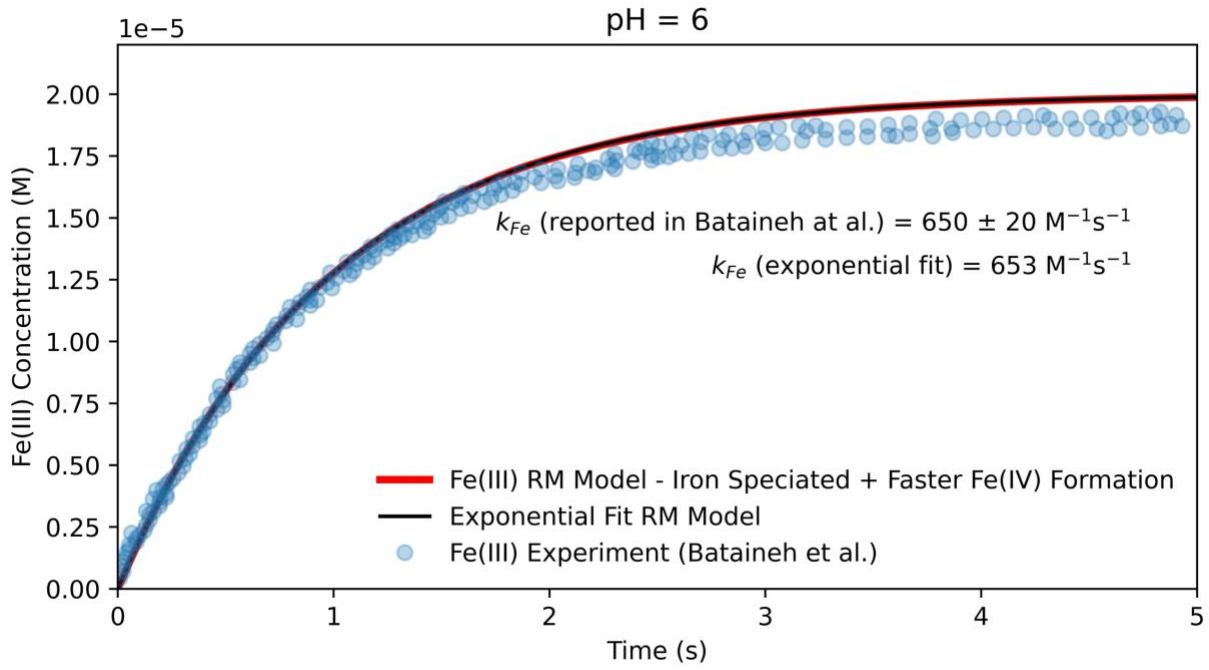

Figure 4.S3 – Fe(III) concentration as a function of time for the RM model with iron speciation and faster Fe(IV) formation rate for pH = 6.2 (red) and experimental data (blue) reproduced from Figure 4.S6 in the Supplementary Information of Bataineh *et al*.[21] Concentrations are obtained from absorbances using the extinction coefficient $2650 \pm 50 M^{-1} cm^{-1}$ and 1 cm path length reported in Ref. [21]. Experimental conditions: 0.02mM Fe(II), 0.78mM H_2O_2, pH 6.2 (buffered by 0.56mM MES).

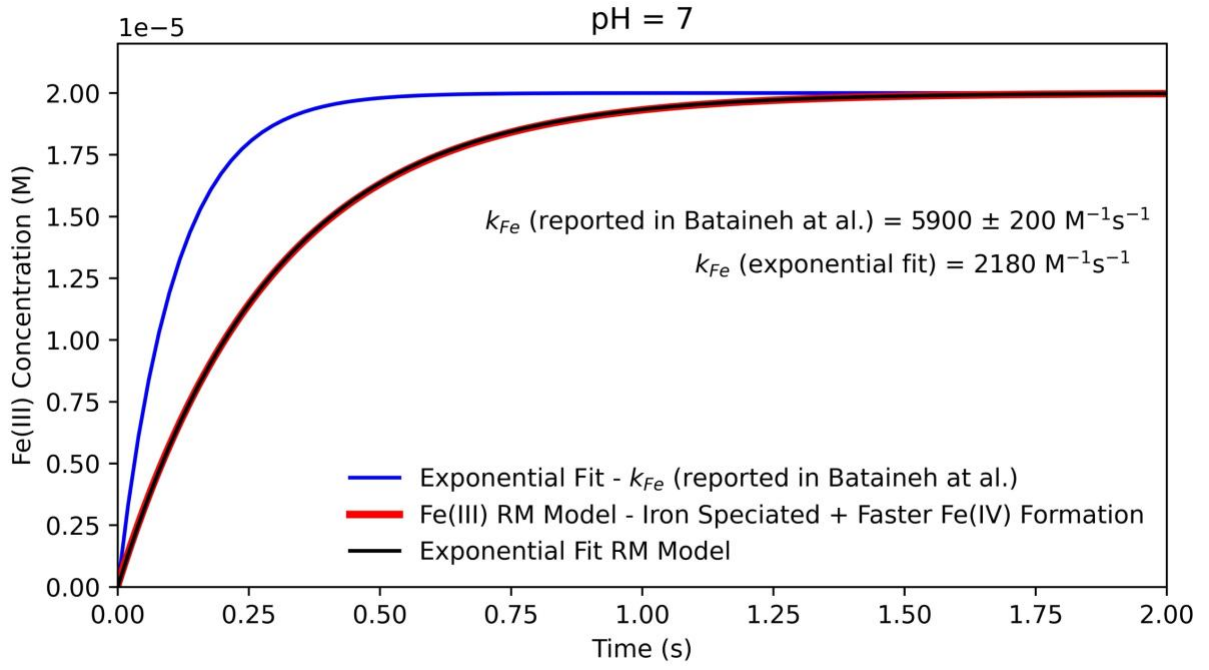

Figure 4.S4 – Fe(III) concentration as a function of time for the RM model with iron speciation and faster Fe(IV) formation rate for pH=7 is shown in red, an exponential fit using the rates reported by Bataineh *et al*.[21] is shown in blue.

There is reasonable agreement between the experimental result and the RM model at pH=6 since the formation rate of Fe(IV) was adjusted to match these conditions, yet extending the model to pH = 7 produces a reaction rate that is about a factor of 3 too slow.

4.6. Section S4: Extracting k_{Fe} from the Experimental Traces of Bataineh et al.

Figure 4.S5 replicates the data shown in the Supplementary Information (Fig. S6) of Bataineh et. al.[21]

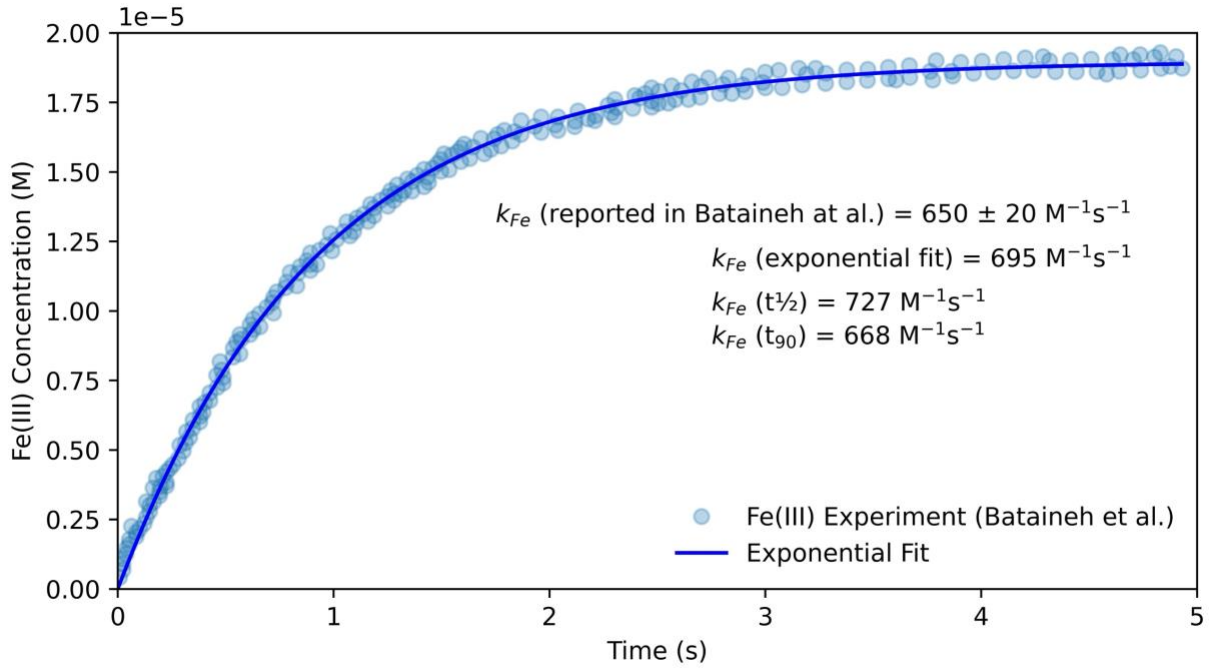

Figure 4.S5 – Experimental data (blue circles) reproduced from Fig. S6 in the Supplementary Information of Bataineh et al[21] and converted to Fe(III) concentration using the extinction coefficient $2650 \pm 50 M^{-1}cm^{-1}$ and 1 cm path length reported in Ref. [21], Experimental conditions: 0.02mM Fe(II), 0.78mM, H_2O_2, and pH 6.2 (buffered by 0.56mM MES). Extraction of the pseudo-first order rate of iron oxidation from the experimental trace is shown using an exponential fit, half-life analysis, and 90% conversion.

The digitized absorbance trace is converted into concentration using the extinction coefficient of $2650 \pm 50 M^{-1}cm^{-1}$ and 1 cm path length reported by Bataineh *et al.*[21] Complete conversion of the initial Fe(II) concentration should form [Fe(III)] $= 2 \times 10^{-5} M$, yet only $1.9 \times 10^{-5} M$ is recovered. Additionally, the authors state that although the solutions were buffered, there was a pH decrease of 0.2 pH units, suggesting that the experimental error in Ref. [21] is likely underestimated. Extraction from the kinetic trace of k_{Fe}, the Fenton reaction rate when H_2O_2 is in excess is shown using an exponential fit, half-life analysis, and 90% conversion. We perform this analysis to better compare the experimental results to our unified model predictions shown in Figure 4.4.4 in the main text and Section S7. Each method emphasizes a different region of the kinetic trace, providing insight into early, average, and late-stage kinetics, where differences among the extracted values arise from non-ideal pseudo first order behavior. The computed Fenton reaction rate has a trend of $k_{Fe_{t^1/_2}} > k_{Fe_{exp}} > k_{Fe_{t_{90}}}$, indicating faster reaction kinetics at early times. We follow the procedure of Ref. [21] to report k_{Fe} as $k_{Fe_{exp}}$, and we calculate the error in

estimating k_{Fe} from the different extraction methods as the largest difference between the exponential fit and the other methods. In Figure 4.S5 $k_{Fe} = 695 \pm 32 M^{-1}s^{-1}$, this values is both larger than the one reported by Bataineh *et al.*[21] and lies outside the reported experimental error. Pointing again to underestimation of the experimental error. An exponential fit incorporating a dead time correction gives $\tau \sim 0.03s$, this would be insignificant for a reaction time scale of about 4 seconds like in Figure 4.S5, but contributing for a faster kinetic trace, like that of pH=7. Unfortunately, no experimental traces are provided for pH=7.

A faster kinetic trace is available for the reaction buffered with phosphate. Digitizing the kinetic trace provided in Bataineh's Supplementary Information (Fig. S12)[21] is presented in Figure 4.S6.

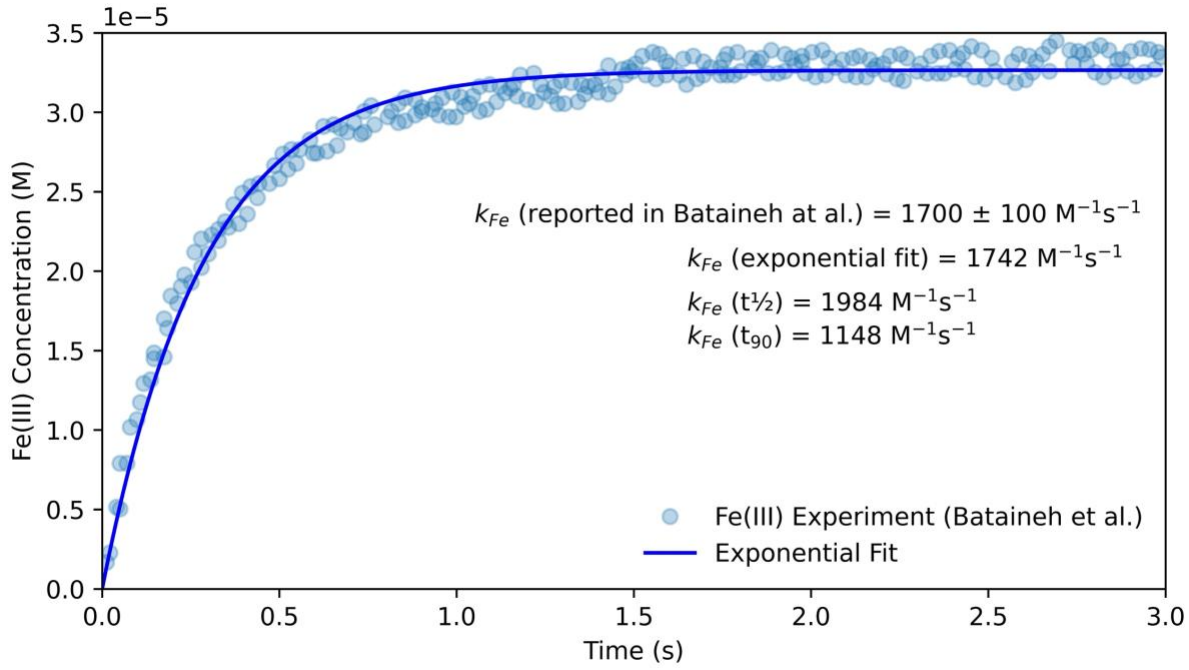

Figure 4.S6– Experimental data (blue circles) reproduced from Figure 4.S12 in the Supplementary Information of Bataineh et al[21] and converted to Fe(III) concentration using the extinction coefficient of $2650 \pm 50 M^{-1}cm^{-1}$ and 1 cm path length reported in Ref. [21], Experimental Conditions: 0.031 mM Fe(II), 1.0 mM H_2O_2, pH 6.1 with 0.6 mM phosphate buffer. Extraction of the pseudo-first order rate of iron oxidation from the experimental trace is shown using an exponential fit, half-life analysis, and 90% conversion.

The exponential fit of the Fe(III) formation rate for Fenton chemistry conducted in phosphate buffers is within the stated experimental error provided by Bataineh *et al.*[21], and exhibits faster kinetics than in non-coordinating buffers (Figure 4.S5). This acceleration has been hypothesized by theory work by Chen to occur due to ligand coordination of phosphate and Fe(III).[53] Analysis of different extraction methods, similarly to Figure 4.S3, shows a trend of $k_{Fe_{t^1/_2}} > k_{Fe_{exp}} > k_{Fe_{t_{90}}}$ pointing to faster initial kinetics that get slower as the reaction proceeds, the uncertainty in the fit is quite large when the overall reaction is faster and yields $k_{Fe} = 1742 \pm 552 M^{-1}s^{-1}$, meaning that there is already significant divergence from pseudo first order kinetics. Complete conversion should yield 0.031mM, yet in this case, we recover more iron than

expected (final value from exponential fit is 0.033mM with individual data points above this concentration). These results suggest again that the experimental error is likely larger than appreciated. At pH=7, k_{Fe} is more than three times higher than in Figure 4.S6, implying that such uncertainties would become even more pronounced at higher pH conditions.

Independently of the experimental error, a more significant concern arises from the use of fixed-wavelength absorbance at 270nm. Figure 4.S7 shows the extinction coefficient or molar absorptivity of Fe(III) species in water.

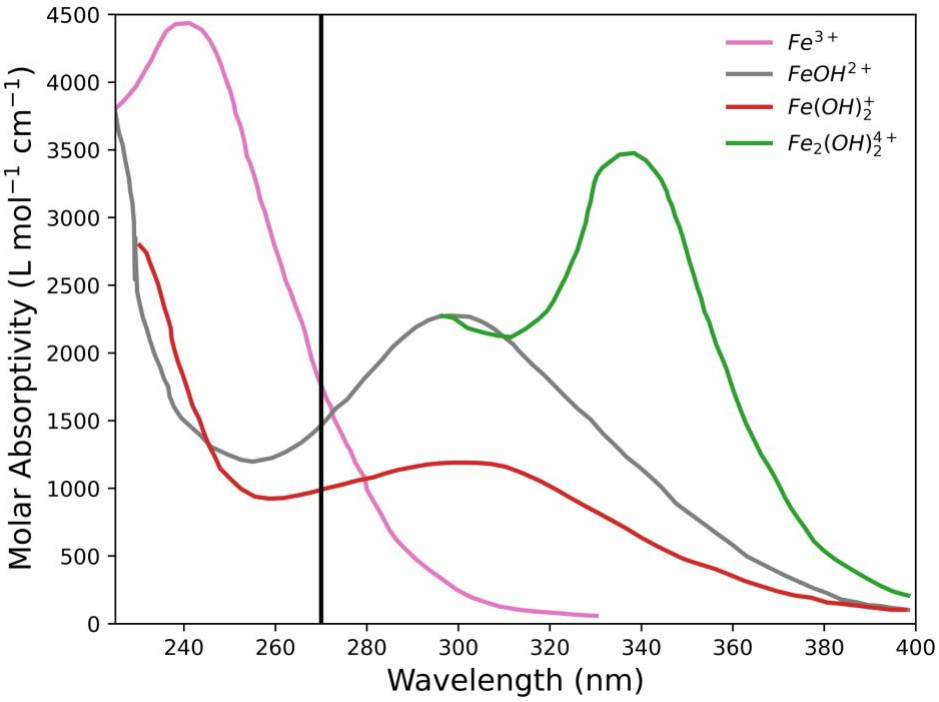

Figure 4.S7– Molar absorptivity of Fe(III) species in water as a function of wavelength reproduced from Fig. 2 in ref [54] similar results shown in Fig 1. and Fig 2. of ref [38] note that $Fe_2(OH)_2^{4+}$ spectrum extends into the UV with very large molar absorptivity values. The single wavelength used to probe the reaction kinetics in Bataineh et al. is shown as a black line at 270nm.

Figure 4.S7 reveals that extracting the formation kinetics of Fe(III) using a single wavelength is likely semi-quantitative, especially with varying pH conditions that largely effect the speciation (see Sanez *et al.*[35] Fig. 2, Remucal and Sedlak[20] Fig. 3, for Fe(III) speciation as a function of pH -slight changes depend on exact thermodynamic equilibria values used and treatment of ferrihydrite). This is not to suggest that the experimental results from Bataineh *et al.*[21] are unreliable, but rather that the use of a single wavelength can only be interpreted as a reaction clock- a flat absorbance signal indicates the reaction has reached completion, but does not necessarily provide a fully quantitative measure of total Fe(III) formation, as speciation evolves throughout the reaction timescale and varies with pH. In that sense, it might be more appropriate to evaluate the pseudo first order rate from conversion times, *i.e.* from $k_{Fe_{t_{90}}}$. Using the 90% conversion point would yield a lower calculated experimental k_{Fe} and a larger one predicted from our kinetic model simulations that appear in the following SI Section S7. Yet, to keep a conservative comparison between the experiment and model we compute k_{Fe} as an exponential

fit as this is the method that was used by Bataineh *et al*.[21]. This comparison is presented in Figure 4.4.4 of the main text.

4.6. Section S5: Unified Kinetic Model - Implementation

The kinetic model detailed in Table 4. 1 of the main text proposes a mechanism that includes both radical and Fe(IV) oxidation in a unified framework. Equilibrium constants for reactions M2 and M15 were modified from reference to ensure compliance with Wegscheider's condition and internal consistency of the model reaction loops. M2 is the first acid dissociation of Fe(III) - $Fe^{3+} + H_2O \rightleftharpoons Fe(OH)^{2+} + H^+$. A range of values from $2 - 7 \times 10^{-3}$M appears in the literature depending on experimental technique and ionic strength[32,37]. In the original Scheme 3 from Stanbury[32] an equilibrium constant value of 2×10^{-3}M is used. To ensure internal consistency in the model and compliance with Wegscheider's condition, the overall equilibrium product of net zero reaction loops should not deviate substantially from unity. These loops are closed sets of reactions that return to the original chemical state and serve as a test for thermodynamic consistency within the model.

The first loop (L1) in the mechanism includes the net zero reaction of M1 + M2 − M3 − M4 + M13 + M14. Computing the overall equilibrium of the net reaction loop results in K=0.97, a reasonable value deviating 3% from unity, when using an equilibrium constant of 4×10^{-3}M for reaction M2. Keeping the original equilibrium value at 2×10^{-3}M would have halved the overall K of loop 1 resulting in violation of Wegscheider's condition.

M15 is the reaction of hydrogen peroxide with the second acid dissociation species of Fe(III) - $Fe(OH)^{2+} + H_2O_2 \rightleftharpoons Fe_3(OH)(HO_2)^{2+} + H^+$. This reaction has a very small equilibrium constant and did not affect the overall kinetics or speciation of the model predictions, still it is included for completeness. A literature equilibrium constant given in ref [32] is 2.2×10^{-12}. The second net zero loop in the mechanism is L2: −M1 − M3 − M4 + M11 + M15. The equilibrium constant of M15 was slightly reduced to 1.2×10^{-12} to provide an overall equilibrium product for L2 of K=0.97. The last loop in the mechanism is L3: M1 + M2 − M3 − M4 − M17 + M18. Wegscheider's condition for this loop is maintained with a net L3 equilibrium product of K=0.99. The overall mechanism does not produce a net zero reaction loop whose overall equilibrium constant deviates by more than 5% from unity. Enforcing consistent cycling of species when propagating the reaction kinetics in our unified model.

The unified Fenton chemistry kinetic model was implemented in Kinetiscope[33]. pH-dependent model predictions were examined in the kinetic scheme by holding the $[H^+]$ concentration constant, *i.e.* assuming a buffered solution. Formation of OH^- is neglected as well as cycling of water molecules.

4.6. Section S6: Unified Kinetic Model - Faster Equilibrium of the Second Acid Dissociation of Fe(III)

In the first iteration of the kinetic model (Table 4. 1), a diffusion limited termolecular rate was applied to the reverse rate of M11, the second acid dissociation of Fe(III) - $Fe^{3+} + 2\,H_2O \rightleftharpoons Fe(OH)_2{}^{+} + 2\,H^+$, in the absence of measured kinetic data. A check of the equilibration time scales starting from Fe^{3+} was examined at pH=7 in Figure 4.S8.

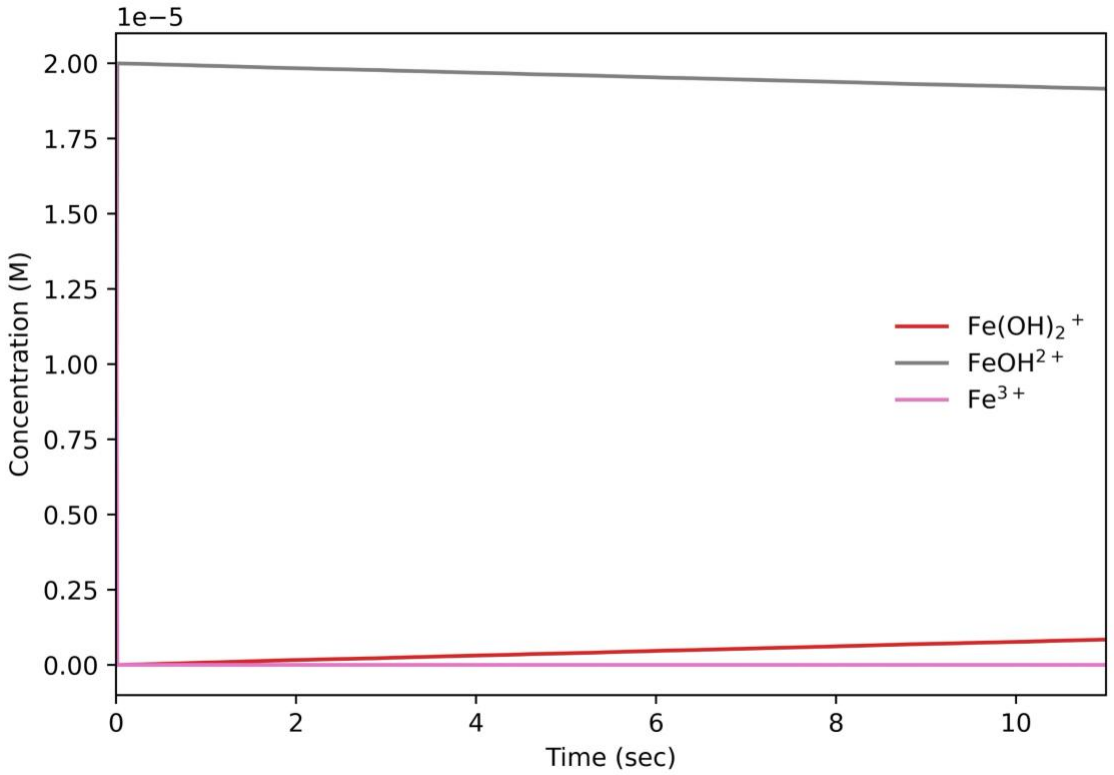

Figure 4.S8 – Fe(III) species concentration as a function of time starting from 2×10^{-5}M Fe^{3+} at pH=7 when the second acid dissociation reverse rate is $k_{M11-r} = 10^{7}\mathrm{M}^{-2}\mathrm{s}^{-1}$

Over the course of 10 seconds, which is longer than the time scale for the reaction at this pH=7, Fe^{3+} converts quickly to $Fe(OH)^{2+}$ and slowly approaches its equilibrium with $Fe(OH)_2{}^{+}$. This timescale to achieve acid-base equilibrium seems too long to be valid so a bimolecular rate was used for the reverse rate of M11. Figure 4.S9 shows equilibrium establishment time scales at pH=7 when $k_{M11-r} = 10^{10}\mathrm{M}^{-2}\mathrm{s}^{-1}$.

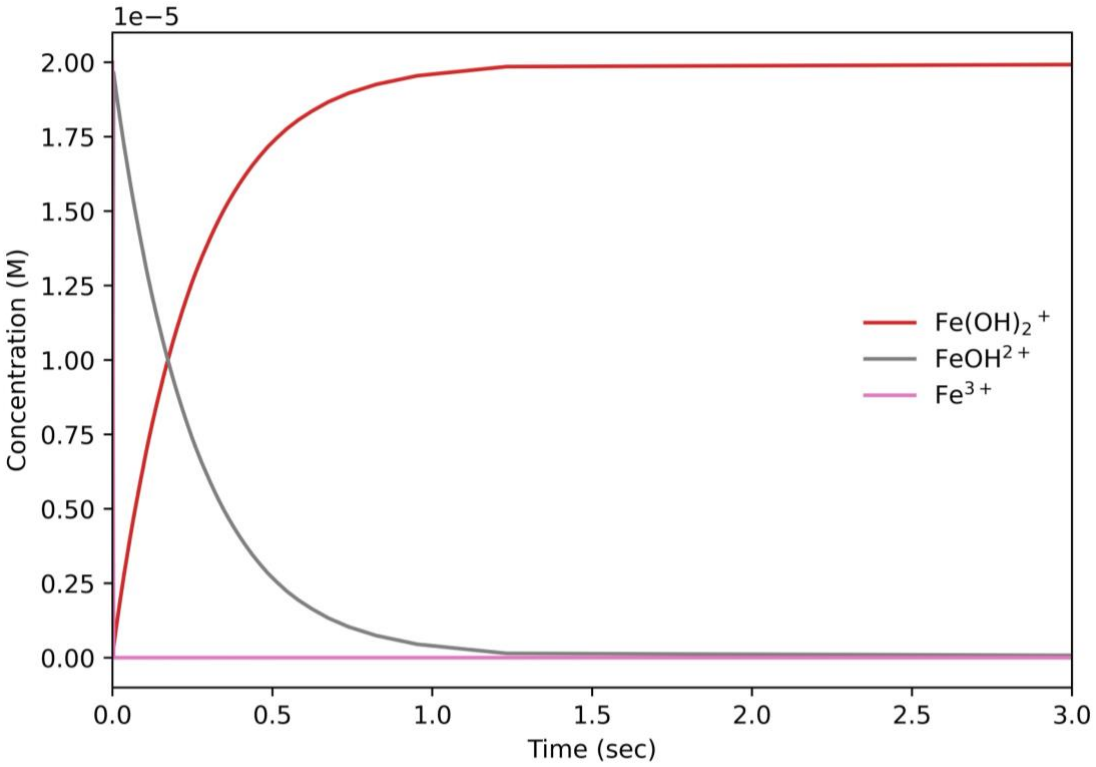

Figure 4.S9 – Fe(III) species' concentration as a function of time starting from $2 \times 10^{-5} M\ Fe^{3+}$ at pH=7 when the second acid dissociation reverse rate is set to $k_{M11-r} = 10^{10} M^{-2} s^{-1}$

The equilibrium in Figure 4.S9 is established over the course of ~1 s, which appears more reasonable. Yet, it is possible that in fact this equilibrium is established over a longer time scale. The kinetic speciation of Fe(III) species predicted by the model using these two reaction rates for the reverse reaction appear in Figure 4.S10 and S11. Little to no effect was observed for the overall Fenton reaction kinetics.

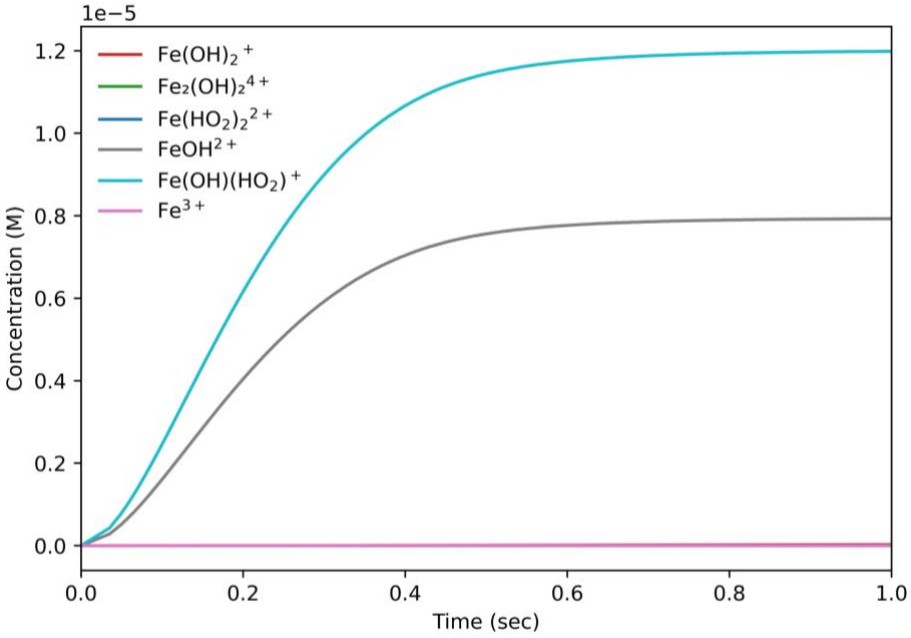

Figure 4.S10 – Fe(III) species concentration as a function of time starting from 2×10^{-5}M Fe^{2+} and 0.78×10^{-3}M of H_2O_2 at pH=7 when the second acid dissociation reverse rate is $k_{M11-r} = 10^{7}\mathrm{M}^{-2}\mathrm{s}^{-1}$.

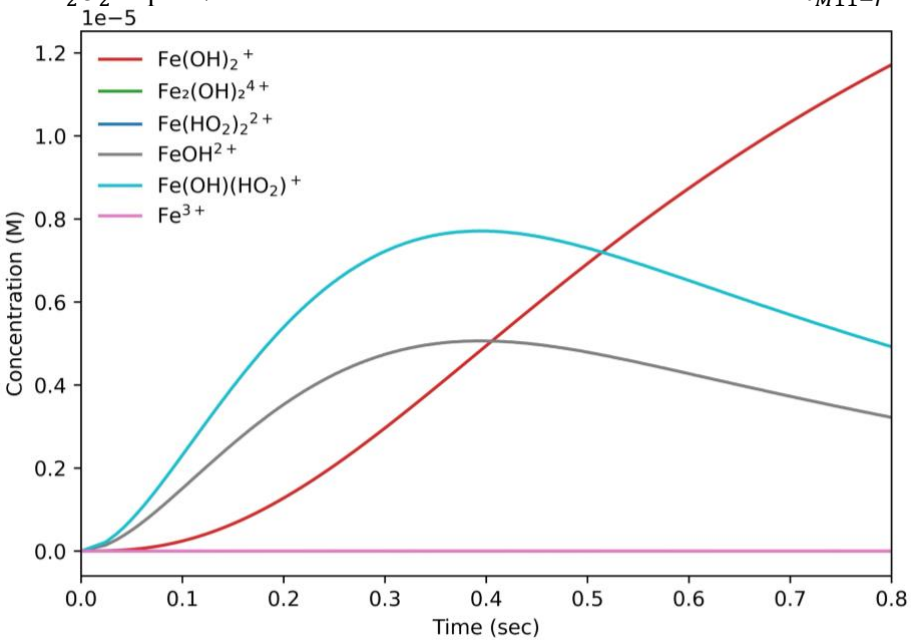

Figure 4.S11 – Fe(III) species concentration as a function of time starting from 2×10^{-5}M Fe^{2+} and 0.78×10^{-3}M of H_2O_2 at pH=7 when the second acid dissociation reverse rate is $k_{M11-r} = 10^{10}\mathrm{M}^{-2}\mathrm{s}^{-1}$.

Section S7: Unified Kinetic Model – Model Predictions and Exponential Fit Uncertainty

Unified kinetic model traces for the formation of Fe(III) and the decay of Fe(II) species are shown in figures S12-S15, for a variety of buffered pH conditions. To compare our unified kinetic model with the experimental results of Bataineh et al.[1], we extract the pseudo–first-order rate constant k_{Fe} with excess of H_2O_2, from the model predictions, using three methods: exponential fitting, half-life analysis, and 90% conversion. Each method emphasizes a different part of the kinetic trace, corresponding to early, average, or late reaction times, and helps assess potential deviations from ideal pseudo–first-order behavior. The extracted values are used in Figure 4.4.4 of the main text comparing model predictions to the experimental results. Because the model involves multiple Fe(II) and Fe(III) species contributing to the overall kinetics, especially as the Fenton reaction accelerates with the increase in pH- no single extraction method fully captures the kinetic behavior. We report k_{Fe} based on the exponential fit for consistency with the approach used in the original experimental study, while also including the other two values to illustrate the range of kinetic behavior and associated uncertainty.

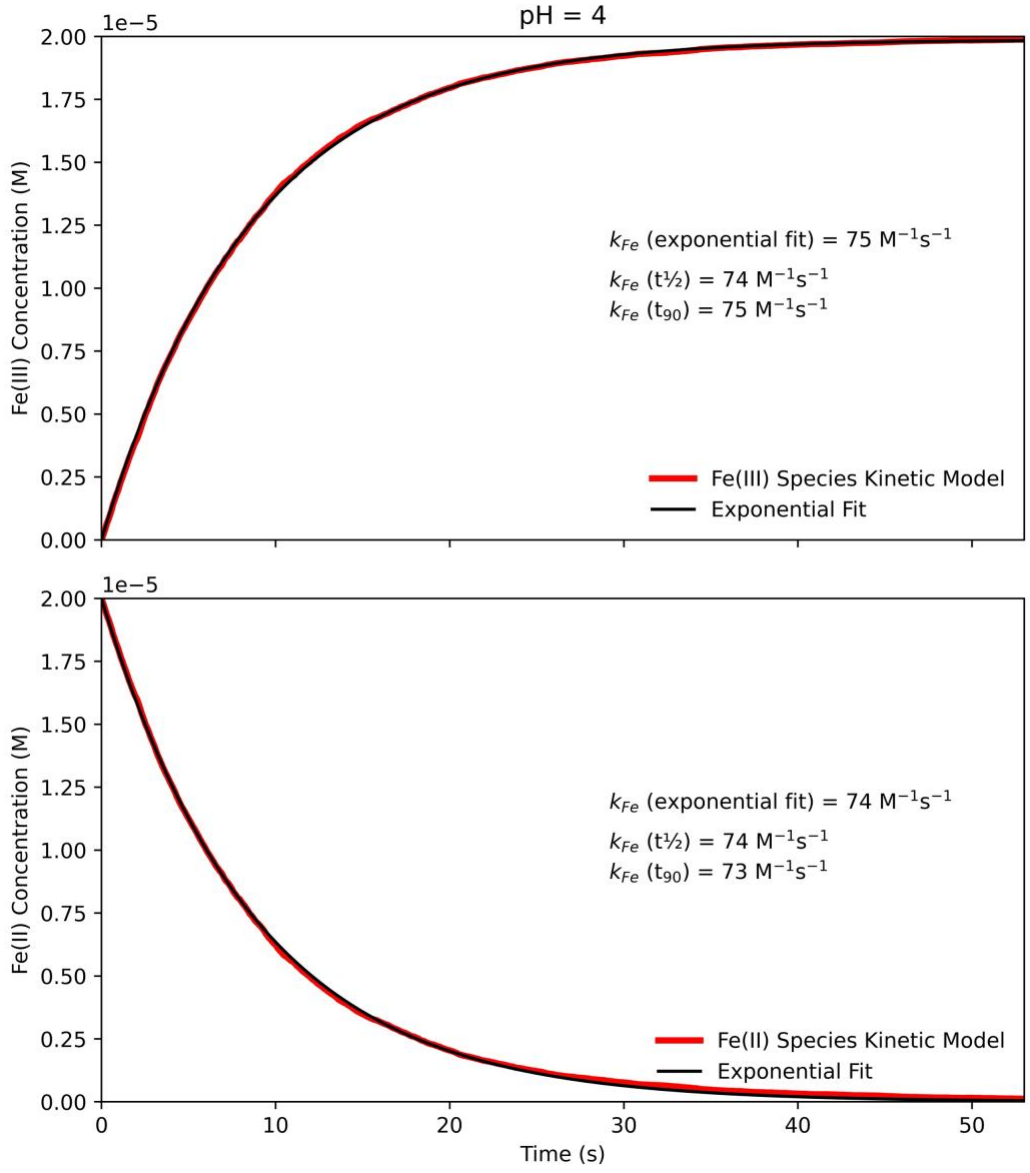

Figure 4.S12 – Fe(III) and Fe(II) total species concentration as a function of time, starting from equilibrated speciation of Fe(II) at a total concentration of 2×10^{-5}M, and 0.78×10^{-3}M H_2O_2 at pH=4.

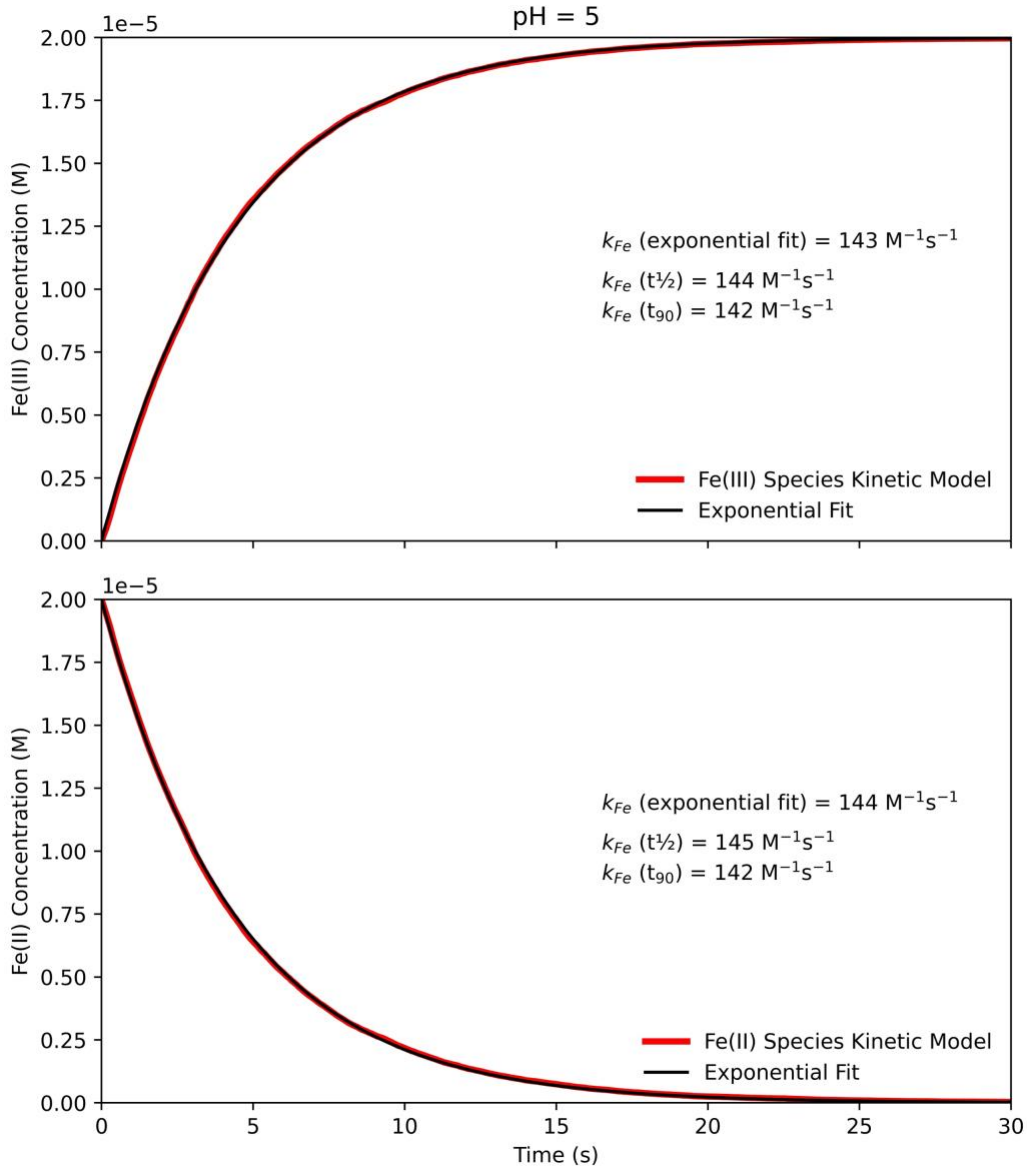

Figure 4.S13 – Fe(III) and Fe(II) total species concentration as a function of time, starting from equilibrated speciation of Fe(II) at a total concentration of 2×10^{-5}M, and 0.78×10^{-3}M H_2O_2 at pH=5.

Figures S12 and S13 show that pH ≤ 5, when the overall reaction kinetics are still comparatively slow, there is no noticeable difference between the different extraction methods and pseudo first order behavior is preserved.

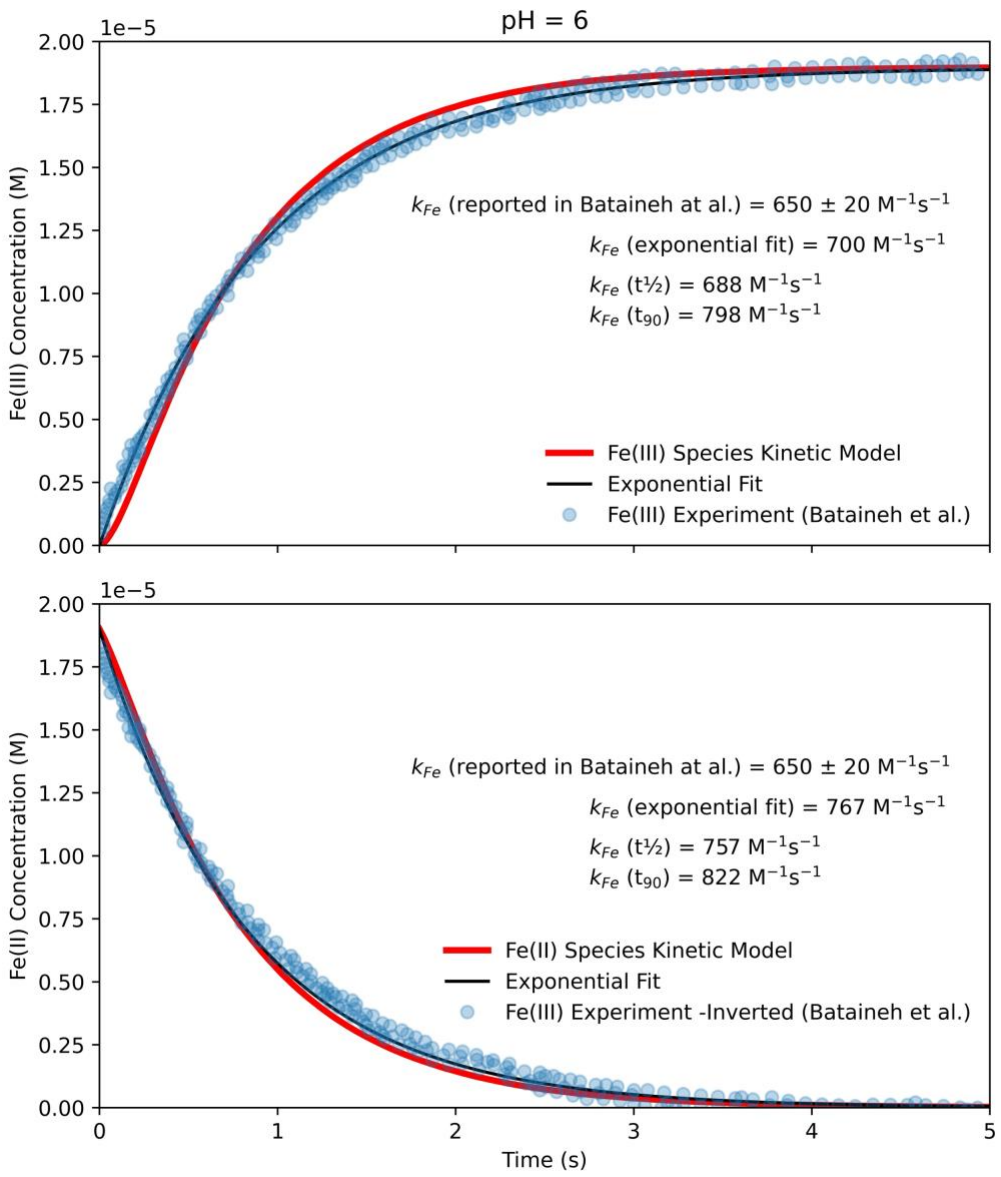

Figure 4.S14 – Fe(III) and Fe(II) total species concentration as a function of time, starting from equilibrated speciation of Fe(II) at a total concentration of 1.9×10^{-5}M, and $0.78 \times 10^{-3} M\ H_2O_2$ at pH=6. Overlayed with experimental data (blue circles) reproduced from Figure 4.S6 in the Supplementary Information of Bataineh *et al.*[21] Absorbance values were converted to concentration using the extinction coefficient provided in the paper of $2650 \pm 50 \mathrm{M^{-1}cm^{-1}}$, Experimental conditions: 0.02mM Fe(II), 0.78mM H_2O_2, pH 6.2 (buffered by 0.56mM MES). Iron initial concentration was reduced to 1.9×10^{-5}M to assist in inspecting the comparison.

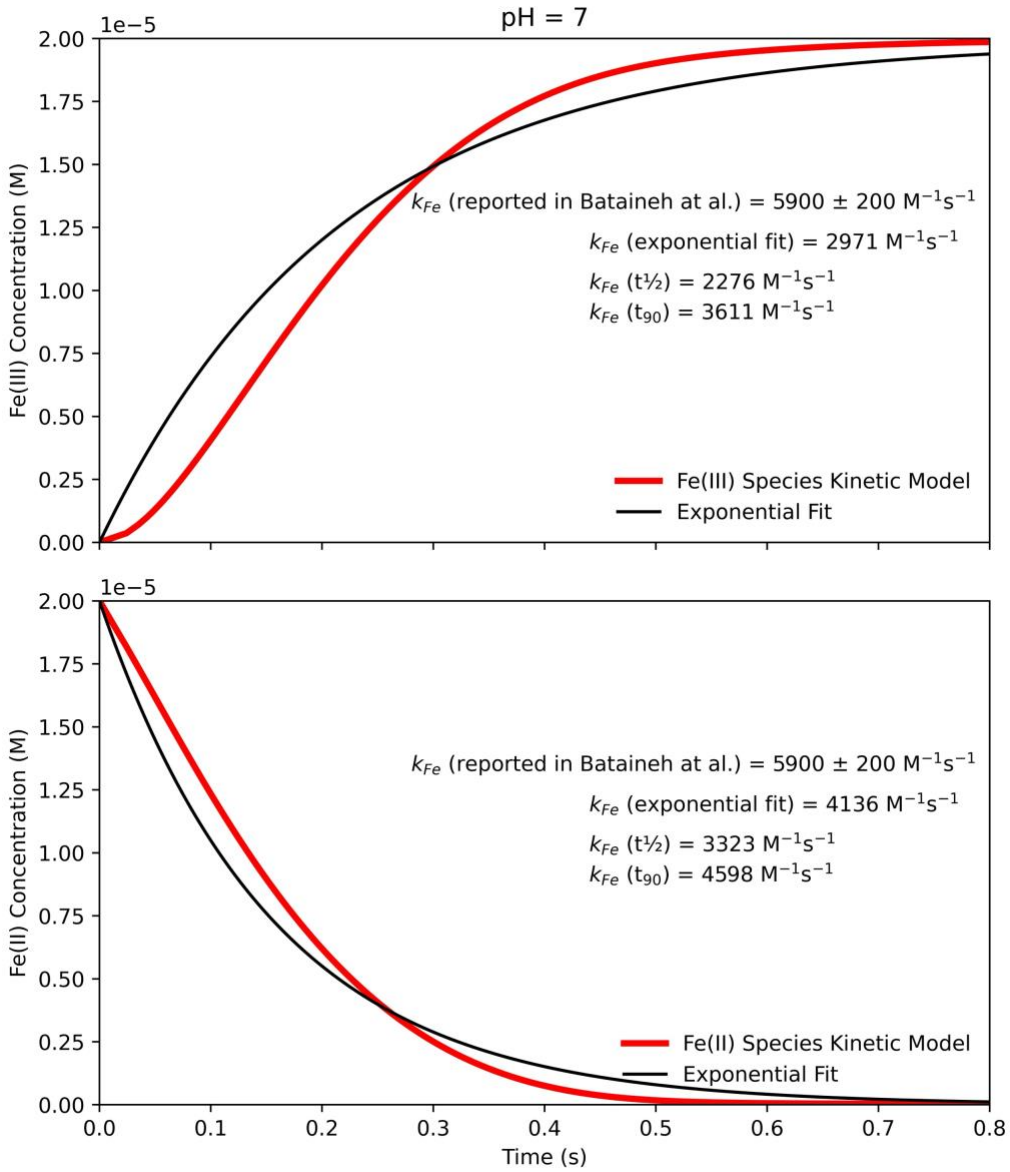

Figure 4.S15 – Fe(III) and Fe(II) total species concentration as a function of time, starting from equilibrated speciation of Fe(II) at a total concentration of $2 \times 10^{-5} M$, and $0.78 \times 10^{-3} M$ H_2O_2 at pH=7.

As pH increases and the observed kinetics become faster, the uncertainty in estimating the pseudo first order using a single exponential fit also increases (Figures S14 and S15). The value of k_{Fe} shown in Figure 4.4.4 of the main text is calculated as the average of Fe(II) and Fe(III) rates obtained from exponential fits. As discussed in Section S4, this approach likely underestimates of the kinetics, particularly at pH=7. However, since no experimental kinetic traces are available from Bataineh for pH values other than 6, we have no other direct way to compare model predictions with the experimental result.

At pH ≥ 6, we observe the trend $k_{Fe_{t_{90}}} > k_{Fe_{exp}} > k_{Fe_{t^1/_2}}$, which suggests that the kinetics are initially faster and slow down over the course of the reaction, showing a characteristic

induction time. It will be interesting to explore if this can be measured experimentally and perhaps assist in constraining the kinetics of some of the equilibrium constants forward and reverse rates.

To estimate the error in fitting the model predictions, we use the largest difference between the k_{Fe} extracted from exponential fit and one of the other metrics. We also note that there is non-negligible uncertainty in extracting rates from the experimental results themselves (Section S4). At pH=6 there is good agreement between the experiment and the model predictions, and the experimental result is within the uncertainty of the average value predicted by the kinetic model.

4.6. Section S8: Probing Kinetic Feasibility of $Fe(OH)^{2+}$ as a forming reagent to Fe(IV)

We used the unified kinetic model to test a theoretical prediction by Lu et al.[52] that the pH dependent mechanism of Fenton chemistry proceeds at pH < 7.7 through a reaction of water coordinated $Fe(OH)^{2+}$ (i.e. $(H_2O)_5Fe^{III}(OH)^{2+}$ in their notation) with an OH radical to produce Fe(IV). Modifying the kinetic model presented in Table 4. 1 of the main text, reaction M20 is now changed from $Fe(OH)^{+} + H_2O_2 \rightarrow FeO^{2+} + H_2O + OH^{-}$ to $Fe(OH)^{2+} + \cdot OH \rightarrow FeO^{2+} + H_2O$ $k_{M20} = 10^{10}\mathrm{M}^{-1}s^{-1}$. A diffusion limited rate is assumed as an upper kinetic upper limit. Additionally, building on the analysis presented in Section S6, we reduced the reverse rate of the Fe(III) second acid dissociation equilibrium back to a termolecular limit - $k_{M11-r} = 10^{7}M^{-2}s^{-1}$ to drive early kinetic speciation of Fe(III) as $Fe(OH)^{2+}$ instead of $Fe(OH)_2^{+}$. The model predictions and experimental results is shown in Figure 4.S16.

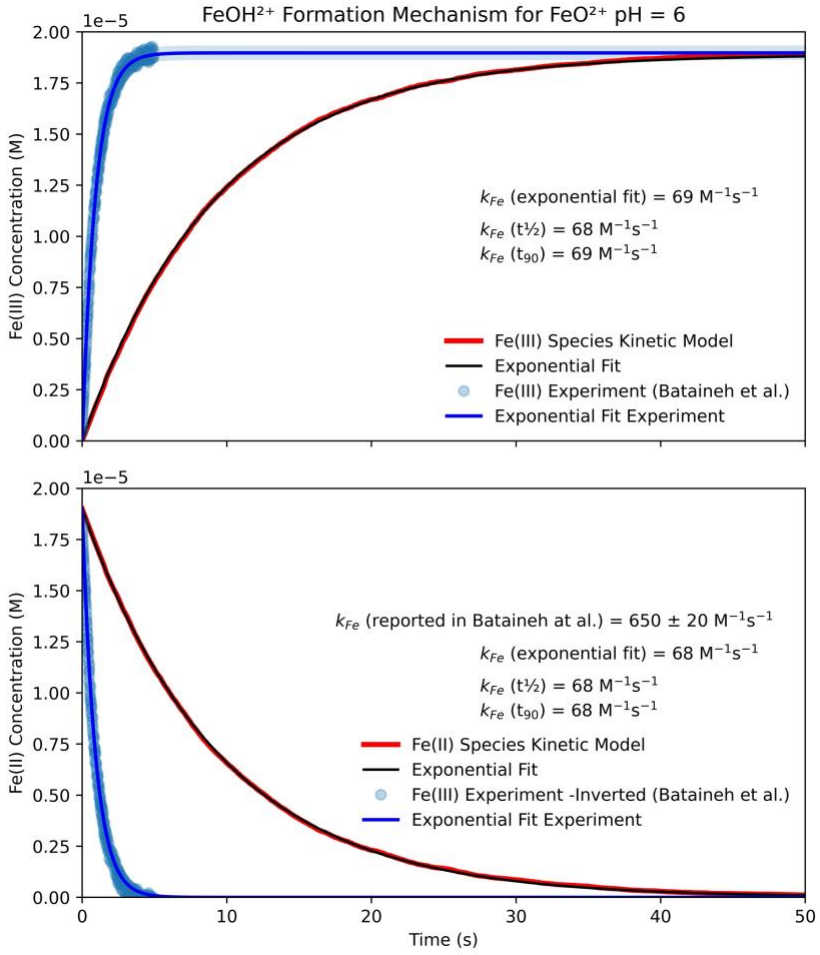

Figure 4.S16 – Fe(III) and Fe(II) total species concentration as a function of time, starting from equilibrated speciation of Fe(II) at a total concentration of 1.9×10^{-5}M, and 0.78×10^{-3}M H_2O_2 at pH=6 testing $Fe(OH)^{2+}$ as the precursor to Fe(IV) formation. Overlayed with experimental data (blue circles) reproduced from Figure 4.S6 in the Supplementary Information of Bataineh *et al*[21]. Absorbance values were converted to concentration using the extinction coefficient provided in the paper of $2650 \pm 50\mathrm{M}^{-1}\mathrm{cm}^{-1}$, Experimental conditions: 0.02mM Fe(II), 0.78mM H_2O_2, pH 6.2 (buffered by 0.56mM MES). Iron initial concentration was reduced to 1.9×10^{-5}M to assist in inspecting the comparison.

The comparison between the model testing the Fe(IV) formation mechanism from $Fe(OH)^{2+}$ and the experimental results shows significant discrepancy, even when we further tested extreme assumptions designed to favor this pathway. Specifically, we tried using rates that were orders of magnitude faster than diffusion limited, forcing all OH radicals formed to react through this pathway and removing all possible sinks for $Fe(OH)^{2+}$, had little to no influence on the predictions shown in Figure 4.4.16 which are already set up to reflect a kinetic upper limit. This is because this pathway depends on the initial reaction of Fe(II) with H_2O_2 to produce a radical species, which is rather slow. This analysis makes a kinetic prediction that Fe(IV) formation through this pathway, while energetically favorable, is likely not the primary explanation of the pH dependent kinetics observed for Fenton chemistry.

4.7. References

(1) Fenton, H. J. H. LXXIII.—Oxidation of Tartaric Acid in Presence of Iron. *J. Chem. Soc. Trans.* **1894**, *65* (0), 899–910. https://doi.org/10.1039/CT8946500899.

(2) Prousek, J. Fenton Chemistry in Biology and Medicine. *Pure Appl. Chem.* **2007**. https://doi.org/10.1351/pac200779122325.

(3) Deguillaume, L.; Leriche, M.; Chaumerliac, N. Impact of Radical versus Non-Radical Pathway in the Fenton Chemistry on the Iron Redox Cycle in Clouds. *Chemosphere* **2005**, *60* (5), 718–724. https://doi.org/10.1016/j.chemosphere.2005.03.052.

(4) A. Al-Abadleh, H. Review of the Bulk and Surface Chemistry of Iron in Atmospherically Relevant Systems Containing Humic-like Substances. *RSC Adv.* **2015**, *5* (57), 45785–45811. https://doi.org/10.1039/C5RA03132J.

(5) Siefert, R. L.; Pehkonen, S. O.; Erel, Y.; Hoffmann, M. R. Iron Photochemistry of Aqueous Suspensions of Ambient Aerosol with Added Organic Acids. *Geochim. Cosmochim. Acta* **1994**, *58* (15), 3271–3279. https://doi.org/10.1016/0016-7037(94)90055-8.

(6) Hems, R. F.; Hsieh, J. S.; Slodki, M. A.; Zhou, S.; Abbatt, J. P. D. Suppression of OH Generation from the Photo-Fenton Reaction in the Presence of α-Pinene Secondary Organic Aerosol Material. *Environ. Sci. Technol. Lett.* **2017**, *4* (10), 439–443. https://doi.org/10.1021/acs.estlett.7b00381.

(7) Pignatello, J. J.; Oliveros, E.; MacKay, A. Advanced Oxidation Processes for Organic Contaminant Destruction Based on the Fenton Reaction and Related Chemistry. *Crit. Rev. Environ. Sci. Technol.* **2006**, *36* (1), 1–84. https://doi.org/10.1080/10643380500326564.

(8) Bigda, R. J. Consider Fenton`s Chemistry for Wastewater Treatment. *Chem. Eng. Prog.* **1995**, *91* (12).

(9) Babuponnusami, A.; Muthukumar, K. A Review on Fenton and Improvements to the Fenton Process for Wastewater Treatment. *J. Environ. Chem. Eng.* **2014**, *2* (1), 557–572. https://doi.org/10.1016/j.jece.2013.10.011.

(10) Wardman, P.; Candeias, L. P. Fenton Chemistry: An Introduction. *Radiat. Res.* **1996**, *145* (5), 523–531. https://doi.org/10.2307/3579270.

(11) Haber, F.; Weiss, J. The Catalytic Decomposition of Hydrogen Peroxide by Iron Salts. *Proc. R. Soc. Lond. Ser. - Math. Phys. Sci.* **1934**. https://doi.org/10.1098/rspa.1934.0221.

(12) Bray, W. C.; Gorin, M. H. FERRYL ION, A COMPOUND OF TETRAVALENT IRON. *J. Am. Chem. Soc.* **1932**, *54* (5), 2124–2125. https://doi.org/10.1021/ja01344a505.

(13) Walling, C. Fenton's Reagent Revisited. *Acc. Chem. Res.* **1975**, *8* (4), 125–131. https://doi.org/10.1021/ar50088a003.

(14) Croft, S.; Gilbert, B. C.; Smith, J. R. L.; Whitwood, A. C. An E.S.R. Investigation of the Reactive Intermediate Generated in the Reaction Between FeII and H2O2 in Aqueous Solution. Direct Evidence for the Formation of the Hydroxyl Radical. *Free Radic. Res. Commun.* **1992**. https://doi.org/10.3109/10715769209061086.

(15) Sawyer, D. T.; Sobkowiak, A.; Matsushita, T. Metal [MLx; M = Fe, Cu, Co, Mn]/Hydroperoxide-Induced Activation of Dioxygen for the Oxygenation of Hydrocarbons: Oxygenated Fenton Chemistry. *Acc. Chem. Res.* **1996**, *29* (9), 409–416. https://doi.org/10.1021/ar950031c.

(16) Rush, J. D.; Koppenol, W. H. Reactions of Iron(II) Nitrilotriacetate and Iron(II) Ethylenediamine-N,N'-Diacetate Complexes with Hydrogen Peroxide. *J. Am. Chem. Soc.* **1988**, *110* (15), 4957–4963. https://doi.org/10.1021/ja00223a013.

(17) Goldstein, S.; Meyerstein, D.; Czapski, G. The Fenton Reagents. *Free Radic. Biol. Med.* **1993**, *15* (4), 435–445. https://doi.org/10.1016/0891-5849(93)90043-T.
(18) Bossmann, S. H.; Oliveros, E.; Göb, S.; Siegwart, S.; Dahlen, E. P.; Payawan, L.; Straub, M.; Wörner, M.; Braun, A. M. New Evidence against Hydroxyl Radicals as Reactive Intermediates in the Thermal and Photochemically Enhanced Fenton Reactions. *J. Phys. Chem. A* **1998**, *102* (28), 5542–5550. https://doi.org/10.1021/jp980129j.
(19) Hug, S. J.; Leupin, O. Iron-Catalyzed Oxidation of Arsenic(III) by Oxygen and by Hydrogen Peroxide: pH-Dependent Formation of Oxidants in the Fenton Reaction. *Environ. Sci. Technol.* **2003**, *37* (12), 2734–2742. https://doi.org/10.1021/es026208x.
(20) Remucal, C. K.; Sedlak, D. L. The Role of Iron Coordination in the Production of Reactive Oxidants from Ferrous Iron Oxidation by Oxygen and Hydrogen Peroxide. In *ACS Symposium Series*; Tratnyek, P. G., Grundl, T. J., Haderlein, S. B., Eds.; American Chemical Society: Washington, DC, 2011; Vol. 1071, pp 177–197. https://doi.org/10.1021/bk-2011-1071.ch009.
(21) Bataineh, H.; Pestovsky, O.; Bakac, A. pH-Induced Mechanistic Changeover from Hydroxyl Radicals to Iron(IV) in the Fenton Reaction. *Chem. Sci.* **2012**, *3* (5), 1594–1599. https://doi.org/10.1039/C2SC20099F.
(22) Lee, H.; Lee, H.-J.; Sedlak, D. L.; Lee, C. pH-Dependent Reactivity of Oxidants Formed by Iron and Copper-Catalyzed Decomposition of Hydrogen Peroxide. *Chemosphere* **2013**, *92* (6), 652–658. https://doi.org/10.1016/j.chemosphere.2013.01.073.
(23) H. Koppenol, W. Ferryl for Real. The Fenton Reaction near Neutral pH. *Dalton Trans.* **2022**, *51* (45), 17496–17502. https://doi.org/10.1039/D2DT03168J.
(24) Kremer, M. L. Mechanism of the Fenton Reaction. Evidence for a New Intermediate. *Phys. Chem. Chem. Phys.* **1999**, *1* (15), 3595–3605. https://doi.org/10.1039/A903915E.
(25) Buda, F.; Ensing, B.; Gribnau, M. C. M.; Baerends, E. J. DFT Study of the Active Intermediate in the Fenton Reaction. *Chem. – Eur. J.* **2001**, *7* (13), 2775–2783. https://doi.org/10.1002/1521-3765(20010702)7:13<2775::AID-CHEM2775>3.0.CO;2-6.
(26) Ensing, B.; Buda, F.; Blöchl, P.; Baerends, E. J. Chemical Involvement of Solvent Water Molecules in Elementary Steps of the Fenton Oxidation Reaction. *Angew. Chem. Int. Ed.* **2001**, *40* (15), 2893–2895. https://doi.org/10.1002/1521-3773(20010803)40:15<2893::AID-ANIE2893>3.0.CO;2-B.
(27) Ensing, B.; Buda, F.; Blöchl, P. E.; Baerends, E. J. A Car–Parrinello Study of the Formation of Oxidizing Intermediates from Fenton's Reagent in Aqueous Solution. *Phys. Chem. Chem. Phys.* **2002**, *4* (15), 3619–3627. https://doi.org/10.1039/B201864K.
(28) Ensing, B.; Buda, F.; Gribnau, M. C. M.; Baerends, E. J. Methane-to-Methanol Oxidation by the Hydrated Iron(IV) Oxo Species in Aqueous Solution: A Combined DFT and Car−Parrinello Molecular Dynamics Study. *J. Am. Chem. Soc.* **2004**, *126* (13), 4355–4365. https://doi.org/10.1021/ja038865a.
(29) Buxton, G. V.; Greenstock, C. L.; Helman, W. P.; Ross, A. B. Critical Review of Rate Constants for Reactions of Hydrated Electrons, Hydrogen Atoms and Hydroxyl Radicals (·OH/·O− in Aqueous Solution. *J. Phys. Chem. Ref. Data* **1988**, *17* (2), 513–886. https://doi.org/10.1063/1.555805.
(30) Eberhardt, M. K.; Colina, R. The Reaction of OH Radicals with Dimethyl Sulfoxide. A Comparative Study of Fenton's Reagent and the Radiolysis of Aqueous Dimethyl Sulfoxide Solutions. *J. Org. Chem.* **1988**, *53* (5), 1071–1074. https://doi.org/10.1021/jo00240a025.

(31) Pestovsky, O.; Stoian, S.; Bominaar, E. L.; Shan, X.; Münck, E.; Que Jr., L.; Bakac, A. Aqueous FeIV□O: Spectroscopic Identification and Oxo-Group Exchange. *Angew. Chem. Int. Ed.* **2005**, *44* (42), 6871–6874. https://doi.org/10.1002/anie.200502686.
(32) Stanbury, D. M. The Principle of Detailed Balancing, the Iron-Catalyzed Disproportionation of Hydrogen Peroxide, and the Fenton Reaction. *Dalton Trans.* **2022**, *51* (6), 2135–2157. https://doi.org/10.1039/D1DT03645A.
(33) Hinsberg, W.; Houle, F. Kinetiscope. https://hinsberg.net/kinetiscope/ (accessed 2025-03-01).
(34) Barshop, B. A.; Wrenn, R. F.; Frieden, C. Analysis of Numerical Methods for Computer Simulation of Kinetic Processes: Development of KINSIM—A Flexible, Portable System. *Anal. Biochem.* **1983**, *130* (1), 134–145. https://doi.org/10.1016/0003-2697(83)90660-7.
(35) Sanz, J.; Lombraña, J. I.; De Luis, A. M.; Ortueta, M.; Varona, F. Microwave and Fenton's Reagent Oxidation of Wastewater. *Environ. Chem. Lett.* **2003**, *1* (1), 45–50. https://doi.org/10.1007/s10311-002-0007-2.
(36) Armstrong, D. A.; Huie, R. E.; Koppenol, W. H.; Lymar, S. V.; Merényi, G.; Neta, P.; Ruscic, B.; Stanbury, D. M.; Steenken, S.; Wardman, P. Standard Electrode Potentials Involving Radicals in Aqueous Solution: Inorganic Radicals (IUPAC Technical Report). *Pure Appl. Chem.* **2015**, *87* (11–12), 1139–1150. https://doi.org/10.1515/pac-2014-0502.
(37) *Chemical Thermodynamics of Iron, Part 1*. Nuclear Energy Agency (NEA). https://www.oecd-nea.org/jcms/pl_14374/chemical-thermodynamics-of-iron-part-1?details=true (accessed 2025-04-22).
(38) Knight, R. J.; Sylva, R. N. Spectrophotometric Investigation of Iron(III) Hydrolysis in Light and Heavy Water at 25°C. *J. Inorg. Nucl. Chem.* **1975**, *37* (3), 779–783. https://doi.org/10.1016/0022-1902(75)80539-2.
(39) Bielski, B. H. J.; Cabelli, D. E.; Arudi, R. L.; Ross, A. B. Reactivity of HO2/O−2 Radicals in Aqueous Solution. *J. Phys. Chem. Ref. Data* **1985**, *14* (4), 1041–1100. https://doi.org/10.1063/1.555739.
(40) Perrin, D. D. *Ionisation Constants of Inorganic Acids and Bases in Aqueous Solution*; Elsevier, 1982. https://doi.org/10.1016/C2013-0-13276-X.
(41) Jacobsen, F.; Holcman, J.; Sehested, K. Activation Parameters of Ferryl Ion Reactions in Aqueous Acid Solutions. *Int. J. Chem. Kinet.* **1997**, *29* (1), 17–24. https://doi.org/10.1002/(SICI)1097-4601(1997)29:1<17::AID-KIN3>3.0.CO;2-O.
(42) Barb, W. G.; Baxendale, J. H.; George, P.; Hargrave, K. R. Reactions of Ferrous and Ferric Ions with Hydrogen Peroxide. Part I.—The Ferrous Ion Reaction. *Trans. Faraday Soc.* **1951**, *47* (0), 462–500. https://doi.org/10.1039/TF9514700462.
(43) Hardwick, T. J. THE RATE CONSTANT OF THE REACTION BETWEEN FERROUS IONS AND HYDROGEN PEROXIDE IN ACID SOLUTION. *Can. J. Chem.* **1957**, *35* (5), 428–436. https://doi.org/10.1139/v57-062.
(44) Barb, W. G.; Baxendale, J. H.; George, P.; Hargrave, K. R. Reactions of Ferrous and Ferric Ions with Hydrogen Peroxide. Part II.—The Ferric Ion Reaction. *Trans Faraday Soc* **1951**, *47* (0), 591–616. https://doi.org/10.1039/TF9514700591.
(45) Wells, C. F.; Salam, M. A. The Effect of pH on the Kinetics of the Reaction of Iron(II) with Hydrogen Peroxide in Perchlorate Media. *J. Chem. Soc. Inorg. Phys. Theor.* **1968**, 24. https://doi.org/10.1039/j19680000024.
(46) Millero, F. J.; Yao, W.; Aicher, J. The Speciation of Fe(II) and Fe(III) in Natural Waters. *Mar. Chem.* **1995**, *50* (1), 21–39. https://doi.org/10.1016/0304-4203(95)00024-L.

(47) Scheres Firak, D.; Schaefer, T.; Kula, C.; Taherkhani, N.; Herrmann, H. Ionic Strength Effect in Fenton Reactions in the Presence of Sulfate and Its Influence on the Aqueous Particle Phase. *ACS Earth Space Chem.* **2025**, *9* (3), 662–670. https://doi.org/10.1021/acsearthspacechem.4c00362.
(48) Ameta, R.; K. Chohadia, A.; Jain, A.; Punjabi, P. B. Fenton and Photo-Fenton Processes. In *Advanced Oxidation Processes for Waste Water Treatment*; Elsevier, 2018; pp 49–87. https://doi.org/10.1016/B978-0-12-810499-6.00003-6.
(49) Miller, C. J.; Rose, A. L.; Waite, T. D. Importance of Iron Complexation for Fenton-Mediated Hydroxyl Radical Production at Circumneutral pH. *Front. Mar. Sci.* **2016**, *3*. https://doi.org/10.3389/fmars.2016.00134.
(50) Luzzatto, E.; Cohen, H.; Stockheim, C.; Wieghardt, K.; Meyerstein, D. Reactions of Low Valent Transition Metal Complexes with Hydrogen Peroxide. Are They "Fenton-like" or Not? 4. The Case of Fe(II)L, L = Edta; Hedta and Tcma. *Free Radic. Res.* **1995**, *23* (5), 453–463. https://doi.org/10.3109/10715769509065266.
(51) Furcas, F. E.; Mundra, S.; Lothenbach, B.; Angst, U. M. Speciation Controls the Kinetics of Iron Hydroxide Precipitation and Transformation at Alkaline pH. *Environ. Sci. Technol.* **2024**, *58* (44), 19851–19860. https://doi.org/10.1021/acs.est.4c06818.
(52) Lu, H.-F.; Chen, H.-F.; Kao, C.-L.; Chao, I.; Chen, H.-Y. A Computational Study of the Fenton Reaction in Different pH Ranges. *Phys. Chem. Chem. Phys.* **2018**, *20* (35), 22890–22901. https://doi.org/10.1039/C8CP04381G.
(53) Chen, H.-Y. Why the Reactive Oxygen Species of the Fenton Reaction Switches from Oxoiron(IV) Species to Hydroxyl Radical in Phosphate Buffer Solutions? A Computational Rationale. *ACS Omega* **2019**, *4* (9), 14105–14113. https://doi.org/10.1021/acsomega.9b02023.
(54) Loures, C. C. A.; Alcântara, M. A. K.; Filho, H. J. I.; Teixeira, A. C. S. C.; Silva, F. T.; Paiva, T. C. B.; Samanamud, G. R. L. Advanced Oxidative Degradation Processes: Fundamentals and Applications. *Int. Rev. Chem. Eng. IRECHE* **2013**, *5* (2), 102–120. https://doi.org/10.15866/ireche.v5i2.6909.